Nikolaos Malissovas - Delft University of Technology - Master Thesis - August 2017

Allowable compression load in the sagbend area during J-Lay

MARINE CONTRACTORS

Allowable compression load in the sagbend area during J-lay

By

Nikolaos Malissovas

in partial fulfilment of the requirements for the degree of

Master of Science
in Offshore & Dredging Engineering

at the Delft University of Technology,
to be defended publicly on Thursday August 31, 2017

Student number 4521714

Thesis committee:

Prof. dr. Ir. A. V. Metrikine	TU Delft, Chairman
Ir. Y. Qu	TU Delft, Daily supervisor
Ir. H. Smienk	HMC, Senior Supervisor
It. J. Kuijpens	HMC, Daily supervisor

TU Delft
Delft University of Technology

MARINE CONTRACTORS

Preface

This thesis is a result of an eight-month research conducted in Heerema Marine Contractors (HMC) in cooperation with the Delft University of Technology as partial fulfillment of the requirements for the degree “Master of Science” in Offshore and Dredging engineering.

I would like to thank the chairman of the department, professor Andrei Metrikine for his clear insights and guidance along this difficult journey. You have been an example for me, I will divulge stories about your immense knowledge around any field of engineering for years to come. My special thanks to my TU Delft supervisor, Yang Qu who was always willing to help and for the time that he devoted for our meetings. I will never forget the first, where the final target of this thesis seemed almost unreachable. I wish you all the luck for your Ph.D. research!

Jean, it was my honor to work with such a smart and experienced engineer. The interest that you showed around this thesis was a predominant factor in the final result. My motivation was through the roof, as I understood that I was working on an important problem. While you allowed me to develop my own thinking, your comments guided me to the target and you always kept me away from irrelevant deviations. I will always remember my baby steps beside you and our first meetings. Thank you for all those wonderful discussions.

Furthermore, I would like to give special thanks to you Bob. You had a great influence on this project. I really appreciate the time that you devoted. Without you, the result might have been different. Henk, thank you for being patient and always willing to help, especially during my first steps in HMC. Always smiley and always ready to make sharp questions, I will never forget our first interactions.

N. Malissovas
Delft, August 2017

Abstract

Offshore pipelay is the operation of laying a pipe from a surface vessel to the seabed. As the suspended pipe approaches the seabed, it bends downwards forming the sagbend. The sagbend is controlled by the vessel position and a tensile load is applied to counteract the weight of the pipe. During the engineering phase of previous HMC projects, compression was observed in the sagbend, for both shallow and deep water projects. Clients and regulatoratory authorities are hesitant to allow compression, limiting workability. DNV-GL implies that compression can be accepted if it does not induce other failure modes, like local buckling. A global stability assessment should be performed to identify if the resultant deformations are acceptable. HMC is intrigued to discover what the constraints are regarding global buckling during pipe-laying. The objective is to develop a methodology to calculate an allowable compressive load, increasing the operational window.

During pipe-laying, the vessels motions are transferred to the pipe, resulting in a time varying loading that can exceed the applied tension in the sagbend area, leading to compression. This can induce two different mechanisms of stability loss. Either the lateral vibrations can be excited, amplifying the amplitudes of the lateral motion, or tension can change into compression in a segment of the pipe for a part of the wave cycle, leading to a pulsating compressive loading. Focus is given on the instability onset due to the compressive pulsating loading, named as impulse dynamic buckling, as dangerously high strains can occur in that case. The system can exhibit higher load bearing capacity than the quasi-static Euler buckling load, when the loading is dynamic, due to inertia and drag.

Depending on the project requirements, different installation vessels are utilized. The vessels response under wave excitation should be taken into account for the pipe-laying analyses. For that reason, a specialized finite element software, Flexcom, is used. The ability of Flexcom to accurately predict the onset of impulse dynamic buckling is validated by comparison with a simplified analytical model. A curved simply supported Euler-Bernoulli beam is utilized for validation, based on the theory of moderately large displacements. A dynamic buckling criterion and an applicable methodology, capable of predicting the onset of impulse dynamic buckling based on Flexcom's post-processing results, is proposed. Constant velocity loading is applied to demonstrate the effect of loading velocity in the dynamic buckling load. Harmonic displacement loading is applied to validate the proposed dynamic buckling criterion.

Two previous HMC projects are utilized as base cases to evaluate the proposed methodology. Finite element analyses in Flexcom is performed and the critical parameters regarding dynamic compression generation are identified. Based on the proposed dynamic buckling criterion, global stability assessment is performed for the base cases, against regular and irregular wave excitation. The critical vessel motions for the onset of impulse dynamic buckling, are identified. A sensitivity study on the driving parameters is performed. Following a limit state design approach for the base cases, results demonstrate that compression could be tolerated during pipelay operations, providing that other failure modes are covered. Hence, the limit of the local buckling criteria can be fully exploited despite the occurrence of compression.

List of abbreviations

Abbreviation	Definition
DCV	Deep-water Construction Vessel
DLF	Dynamic Load Factor
DNV- GL	Det Norske Veritas - Germanischer Lloyd
DOF	Degree Of Freedom
DP	Dynamic positioning
HMC	Heerema Marine Contractors
HOM	Hang Off Module
ISO	International Organization for Standardization
LCC	Load Controlled Condition
ODE	Ordinary Differential Equation
RAO	Response Amplitude Operator
TDP	Touch Down Point

List of symbols

Symbol	Definition	Unit
a	acceleration amplitude	m/s^2
A	cross sectional area	m^2
A_1	dimensionless constant	-
A_2	dimensionless constant	-
C_d	drag coefficient	-
D_i	internal pipe diameter	m
D_o	external pipe diameter	m
E	modulus of elasticity	N/m^2
$f(t)$	displacement of movable support	m
$f(\dot{t})$	velocity of movable support	m/s
F	force	N
g	gravitational acceleration	m/s^2
H	heave amplitude	m
I	cross sectional moment of inertia	m^4
J	impulse	Ns
J_{cr}	critical impulse	Ns
k	factor for the end conditions in Euler load	-
L	length	m
m	mass	Kg
M	bending moment	Nm
n	integer, defining the mode number	-
P	axial force	N
P_{cr}	critical buckling load	N
Q	shear force	N
t	time	s
$T(x,t)$	total effective tension	N
$T_D(x,t)$	dynamic component of effective tension	N
$T_S(x)$	static component of effective tension	N
$w_o(x)$	imperfection	m
$W_n(x,t)$	horizontal deflection amplitude of mode n	m
W_o	imperfection amplitude	m
u	longitudinal displacement	m
v	velocity amplitude	m/s
v_{cr}	critical velocity amplitude	m/s
v_s	speed of longitudinal compressive waves in steel	m/s

Symbol	Definition	Unit
$v_{terminal}$	terminal velocity	m/s
$w(x,t)$	lateral deflection	m
x	longitudinal axis coordinate	m
z	vertical axis coordinate	m

Greek symbols	Definition	Unit
a_{cr}	critical acceleration	m/s^2
ε	Cauchy strain	-
ε_{long}	strain at beam axis due to axial shortening	-
ε^o	total strain at beam axis	-
ε_{rot}	strain at beam axis due to rotation	-
θ	rotation of beam axis	rad
ρ_s	density of sea water	kg/m^3
ρ_w	density of steel	kg/m^3
ΔP	change in momentum	kg m/s
μ	dynamic viscosity of water	Pa s
π	ratio of a circle's circumference to its diameter	-
ω	radial frequency	Hz
Ω	dynamic similarity number	-

Sign conventions

PART A

The internal axial force (P), bending moment (M) and shear force (Q), acting on the differential element of the beam given below, are considered positive as follows:

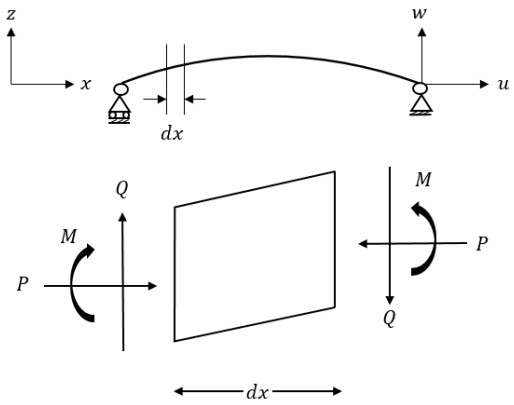

Figure i: Sign convection, part A.

A positive axial force (P) represents compressive loading, while a negative represents tensile loading . The lateral deflection towards the vertical axis z is denoted as w and the axial displacement along the longitudinal axis x is symbolized with u.

PART B

A negative effective tension (T) represents compressive loading, while a positive represents tensile loading. The following figure demonstrates the axis convention of part B, along with the meaning of the directional terms “heave”, “lateral”, “longitudinal” and “transversal”.

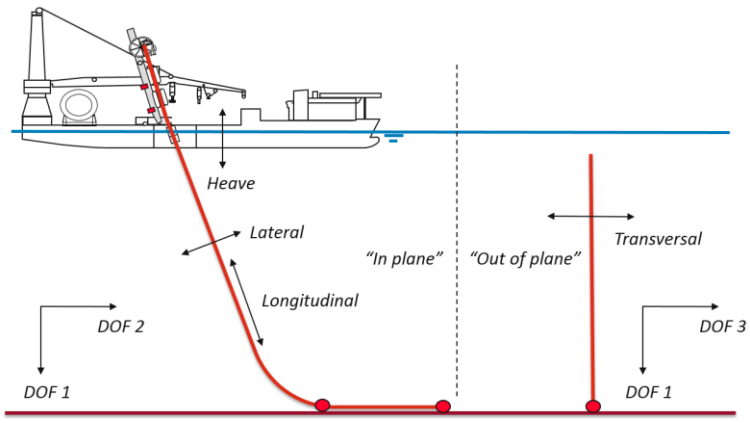

Figure ii: Sign convection, part B.

Table of contents

1

Introduction

1.1. Problem definition

During offshore pipelay, the suspended pipe may go through two qualitatively different types of compression, namely axial (or true wall) compression and effective compression (negative effective tension). The true wall axial force is given by the integral of stresses over the cross section of the pipe. The effective tension accounts for the effects of the internal and external pressure (buoyancy). The first type of compression, combined with bending moment and the external hydrostatic pressure, can cause local buckling. Local buckling is the buckling behavior within the pipeline's cross section. The second type, effective compression along a segment of the suspended pipe, can initiate dynamic instability and can consequently result in increased deformations of the pipe that can possibly lead to failure.

The vessels motions are transferred to the suspended pipe, at the so called hang off module (HOM) and the pipe is being dynamically excited. Due to the heave motion of the HOM, effective compressive loads were observed in the sagbend area in both shallow and deep water projects. This is due to dynamic compression [1]. Dynamic compression occurs on a segment of the line when the time-varying component of the tension (dynamic tension), exceeds the static tension applied from the installation vessel on that section. A sinusoidal compressive load, with a bigger amplitude than the quasi-static Euler buckling load, is suddenly applied over a segment of the pipe. That type of loading can initiate a dynamic instability type, named as impulse dynamic buckling. The word impulse is used to emphasize the high amplitude, comparing to the static buckling capacity and sudden application of the axial load. This phenomenon can induce extensive deflections leading to amplified bending strains and possibly failure. Thus, the onset of impulse dynamic buckling can possibly impose a limitation for the pipelay operation.

Regarding the acceptance of compression, DNV states that it can be accepted provided that it doesn't lead to other failure modes like local buckling or excessive fatigue loading. DNV states that a global buckling assessment should be performed, without providing specific instructions, referring to other conventional engineering codes as ISO. In order to avoid conservatism, the design procedure for an unconventional structure with large slenderness ratio like a suspended pipe during

J-lay, should not adopt the classic stability criteria for conventional structures, where a quasi-static approach is implemented. The quasi-static buckling capacity of the pipe is considerably smaller than the compressive forces that emerge due to the heave motion of the HOM during the engineering phase of pipelaying projects. The current industry approach is to stall the pipe-laying operation when a sea state is leading to compressive loading.

When the loading is dynamic, global buckling is not a failure mode, but a type of instability. When slender structures are loaded with compressive dynamic forces, dynamic buckling can occur. The dynamic buckling phenomenon is different from static buckling, as the time parameter becomes important and the response of the system depends on the loading itself. Thus, a different approach should be developed for the identification of the critical parameters, meaning force or displacement amplitude and duration of application. Dynamically loaded systems can exhibit higher load bearing capacity than the quasi-static Euler buckling load due to the contribution of inertia which is retarding the amplification of displacement due to the compressive loading. In the marine environment, the hydrodynamic drag force acts in a similar manner contributing to the dynamic buckling capacity of the system. Various criteria for the definition of buckling have been proposed, the most known being the following: *Buckling is the state of a structure for which a large increment in displacement occurs when the load slightly increases.* However, this criterion is not directly applicable for the stability assessment of the suspended pipe during pipelaying, as the occurrence of the increase in displacement is not always straightforward.

In order to conduct a global stability assessment, a design tool like a finite element software, along with an appropriate methodology for the identification of the instability onset should be available. Using a general finite element software like ABAQUS or ANSYS is an option. Those programs have been thoroughly used to model linear and nonlinear buckling both in statics and dynamics and many publications exist validating this ability. But, in case of pipe-laying, the vessels response should be also taken into account and a nonlinear, coupled dynamic analysis is imperative. For that reason, a specialized finite element software, Flexcom, is being used as standard pipelay analysis tool for HMC. Flexcom can model the vessels response under any given sea-state, significantly facilitating the design procedure.

In order to use Flexcom to identify the impulse dynamic buckling onset, its ability to model the transient response of the pipe under compressive pulse loading shall be investigated. Accordingly, an appropriate methodology for the identification of the critical loading conditions should be developed. Then, the global stability assessment as DNV proposes can be conducted, defining the allowable HOM heave motions, erasing the conservatism around the dynamic compression phenomenon.

1.2. Research aim

The goal of this graduation thesis is to is build up an efficient methodology to quantify an allowable compressive load in the pipe during installation. The allowable harmonic heave motions of the HOM leading to compressive loading should be identified. This will increase the offshore operational window.

The target is to develop a programmable methodology, based on Flexcom's nonlinear dynamic analyses post-processing results, capable of conducting a robust stability assessment against both regular and irregular excitation.

1.3. Research question

HMC wants to discover if and what the constraints are if compression occurs and if any compression in the pipe during installation can be permitted. In order to reach the final target, the problem can be decomposed into the following questions:

1. *Can the pipe tolerate an effective axial compressive load with a bigger amplitude than its static buckling capacity?*

2. *Can Flexcom accurately identify the onset of impulse dynamic buckling?*

3. *How can the global stability assessment be efficiently conducted against harmonic heave excitation of the HOM?*

4. *Which are the driving parameters regarding the generation of the compressive force in the sagbend?*

5. *Which are the allowable harmonic HOM motions for the base cases?*

6. *How can the global stability assessment be efficiently performed against irregular wave excitation?*

1.4. Thesis structure

The thesis main body is divided into two main parts. The order of the chapters, reflects the research timeline.

PART A: Initially, the literature study and the background theory is introduced. The difference between dynamic and static (Euler) buckling is highlighted. Subsequently, the ability of Flexcom

to accurately predict the onset of instability due to compressive pulse loading is being investigated. The validation is performed by comparing Flexcom with an analytical model of an initially curved, perfectly elastic, simply supported beam in compression. Then the analytical model is used to develop a methodology for the identification of impulse dynamic buckling onset due to harmonic displacement loading.

PART B: Finite element analyses using Flexcom FE software is performed for the base cases. The dynamic compression generation is investigated. In order to understand the mechanisms behind the phenomenon, a sensitivity study on the driving parameters is performed. Finally, the global buckling assessment is being conducted, adopting the methodology derived in part A. The allowable combinations of period and amplitudes considering harmonic HOM heave motion are identified. Then utilizing the impulse momentum theorem, the impulse (integral of pulse load) that leads to impulse dynamic buckling onset, is measured per period of excitation for each base case. This is employed to assess the stability of the suspended pipe against irregular excitation.

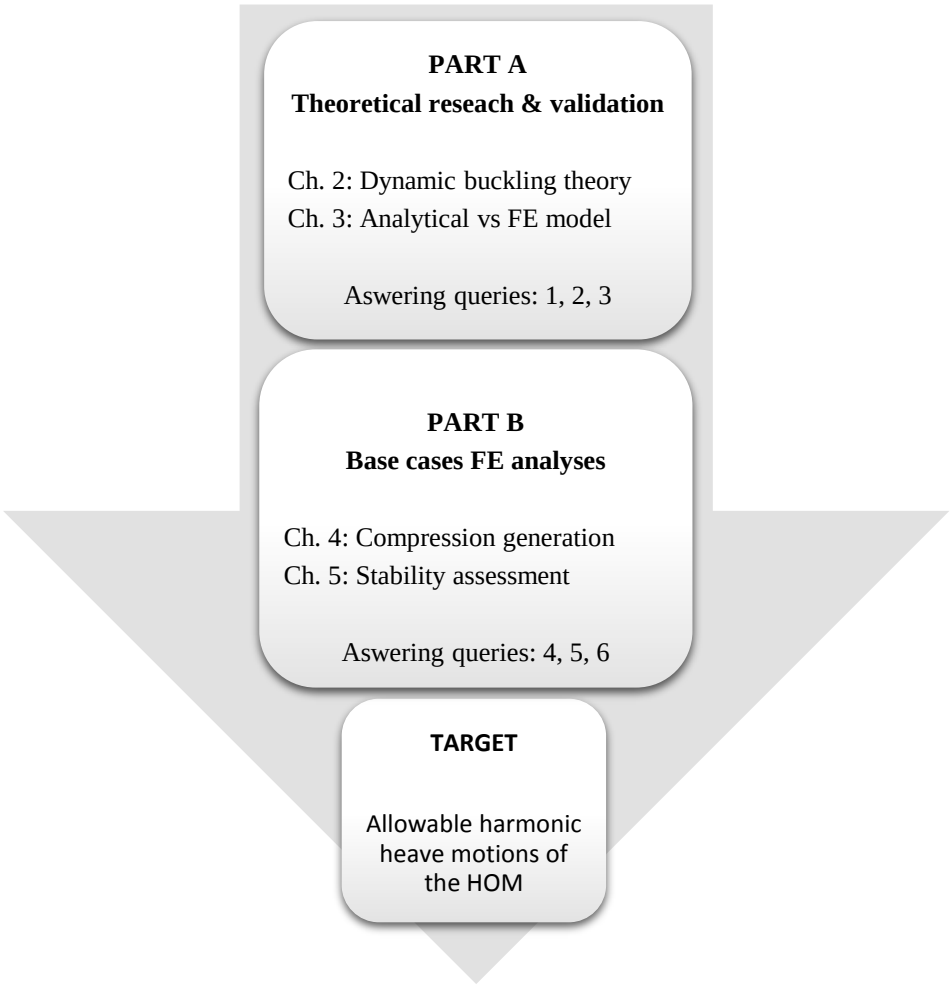

Figure 1: Thesis main body structure.

1.5. Pipelay basic definitions

The basic pipelay (J-lay) abbreviations that will be used in the present, are schematically represented in the following figures.

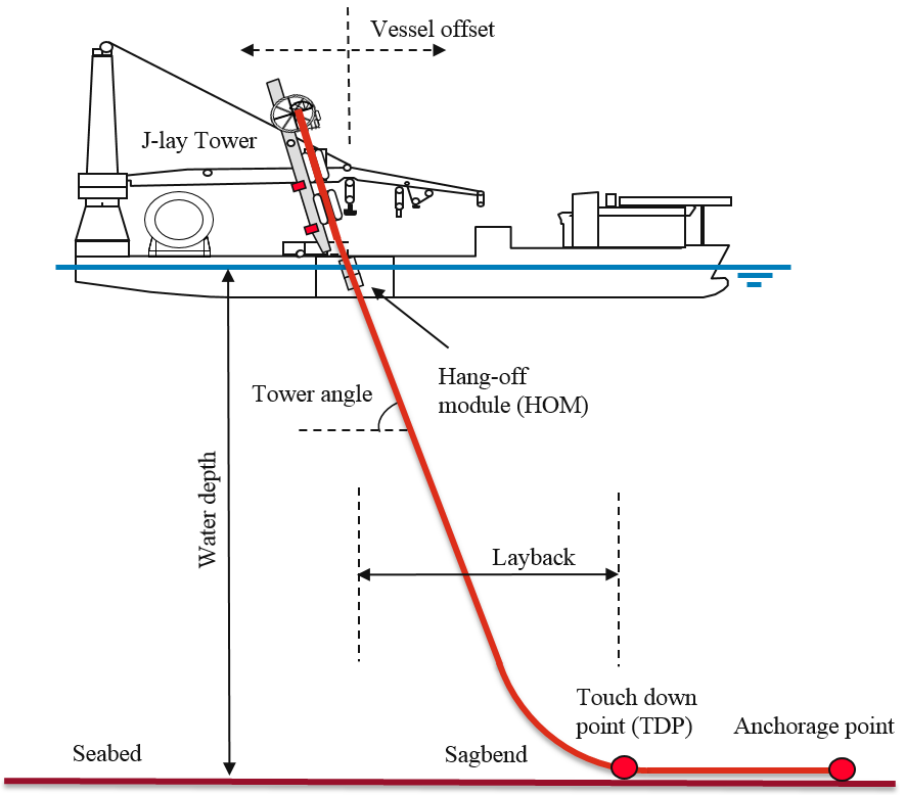

Figure 2: Basic J-lay definitions, side view.

Vessel offset: Deviation of vessel position from the nominal.

Tower angle - Departure angle: The angle between the J-lay tower and the horizontal.

Hang off module (HOM): The module on the tower from where the pipe is suspended.

Sagbend: Curved section of the pipeline, near the TDP.

Layback: Distance between the HOM and the TDP.

Touch down point (TDP): The first point where the pipe touches the seabed.

Anchorage point: Final point in touch with the seabed for the finite element model.

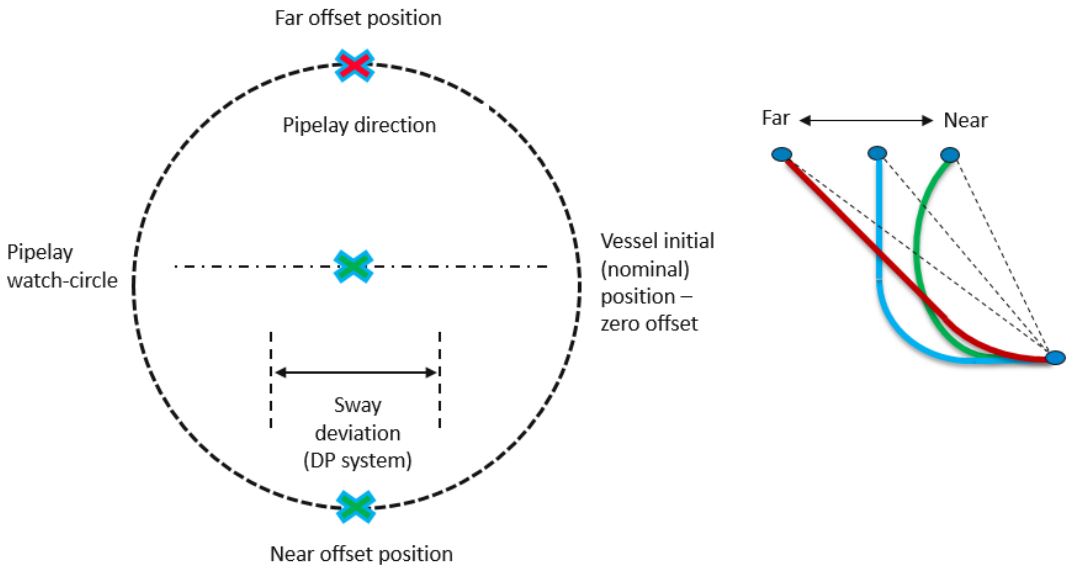

Figure 3: Basic J-lay definitions, plan view.

Pipelay watch-circle: Allowable deviation from nominal pipelay position.

Near offset position: Maximum allowable decrease in layback.

Far offset position: : Maximum allowable increase in layback.

Sway deviation – out of plane offset: Deviation from the straight route, due to DP system tolerance.

DP system: System that controls the position and motion of the pipelay vessel.

1.6. The base cases

Two previous HMC J-lay projects will be considered as base cases for the research.

Shallow water case: Pipelay water depth is 237m.

Deep water case: Pipelay water depth is 2947m.

PART A

Theoretical study & validation: Dynamic buckling of elastic curved beam. Analytical vs Flexcom FE model

Figure 4: HMC AEGIR DCV.

2

Dynamic buckling background theory

2.1. Introduction

This chapter includes the theory that the research is based on. The difference between static and dynamic buckling is presented in short. Then the forms of dynamic instability, occurring under time-varying parametric loading are being presented. Those are parametric resonance and impulse dynamic buckling. Focus will be given to the second type of instability, as it has been proven [2], that parametric resonance cannot induce dangerously large strains in suspended pipes in the marine environment.

The term “impulse” is generally used to describe the application of a force for a duration of time. Sometimes though, it is used to emphasize the suddenness of an event, for example, it is used to describe “fast” loading, thus the definition of “impulse buckling”, underlines the suddenness of the event. Which loading can be considered “fast” and which “slow” has to do with the load itself, plus the physical characteristics of the system of application. The definition of the dynamic similarity number introduced by Hoff in 1951 [3], is being analysed in order to give an insight for the classification of loading, depending on loading velocity and on the systems physical properties. This number can give further insight into the significance of the dynamic effects on a structural system and it will be used to show the dependency of the rate of compression for the base cases.

In order to identify the onset of dynamic buckling various criteria has been proposed. Each of those presents advantages and disadvantages regarding accuracy, computational effort, and applicability. The most widely used dynamic buckling criteria are being presented herein. Finally, the impulse - momentum theorem is being introduced.

2.2. Literature review

2.2.1. Dynamic buckling

Several studies have been conducted by various researchers regarding the buckling capacity of dynamically loaded systems. Leonard Euler first calculated the critical buckling load for statically compressed columns back in 1744. Since then, numerous theoretical and experimental studies demonstrated that the critical buckling load of a structure under dynamic loading cannot be predicted by the Euler formula. The dynamic buckling capacity depends on the rate of compression [3], [4]. This is possible only for imperfect structures. Particularly, in 1951 N.J. Hoff demonstrated that even at small compression rates compared to the speed of sound, the dynamic buckling capacity can exceed the static buckling capacity. This was both mathematically and experimentally validated by loading columns in a hydraulic testing machine. It has been concluded that specifically for slender columns the maximum force can exceed the Euler static force by a factor of 100. This is because the lateral inertia of the column is retarding the deflections of the column. Consequently, a specific amount of time is needed for the system to buckle. Based on analytical calculations assuming the first buckling mode and constant velocity loading, Hoff demonstrated that the critical buckling load depends on two parameters. Those are the amplitude of the imperfection, and a dimensionless parameter named as the dynamic similarity number. This depends on the slenderness ratio of the column and the loading velocity. The dynamic buckling behavior depends also on the method of compression. Different loading conditions are analyzed in paper [5]. Those can be classified as constant velocity or constant mass impulse loading scheme, constant velocity or displacement loading scheme or force-time impulse loading.

Buckling under compressive pulse loading often referred as impulse dynamic buckling was studied in papers [6], [7], [8], [9]. It was concluded that the stability analyses of a structure under in plane pulse loading depends on the pulse characteristics, meaning amplitude, duration and shape. For loading durations close to the period of fundamental natural vibrations the dynamic impulse buckling occurs. It was demonstrated that both load duration and amplitude, affect the response of the structure. When the amplitude of the pulse load is low the structure vibrates around the static equilibrium position. For pulse loads of short duration compared to the period of fundamental natural vibrations, the dynamic buckling capacity exceeds the static one. For loads with a duration that exceeds twice the period of fundamental natural vibrations, the quasi-static capacity is being measured.

The influence of axial inertia is discussed in paper [10]. It has been proven that the effect of the axial inertia is not of significant importance for conventional structures (those with slenderness ratio lower than 150). The hypothesis behind that is that the time required for an axial pressure wave to travel from the one end of the column to the other is at least one order of magnitude shorter, compared to the time necessary for the lateral displacements to develop at the critical buckling load.

The effect of imperfection was studied in paper [11]. The increase of the imperfection amplitude reduced the dynamic buckling load for the particular load duration. For various imperfection

amplitudes examined, the dynamic buckling loads were found to decrease with the increase of the loading duration. In paper [12] it was concluded that the load duration affects the imperfection sensitivity of the structure. For small loading durations, it was found that the critical buckling load rapidly decreases as the imperfection increases.

The aforementioned conclusions are particularly important for the problem in hand. The suspended pipeline being highly slender is expected to yield increased buckling capacity under the dynamic compressive loading caused by the vessels heave motion. Possible limitations can arise due to the variation of the vessels position from the nominal, because in that case the imperfection of the structure is being affected.

2.2.2. Dynamic compression

The problem of dynamic compression in the offshore environment has been studied for riser applications. Several researchers have investigated this phenomenon, the majority of those originating from Brazil, where a number of deep water field discoveries and developments emerged the last two decades.

Ribeiro, Roveri and Mourelle from Petrobras S.A, studied the dynamic compression development in flexible risers [13]. They concluded that the axial compressive force is being introduced due to the inability of the pipe to travel fast enough through the water column, due to the opposing drag force. Aranha and Pinto [14] presented an algebraic approximation for the dynamic tension on deep water risers, which agrees fairly well with numerical simulations and experiments. The restoring forces mechanism and its contribution to compression where identified by using linear cable equations, initially derived by and Irvine and Caughey [15] and Blienk [16]. The solution technique using asymptotic functions was based in the work of Triantafillou [17]. It was deducted that the ratio between the longitudinal (elastic) and lateral (catenary) heave absorption mechanisms is the governing parameter, controlling the response of the riser to the imposed heave motion. Additionally, it was shown that the inclination significantly affected the dynamic tension generation. Simos and Fujarra [1], performed extensive comparisons between experimental and numerical models of rigid and flexible risers in compression. For both type of models it was concluded that dynamic buckling is accompanied by severe out of plain vibrations. Mc Cann, Smith and O'Brien from MCS Kenny [18], studied the relation of compression with heave velocity. They introduced a dimensionless parameter, comprising from the hang-off velocity divided by the terminal velocity of the pipe. It was shown, that for the examined base cases, this ratio when lower than unity, provides an indication of compression existence.

2.3. Static vs dynamic buckling

Buckling can be broadly categorized in static and dynamic. Static buckling occurs under static loads and dynamic buckling occurs under dynamic loads.

In static buckling, the critical axial load is the maximum load which a beam can bear while staying straight. It is given by the well-known Euler formula and it depends on the geometry and the material of the structure. The governing differential equation of the lateral motion of a straight beam in statics, is the following:

$$EI\frac{\partial^4 w}{\partial x^4} + P\frac{\partial^2 w}{\partial x^2} = 0 \qquad [2.1]$$

Where, $w(x)$ is the lateral motion, E is the modulus of elasticity, I is the cross-sectional moment of inertia and P is the axial load of the beam. For a simply supported beam with length L, the critical buckling load (Euler load) is determined by:

$$P_{cr} = \frac{\pi^2 EI}{L^2} \qquad [2.2]$$

For loads exceeding P_{cr}, the lateral displacements tend to infinity and failure is assumed to occur. The critical buckling load depends on the material and the geometry of the structure.

In dynamic buckling, the critical axial load should be defined according to the adopted buckling criterion. More around the dynamic buckling criteria can be found in chapter 2.7. The governing differential equation of the lateral motion of a straight beam in dynamics is the following:

$$EI\frac{\partial^4 w}{\partial x^4} + P(t)\frac{\partial^2 w}{\partial x^2} + \frac{\rho_s A\partial^2 w}{\partial t^2} = 0 \qquad [2.3]$$

And specifically, in the marine environment:

$$EI\frac{\partial^4 w}{\partial x^4} + P(t)\frac{\partial^2 w}{\partial x^2} + \frac{\rho_s A\partial^2 w}{\partial t^2} + \mu A_1\frac{\partial w}{\partial t} + \frac{1}{2}\rho_w D_o A_2\left|\frac{\partial w}{\partial t}\right|\frac{\partial w}{\partial t} = 0 \qquad [2.4]$$

Where, I is the cross sectional moment of inertia, A the cross sectional area of the pipe, ρ_s is the density of steel, ρ_w is the density of water, D_o is the outer diameter of the pipe, A_1, A_2 are two dimensionless hydrodynamic drag constants and μ is the dynamic viscosity of water [2].

The difference between the static and dynamic buckling is visible comparing equations [2.1] and [2.3]. The dynamic equation has an additional time-related term, the inertial force. When it is surrounded by fluid, another time dependent parameter emerge, the drag force. The pipe can exhibit increased load bearing capacity due to inertia and drag. This capacity is being affected not only by

the geometry and material, but also by the type of loading (magnitude, duration, shape) so the response depends also on the loading itself.

Dynamic buckling can only occur for imperfect structural configurations [3]. The term "dynamic buckling" refers to stability of a structure under time-dependent loads. When examining a displacement induced buckling problem, the rate of change of the induced motion has a major effect on the dynamic behavior of the structure. This contribution also depends on the physical characteristics of the system. The combined effect can be disclosed in the so called dynamic similarity number.

2.4. Dynamic similarity number

In 1951, Hoff performed various experiments, loading beams in a hydraulic test machine with various velocity amplitudes. He demonstrated the dependence of the dynamic critical buckling load on two parameters. The initial imperfection (out of straightness) of the beam and the dynamic similarity number, defined as:

$$\Omega = \pi^8 \left(\frac{R}{L}\right)^6 \left(\frac{v_s}{v}\right)^2 \quad [2.5]$$

With R being the radius of gyration, v is the constant speed applied to the columns end and v_s the longitudinal compressive waves speed, given by

$$v_S = \sqrt{E/\rho} \quad [2.6]$$

$$R = \sqrt{I/A} = L/\delta \quad [2.7]$$

Where δ is the slenderness ratio of the beam. This number contains all the information needed to classify the loading, taking into account the characteristics of the structure. The same load can be considered rapid for a structure and quasi-static for another, with different similarity number. Generally when $\Omega \to \infty$, the quasi-static capacity is being measured and when $\Omega \to 0$, the loading can be considered rapid and the inertial forces are expected to cause a time lag between the lateral motion and the prescribed tip displacement. This is associated with the so called "time to buckle" as the system "needs" a specific amount of time to reach an apriori defined critical condition (depending to the adopted dynamic buckling criterion) [3]. This renders the system capable of maintaining a bigger force than the-quasi static critical buckling load (Euler load). Hoff derived the following relation, relating the dynamic buckling capacity of the system to the static.

$$\frac{P_{cr,dynamic}}{P_{cr,static}} = 1 + \left(\frac{3}{4\Omega^{\frac{1}{2}}} \ln\left(\frac{2}{\pi d^2 \Omega}\right)\right)^{\frac{2}{3}} \quad [2.8]$$

Where d is a dimensionless imperfection parameter. Observing equations [2.5] [2.7] and [2.8], one can notice that an increase in the slenderness of the structure results in a decrease of the dynamic similarity number. That means that, for an increasing slenderness ratio the contribution of inertia to the critical dynamic buckling load is increasing.

This can be related to the pipelay problem as the large slenderness ratio of the suspended pipe is expected to yield increased ratios of dynamic to static buckling capacity.

2.5. Dynamic load factor

The ratio of the critical dynamic buckling load to the static buckling load, can be defined as the dynamic load factor (DLF):

$$DLF = \frac{P_{cr,dynamic}}{P_{cr,static}} > 1 \qquad [2.9]$$

This demonstrates the significance of the added time varying parameters to the dynamic buckling problem. DLF Values as high as 100, can be observed depending on the associated parameters. Values lower than 1, can be observed for large values of initial imperfection in the rapid loading regime [4].

The dynamic load factor depends on the applied load amplitude, duration and shape of the applied pulse load. It variates also with the imperfection of the system (out of straightness). This is important for the pipelay procedure as the different vessel positions are alternating the imperfection of the pipe.

2.6. Dynamic stability under parametric loading

The definition of parametric loading is used when the forcing term appear as a parameter that multiplies the displacement of the structure in the left hand side of the equation. In forced structural vibrations, the forcing term appears in the right hand side.

Recalling equation [2.3], one can notice that the axial load *P(t)* multiplies the structural displacement $w(x,t)$, being thus a parameter of the equation.

2.6.1. Parametric resonance and impulse dynamic buckling

Two different types of instability can occur in structures whose lateral motion is described by equation [2.3]. The following figure offers a visual representation of those:

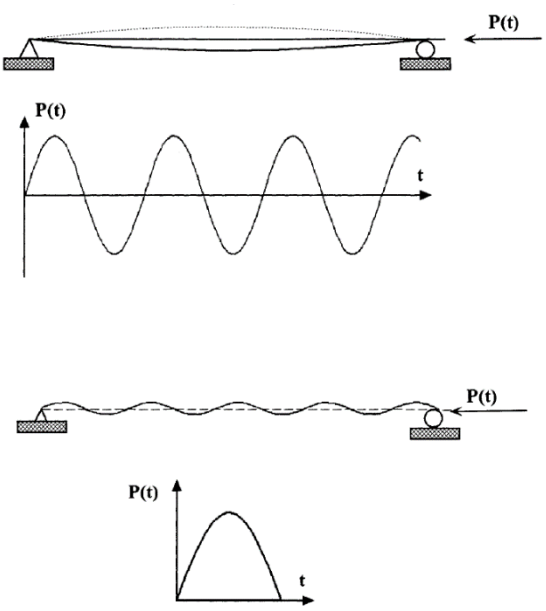

Figure 5: Vibration buckling (top), impulse buckling (bottom).
Courtesy (Lindberg and Florence, 2003).

In the left side of figure 5, the bar is loaded with a load oscillating with a frequency equal twice the fundamental bending frequency. The amplitude of the load is smaller than the critical static (Euler) load. When bar bends to one side or the other, the axial load is multiplied with the displacement, inducing additional bending. The same effect can be noticed if the forcing frequency equals three or more times the natural bending frequency ($f_{load}=n\,x\,f_{nat}$, $n=2,\ 3\ ..N$). This phenomenon is being called *parametric resonance*. Buckling initiation due to parametric excitation is often called as *vibration buckling* [19]. The response of the structure due to this excitation is quite similar to resonant forced vibration. The difference is that in case of the parametric excitation the axial force induces a bending moment which causes the growth in deflection, where in resonant forced vibration the structure deflects in the same direction as the induced pulse. Vibration buckling can induce unbounded growth of the lateral displacement (instability). This would occur in the absence of damping and geometrical nonlinearity, as if those terms are present, they will finally stabilize the system, leading to bounded motions. The bending shape and vibrations around the dynamic equilibrium position are quite similar to those that would occur if the structure was loaded with a lateral harmonic load. This phenomenon generally occurs for specific combinations of load amplitude, frequency and system characteristics (stiffness, mass, damping).

In the right side of figure 5, a pulse load with an amplitude bigger than the Euler buckling load of the bar is applied. The lateral displacement, in that case, increases monotonically (divergence) rather than oscillating as in the bar on the left, followed by random aperiodic oscillations around the new equilibrium position. Interaction between the global and local dynamic modes is occurring and the buckling mode consists of higher order harmonic shapes. This type of buckling is named as *"impulse (dynamic) buckling"* [19]. The term ''impulse'' is used to emphasize the relatively

high amplitude and sort duration of the applied axial load. The definition of impulse dynamic buckling is: *Instability onset due to transient response to a pulse load.*

Impulse dynamic buckling occur for pulse loads with intermediate amplitude (bigger but of the same order, comparing to the static buckling capacity) and duration close to the fundamental natural flexural period of the system [22].

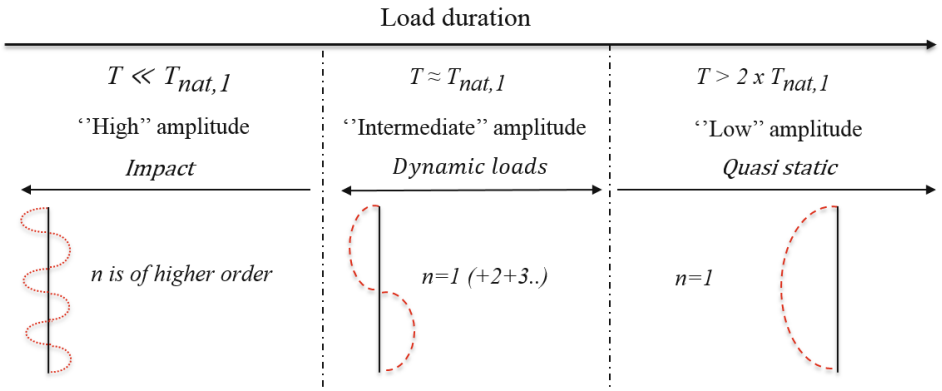

Figure 6: Classification of loading.

For the impact loading and the quasi-static loading regime, the loading can be modeled by considering only the loading magnitude. The effect of loading duration can be neglected (Hong Hao et.al. 1999). For the dynamic loading regime, the duration, amplitude and shape of loading pulse defines the response of the structure.

2.6.2. Dynamic stability of cylindrical shells in the marine environment.

During offshore pipe-laying operations, the heave motion of the installation vessel results in a time varying effective tension. This fluctuation can induce the aforementioned qualitatively different mechanisms of global stability loss. Either the lateral vibrations of the pipe can be excited, amplifying the amplitudes of the lateral motion (parametric resonance), or the dynamic component of the effective tension can become negative into a segment of the pipe for a part of the wave loading, leading to an undesirable pulsating compressive loading (impulse dynamic buckling).

When looking at a rapid varying axial loading of imperfect cylindrical shells, dynamic effects become important as dangerously large dynamic stresses can occur in this case. The onset of impulse dynamic buckling results in a sudden, divergent motion both in the in and out of plane directions, leading to high deflection amplitudes and amplified resultant strains. The post-buckling behavior is being characterized by the onset of random, aperiodic vibrations. This phenomenon is considered to be catastrophic for those type of structural elements [20]. The system is violently moved, with a finite jump from an initially stable state to a final stable state [21], because of the existence of the hydrodynamic damping and geometrical non-linearity. In the absence of those, the system would exhibit an infinite jump to a final unstable state.

On the other hand, it has been proven that parametric resonance cannot hamper the pipe's structural integrity. That type of instability induces low strains [2] and can be accepted during pipe-laying operations as it is relatively quickly damped by the drag force. For that reason, focus will be given on the instability caused by the compressive pulse loading.

2.7. Dynamic buckling criteria

As mentioned before, dynamic impulse buckling is not a failure mode, but a type of instability. Dynamic instability can take place only for imperfect structures. For that reason, there is no bifurcation load and a relevant dynamic buckling criterion should be applied for the identification of the critical dynamic buckling load. For various load amplitudes, buckling is assumed to have occurred when the load reaches a critical value associated with a maximum allowable stress or deformation, the magnitudes of which are defined according to the design requirements. Thus, there is no universally accepted criterion for dynamic buckling identification and no general guidelines for the design.

Various methods for determining the critical conditions for the onset of dynamic buckling exist. Each of those has its pros and cons concerning the accuracy and effort that is needed to be made in order to be applied. Those that are convenient to use in combination with numerical solvers are being presented in the following sub-chapters.

2.7.1. Budiansky and Roth

The most popular one was formulated by Budiansky and Roth, in 1962: *The critical dynamic buckling load is defined as the value of the load at which deflection grows rapidly for a small variation in load amplitude.* The load value, at which a sudden change in the response occurs, is called critical load for that particular load duration. Solving the equations of motion and plotting the displacement versus time by increasing the intensity of the applied load, a finite jump of the displacement is taking place for a small load increase. The load for which the "jump" occurs is the critical dynamic buckling load P_{cr}.

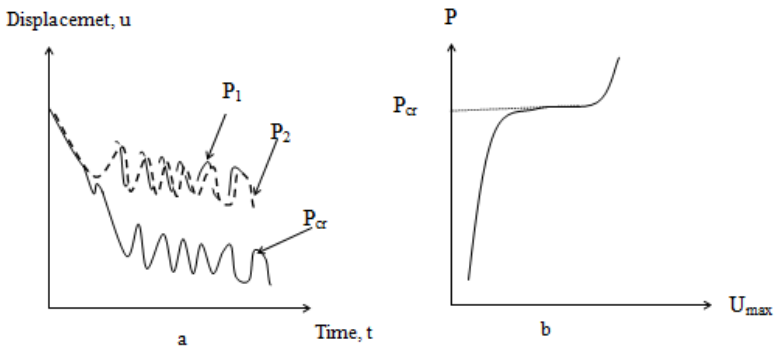

Figure 7: Budiansky and Roth dynamic buckling criterion. Courtesy (Touati et.al 2012).

2.7.2. The phase plane approach

The phase plane, introduced by Hoff & Bruce in 1954, is a graphical approach to evaluate the stability of a dynamic system. It is drawn in a velocity – displacement coordinate system. Stable systems correspond to bounded motions, where the displacements are drawn in closed paths, limited and focused around the dynamic equilibrium position. When the loading increases, it is possible for an escaping motion to occur, where a movement of the structure gets away of the pole without oscillating around him. In that case, instability occurs and the corresponding load is the critical buckling load.

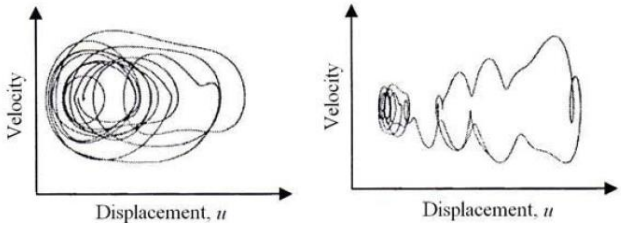

Figure 8: Stable (left) and unstable (right) motion. Courtesy (Touati et.al 2012).

In the first case, the motion is named bounded because if the simulation time increases, the corresponding motion envelope will remain unaffected, while an unstable motion is growing over time (unbounded motion). During pipelay installation, because of the existence of the drag force and because of the geometrical non-linearity of the pipe, the system will stabilize again after the occurrence of the escaping motion. The escaping motion will be still visible though and its occurrence corresponds to the onset of instability.

The same can be applied in any physical quantity that one wants to assess over time. By plotting the phase plain of the strains, one can get a better illustration of the stress scheme in the system.

2.8. Impulse - momentum theorem

In classical mechanics, impulse is the integral of a force *F*, over the time interval of application *t*. The impulse-momentum theorem states that the change in momentum of an object equals the impulse applied to it. Impulse is a quantity which demonstrates the effect of a force acting on an object. For a system with a constant mass *m*, using the Newton's second law the impulse is defined as follows:

$$J = \int_o^t f(x)\, dt = m \int_o^t (a) dt = m\, \Delta v = \Delta P \qquad [2.10]$$

Where J is the impulse, ΔP is change in momentum, v is velocity, a is acceleration and m is the mass of the object.

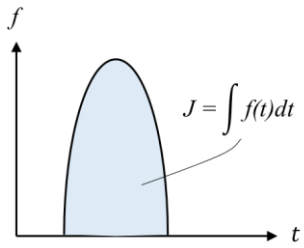

Figure 9: Impulse.

Given that the dynamic buckling capacity depends on the applied load amplitude, duration and shape of the applied pulse load, the impulse can be used to define the buckling capacity of the pipe in terms of the change in momentum needed for the pipe to develop an escaping motion (Simitses, 2012).

3

Dynamic elastic buckling of curved beam. Analytical vs FE model

3.1. Introduction

An analytical model using the matrix based MATLAB language, capturing the physics of the problem in hand, is developed. Hoff's formulation [3] of the buckling problem for a naturally curved, simply supported Euler Bernoulli beam model, is being recalled and modified to account for periodic, motion driven excitation. The theory of moderately large displacements is applied. Perfectly elastic material is considered. Direct comparison with an identical Flexcom model is performed. Constant and sinusoidal velocity loading is applied to the movable support of the beam for the following reasons:

- Applying a constant velocity loading, the dependence between the movable support velocity and critical buckling load can be explicitly defined.

- In order to demonstrate the effect of loading duration, a half-sine displacement pulse is applied for different time durations.

- A sinusoidal motion loading with constant amplitude, replicates the action of a regular sea state that leads to compressive oscillatory loading. The ability of Flexcom to accurately capture the onset of impulse dynamic buckling is validated and the difference between impulse dynamic buckling and parametric resonance is demonstrated.

- A sinusoidal motion with linearly increasing amplitude is applied. This loading is used to identify the critical loading conditions for the onset of instability (critical axial motion amplitude per loading frequency). This will be further utilized in chapter 5 for conducting the stability assessment against regular and irregular excitation for the base cases.

3.2. Analytical model mathematical formulation

In this section, the analytical model's mathematical formulation is presented. The adopted assumptions, boundary conditions and the solution for constant and sinusoidal velocity loading are given.

3.2.1. Formulation of the EOM of the lateral motion of the curved beam

An initially imperfect (curved, stress-free), simply supported beam of length *L*, is subjected to a time varying axial motion *f(t)* of its movable support. The beam end is moving, along the longitudinal axis *x*, with a velocity $v=\dot{f(t)}$, as it is depicted in the following figure.

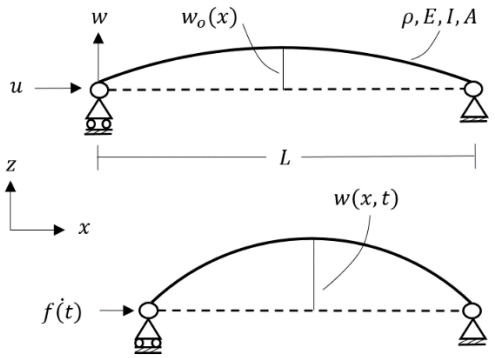

Figure 10: Initial (top) and current (bottom) configuration of the simply supported, imperfect beam subjected to time dependent axial displacement loading.

The following equations, subjected to the suitable boundary and initial conditions, represent a complete system of equations for determining the three unknown space and time-dependent quantities which characterize the column motion: the lateral deflection w, the axial displacement u, and the axial force *P*, due to the imposed displacement*:*

$$EI\frac{\partial^4(w-w_o)}{\partial x^4}+P(t)\frac{\partial^2 w}{\partial x^2}+\frac{\rho_s A\partial^2 w}{\partial t^2}=0 \qquad [3.1]$$

$$-\frac{\partial P}{\partial x}=\rho_s A\frac{\partial^2 u}{\partial t^2} \qquad [3.2]$$

$$P(t)=\frac{EA}{L}\left(f(t)-\frac{1}{2}\int_0^L\left(\left(\frac{\partial w}{\partial x}\right)^2-\left(\frac{\partial w_o}{\partial x}\right)^2\right)dx\right) \qquad [3.3]$$

Where, $w_o(x)$ is the initial imperfection, *E* is the modulus of elasticity, *I* is the cross sectional moment of inertia, *A* is the cross sectional area and ρ_s is the density of steel.

Equation [3.1] expresses the equilibrium of the column in the lateral direction [10]. Equation [3.2] expresses the equilibrium of the column in the axial direction. Equation [3.3] is the nonlinear axial strain displacement relation, based on the moderately large displacements of the beam. The mid plane stretching of the beam is taken into account. Assuming finite rotations, the bending of the beam contributes to the axial strain of the beam.

3.2.2. Model assumptions

The longitudinal force is assumed to be constant along the beams length.

Equation [3.1] involves the assumptions of linearly elastic material behavior, small displacements and uniform geometrical and physical properties along the pipe. It neglects rotatory inertia and effects due to shear strains and Poisson's ratio, complying with the Euler Bernoulli beam theory.

The nonlinear terms in the equation [3.3], represent axial components of the strain due to bending of the beam. The validity of this theory is being retained for angles that do not exceed 10^o. Consequently, the lateral displacements should not exceed 1.8 m (small strain assumption) [9]. More information around the moderately large displacement theory, along with the derivation of equation [3.3], can be found in Appendix part A.1 and A.2 respectively.

For constant velocity loading and for conventional engineering materials like steel, in order for the small strains assumption to be valid until the time that the critical buckling load is reached, the following inequality should hold [10].

$$\frac{f(\dot{t})}{v_S} < 0.001, \qquad v_S = \sqrt{E/\rho_s}, \qquad E = 2{,}1\times10^{11}\ \text{Pa},\ \rho_s = 7859\ \frac{\text{kg}}{\text{m}^3}$$

$$\xrightarrow{yields}\ f(\dot{t}) < 5.172\ \text{m/s} \qquad [3.4]$$

Where, v_S is the longitudinal speed of the compressive waves in steel.

It has been proven that the effect of axial inertia effect is not of significant importance, as the gross elastic response of conventional structural members (those with slenderness ratio less than 150) under compression is concerned [10]. This is based on the hypothesis that the time required for an axial pressure wave to travel from the one end of the column to the other is at least one order of magnitude shorter, compared to the time necessary for the lateral displacements to develop at the critical buckling load.

Equation [3.2] is then dropped, as the axial inertia term on the right hand-side of the equation is taken equal to zero.

Summarizing the aforementioned assumptions, the system of equations [3.1], [3.3] can be used to accurately obtain the critical buckling load under the following conditions:

1. Material is fully elastic.
2. The longitudinal force *P* is constant throughout the beams length.
3. Lateral displacements do not exceed 1.8 m (small strains assumption).
4. The slenderness ratio is less than 150.

3.2.3. Solution of the EOM for constant and sinusoidal velocity loading

Inserting equation [3.3] into [3.1] results:

$$EI\frac{\partial^4(w-w_o)}{\partial x^4}+\frac{EA}{L}\left(f(t)-\frac{1}{2}\int_0^L\left(\left(\frac{\partial w}{\partial x}\right)^2-\left(\frac{\partial w_o}{\partial x}\right)^2\right)dx\right)\frac{\partial^2 w}{\partial x^2}+\frac{\rho A\partial^2 w}{\partial t^2}=0 \qquad [3.5]$$

Solving the above partial integro-differential equation, one get can the response of the imperfect beam for the displacement loading scheme.

The lateral deflection *w(x,t)*, is taken as a Fourier sinusoidal series:

$$w(x,t)=\sum_{n=1}^{\infty}W_n(t)sin\left(\frac{n\pi x}{L}\right),\qquad n=1,2,\dots,N \qquad [3.6]$$

The initial shape of the beam is assumed to follow the first mode of vibration of the beam (*n=1*):

$$w(x,0)=w_o(x)=W_o\sin\left(\frac{\pi x}{L}\right) \qquad [3.7]$$

For a simply supported beam, the following boundary conditions should be applied:

$$w(0)=w(L)=0\quad \frac{\partial^2 w}{\partial x^2}(0)=\frac{\partial^2 w}{\partial x^2}(L)=0 \qquad [3.8]$$

Equation [3.6] automatically satisfies the boundary conditions for a simply supported beam.

Inserting equations [3.6] and [3.7] into [3.5], yields:

$$\sum_{n=1}^{N}\left[EI\left(\frac{n\pi}{L}\right)^4W_n(t)+\ddot{W_n}(t)\rho A-P_n\left(\frac{n\pi}{L}\right)^2W_n(t)\right]\sin\left(\frac{n\pi x}{L}\right)-EI\left(\frac{\pi}{L}\right)^4W_o\sin\left(\frac{\pi x}{L}\right)=0 \qquad [3.9]$$

with,

$$P_n = \frac{EA}{L}\left(f(t) - \frac{1}{2}\int_0^L \left(\left(\sum_{n=1}^{N} \left[W_n(t) \left(\frac{n\pi}{L}\right) \cos\left(\frac{n\pi x}{L}\right) \right] \right)^2 - \left(W_o \left(\frac{\pi}{L}\right) \cos\left(\frac{\pi x}{L}\right) \right)^2 \right) dx \right) \quad [3.10]$$

Equation [3.9] is solved for the first buckling mode (*n=1*). For a non-linear PDE the simple modal superposition principle does not apply [23]. This is because taking into account more modes results in a coupled system of modal equations. It has been shown that the first buckling mode provides an accurate approximation for low buckling levels. The onset of dynamic buckling can be approximated using the first mode of vibration [24].

Setting *n=1* in equation [3.9] yields,

$$EI\left(\frac{\pi}{L}\right)^4 (W_1(t) - W_o) - P_1\left(\frac{\pi}{L}\right)^2 W_1(t) + \ddot{W_1}(t)\rho A = 0 \quad [3.11]$$

with,

$$P_1 = \frac{EA}{L}\left(f(t) - \frac{1}{2}\pi^2 \left(\frac{W_1(t)^2 - {W_o}^2}{2L} \right) \right) \quad [3.12]$$

Equation [3.11] is being solved with an ordinary differential solver in MATLAB (ODE 45), subjected to the following initial conditions:

$$W_1(0) = W_o \quad [3.13]$$

$$\frac{\partial W_1}{\partial t}(0) = 0 \quad [3.14]$$

The initial deviation of the center line of the beam from the straight line, along which the axial compressive load is acting, is assumed to be equal to the initial imperfection. The lateral velocity of the points along the longitudinal axis of the beam is zero at the beginning of the analysis. The information about the type of the loading is inserted by modifying the axial displacement function $f(t)$.

Constant velocity loading: The beam end is moving towards the other with a constant velocity $\dot{f}(t)=v$, along the longitudinal axis x. Inserting $f(t)=vt$, into equation [3.11] yields the equation of motion of the lateral motion of an imperfect beam, under constant rate of displacement.

$$EI\left(\frac{\pi}{L}\right)^4 (W_1(t) - W_o) + \ddot{W_1}(t)\rho A - P_1\left(\frac{\pi}{L}\right)^2 W_1(t) = 0 \quad [3.15]$$

with,

$$P_1 = \frac{EA}{L}\left(vt - \frac{1}{2}\pi^2\left(\frac{W_1(t)^2 - {W_o}^2}{2L}\right)\right) \quad [3.16]$$

Sinusoidal velocity loading: The motion of the movable support along the longitudinal axis *x* is following a sinusoidal function. Inserting *f(x)=Dsin(ωt)*, where, *D* is the amplitude and *ω* the radial frequency of the imposed axial sinusoidal motion, into equation [3.11] yields the equation of motion of the lateral motion of the imperfect beam, under sinusoidal motion of the moving end.

$$EI\left(\frac{\pi}{L}\right)^4 (W_1(t) - W_o) + \ddot{W_1}(t)\rho A - P_1\left(\frac{\pi}{L}\right)^2 W_1(t) = 0 \quad [3.17]$$

with,

$$P_1 = \frac{EA}{L}\left(Dsin(\omega t) - \frac{1}{2}\pi^2\left(\frac{W_1(t)^2 - {W_o}^2}{2L}\right)\right) \quad [3.18]$$

3.3. Flexcom FE Model

3.3.1. Flexcom model assumptions

The finite element development is based on the assumption that strains are small and elastic under arbitrarily large three-dimensional displacements and rotations. A convected axis system is used, which moves with the element as it displaces in space. Deformations along the element relative to this system are assumed to be moderate.

3.3.2. Geometrical and material characteristics.

In order to comply with the analytical model assumptions, a horizontal pipe will be modeled, ensuring that the longitudinal force will remain unaffected by the mass of the beam, staying constant along the length of the pipe. No surrounding fluid (water) was taken into account. The model's structural configuration and physical characteristics are being represented in the following figure and table.

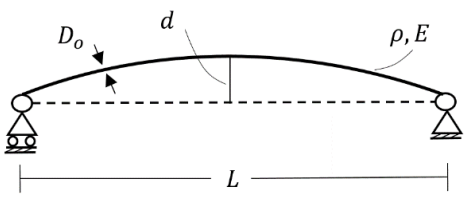

Figure 11: Flexcom model structural configuration.

Table 1: Flexcom model properties.

Water depth (m)	0
Steel density (kg/m^3)	7850
Modulus of elasticity (GPa)	210
Mass per unit length (kg)	220.76
Inner steel pipe diameter (m)	0.54
Outer steel pipe diameter (m)	0.58
Coefficient of friction	0
Slenderness ratio	100
Length (m)	20
Imperfection at mid-span (m)	0.02

Special care was given to find a combination of the above that yield a slenderness ratio lower than 150, to comply with the analytical model assumptions stated in chapter 3.2.2. The model consists of 1000 beam elements. When the effective compression in an element achieves the theoretical element compression limit, the solution becomes numerically unstable and will terminate. The static buckling capacity of each element was checked to be larger than the maximum axial force encountered during the analyses. The static (Euler) buckling load $P_{cr,static}$ for each element, should be higher than the resulting internal axial load from the imposed displacement.

$$P_{cr,static} = \frac{\pi^2 EI}{k\left(\frac{L}{1000}\right)^2}, \qquad k = 1\ (simply\ supported), \qquad I = \frac{\pi\left({D_o}^4 - {D_i}^4\right)}{64}$$

$$\xrightarrow{yields} P_{cr,el} \approx 10^9 \text{ mT} \qquad [3.19]$$

3.4. Load cases and results

Hereby, Flexcom's FE analyses results are being compared against the numerical solution of the analytical model. The validation procedure is performed for the range of parameters that render the analytical model's assumptions valid [see chapter 3.2.2].

3.4.1. Constant velocity loading

A constant rate of displacement (constant velocity) is applied to the movable support. Two loading cases will be considered, as illustrated in the following table.

Table 2: Constant velocity load cases.

Load case	Velocity (m/s)
A	0.1
B	0.5

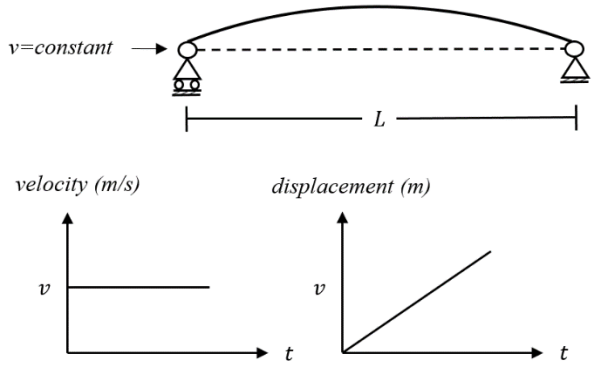

Figure 12: Constant velocity loading.

In the following figures, the displacement and axial force of the middle point of the beam ($x = L/2$) are plotted against time. The simulation time is set to 1s, so for different applied velocities, the movable beams end is covering different distances.

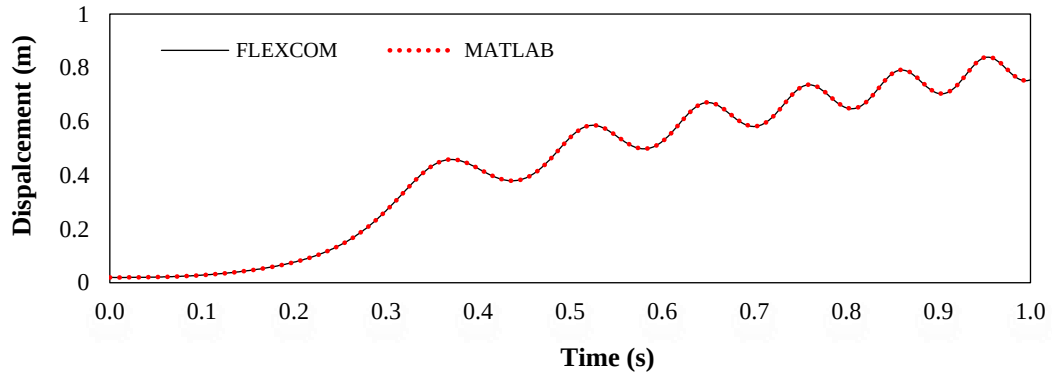

Figure 13: Lateral deflection at midspan, load case A.

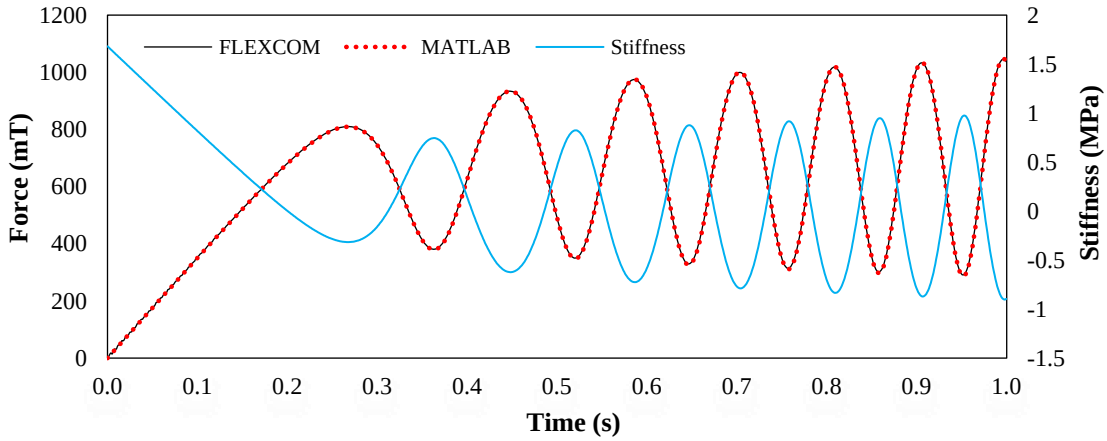

Figure 14: Axial force at midspan and stiffness, load case A.

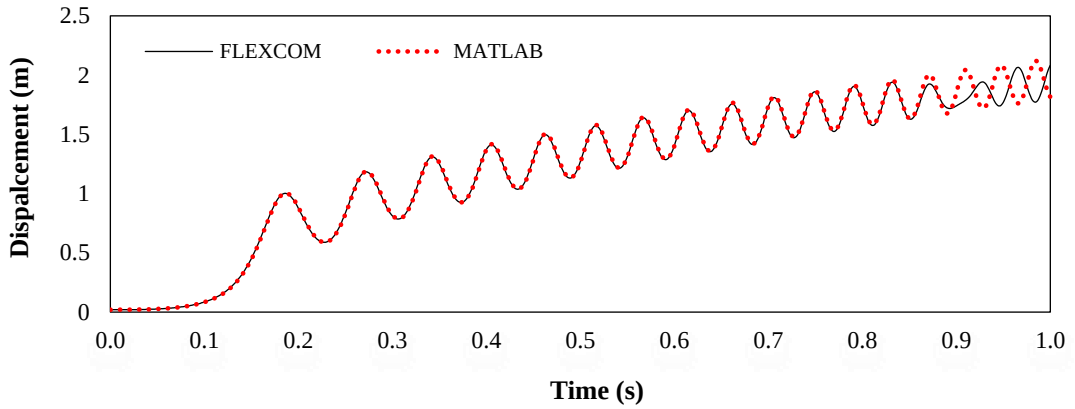

Figure 15: Lateral deflection at midspan, load case B.

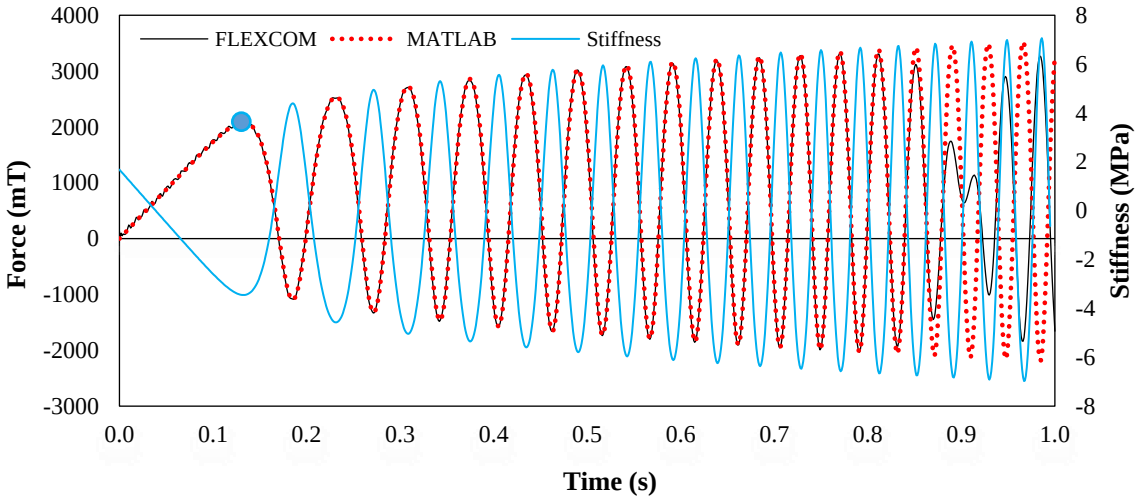

Figure 16: Axial force at midspan and stiffness, load case B.

Load case A: Complete agreement in terms of displacement and force, between the models, is depicted in figures 13 and 14. For a total axial tip displacement of 0.1m, the first mode approximation can accurately calculate the response of the pipe.

Observing figure 16, one can notice that approximately after 0.05s, the system has negative stiffness and the lateral deflection is increasing rapidly. However, according to the Budiansky and Roth criterion (see chapter 2.7.1), buckling occurs at the first local maxima of the axial force. This happens at 0.12s (blue dot on plot) for a force of around 800 mT. There is a "time lag" between the force application (application of strain due to axial motion of the tip) and the development of deflection. This is because of the inertial force, which acts in the opposite direction of the deflection, retarding the motion of the system. Consequently, a specific amount of time is needed for the system to buckle (develop finite jump in displacement). The time to buckle increases for increasing velocities. Comparing figures 14 and 16 one can notice that the moment that the stiffness gets negative is "further away" from the moment of buckling onset for the bigger velocity loading.

Load case B: From figures 15 and 16, one can observe that after approximately 0.9s and a displacement of the movable end equal to 0.45m, an interaction of modes is occurring. The first mode approximation is not accurate after 0.9s. However, this interaction occurs for deflections of the middle point that exceeds the upper limit for the validity of the moderately large displacement theory (1.8m, see 3.3.2.) and even a multi-modal approximation would be inaccurate.

From figure 14, it is seen that the pipe, for a velocity of the moving end equal to 0.5 m/s, buckles at a higher force (2000 mT), comparing to 600 mT for the 0.1m/s velocity case. This is due to inertia, as the pipe-span develops higher accelerations for higher velocity excitations and the lateral motion of the pipe is being further restricted as the compression rate (velocity of moving end) increases. For higher velocities and for the same total displacement of the movable support, the lateral displacement is smaller. As a result, the onset of buckling occurs in a higher compressive force. This is more obvious in the forthcoming plot, where the forces for the onset of buckling, are collected and plotted for a range of velocities from 0.001 to 0.50 m/s. Then, the variation of the DLF with velocity and the related similarity number is plotted.

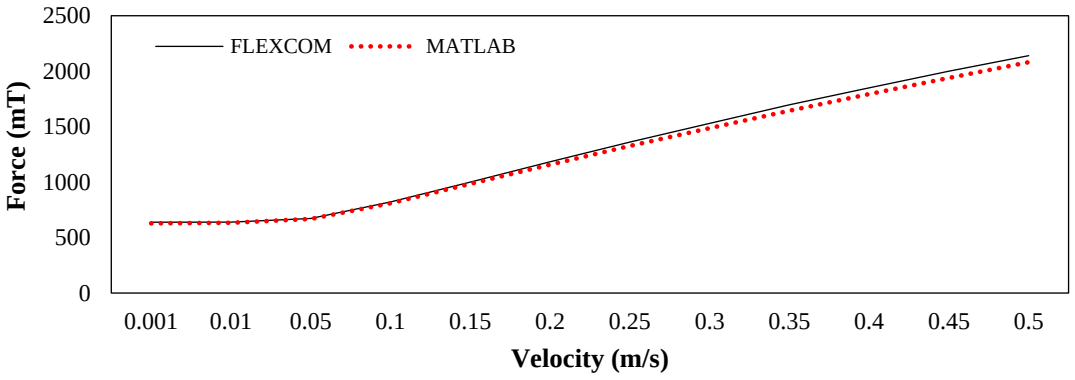

Figure 17: Critical axial force vs loading velocity.

Table 3: Critical buckling load vs loading velocity.

Velocity (m/s)	**0.001**	**0.05**	**0.10**	**0.20**	**0.30**	**0.40**	**0.50**
Flexcom Force (mT)	638.7	672.3	821.4	1183.5	1530	1849.5	2140
Analytical Force (mT)	628.5	668.4	809.3	1158	1487	1793	2081

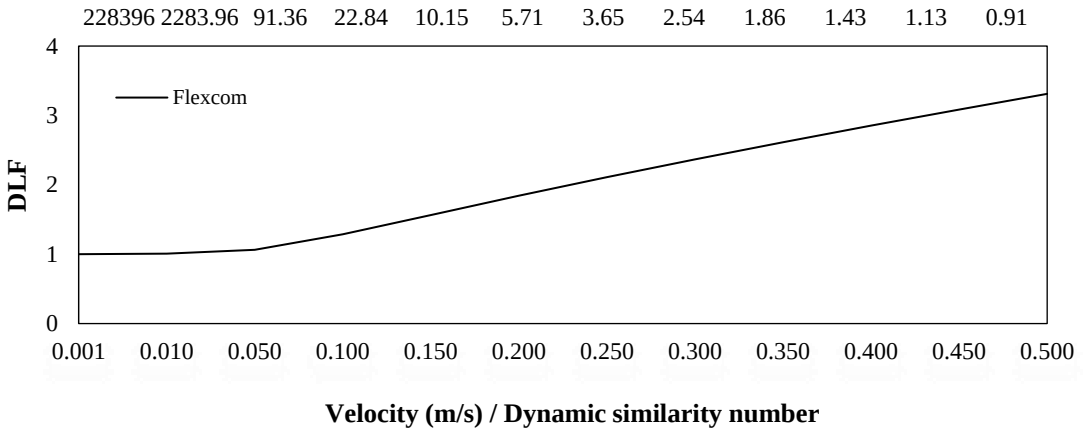

Figure 18: Dynamic load factor (DLF) vs velocity vs Hoff's similarity number.

Observing figure 18, it can be seen that for small velocities, the static buckling capacity of the pipe is being measured. For bigger velocities, the DLF is growing as the dynamic buckling capacity is increasing over the static with increasing velocities of the movable support. From figure 17 it is visible that he critical buckling load of the analytical model is becoming increasingly smaller than the finite element model predicts. This is because the analytical model slightly overestimates the lateral deflection, due to the zero axial inertia assumption.

3.4.2. Half-sine displacement pulse loading

A half sine axial displacement pulse with an amplitude of 0.07 meters is applied for different loading durations.

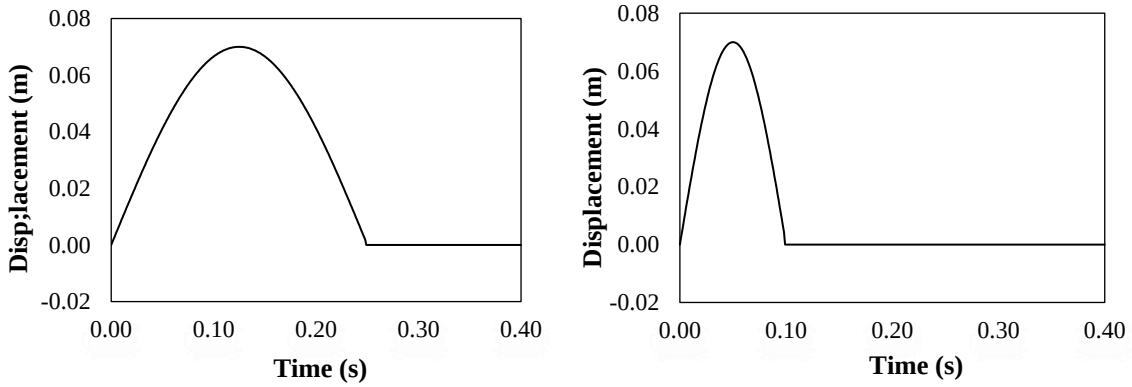

Figure 19: Two half sin displacement pulses with the same amplitude and different load duration (0.2s left , 0.1s right).

In the following figure the displacement of the middle point is being plotted against time for the left pulse of figure 19.

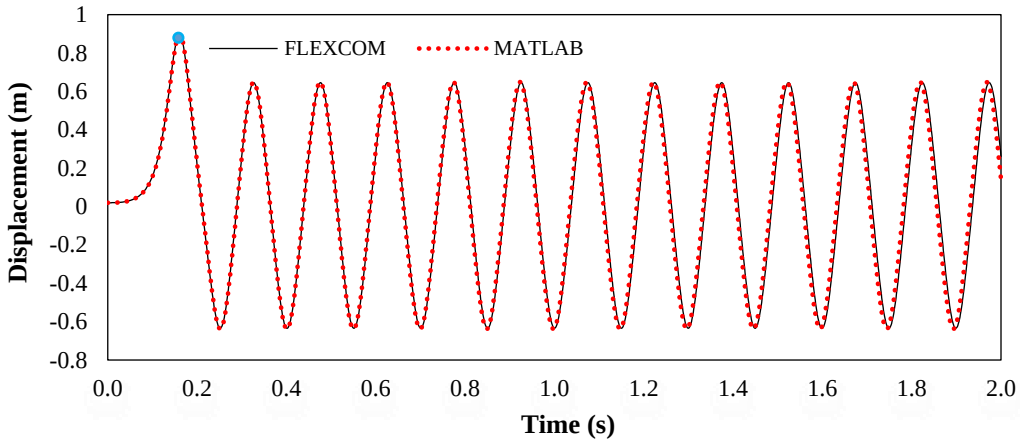

Figure 20: Deflection at midspan under half sine displacement loading with 0.07m amplitude, 0.25s load duration.

The maximum deflection of the middle point is highlighted with the blue dot. Due to geometrical non-linearity after the end of the applied excitation, the deflection decrease until it vanish. The maximum deflection of the middle point is plotted against the load duration of the applied displacement pulse.

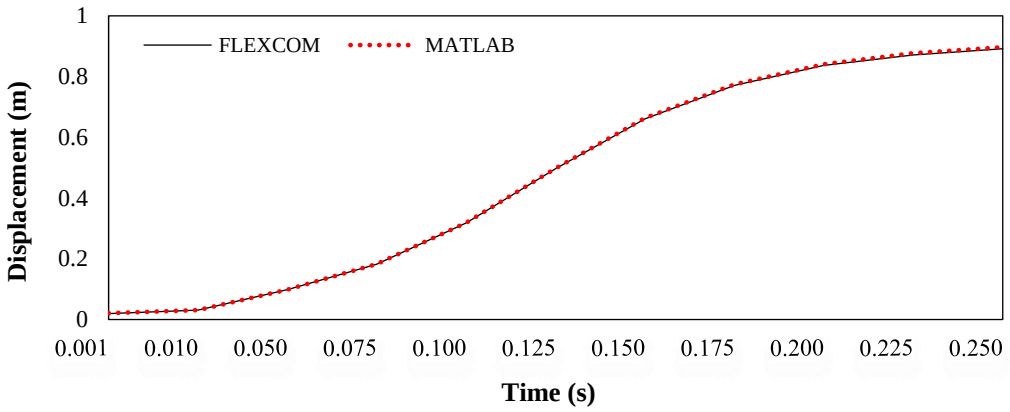

Figure 21: Maximum deflection at midspan vs displacement pulse load duration.

From figure 21 we can observe that the maximum deflection of the pipe is being significantly affected by the loading duration. As the loading duration decreases, the maximum deflection is reduced. This is because a specific amount of time is needed for the pipe to develop deflection due to the imposed axial motion. In accordance with chapter 3.4.1, this is an inertial effect. For the same displacement amplitude, a motion with shorter duration exhibits higher velocity and consequently acceleration, increasing the inertial force which retards the deflections of the system.

Complete agreement between the two models occur, validating the ability of Flexcom to model the transient response of the system due to sudden dynamic loading, given that a small enough time-

step is used. A time-step between 0.01 and 0.001 s was required to accurately conduct the validation procedure.

3.4.3. Sinusoidal displacement loading: constant amplitude

Two loading cases will be considered as illustrated in the following table.

Table 4: Constant displacement amplitude sinusoidal motion load cases

Load case	Displacement Amplitude (m)	Period (s)	Simulation time (s)
A	0.07	0.06	30
B	0.07	0.25	30

A representative plot of the applied excitation is given below.

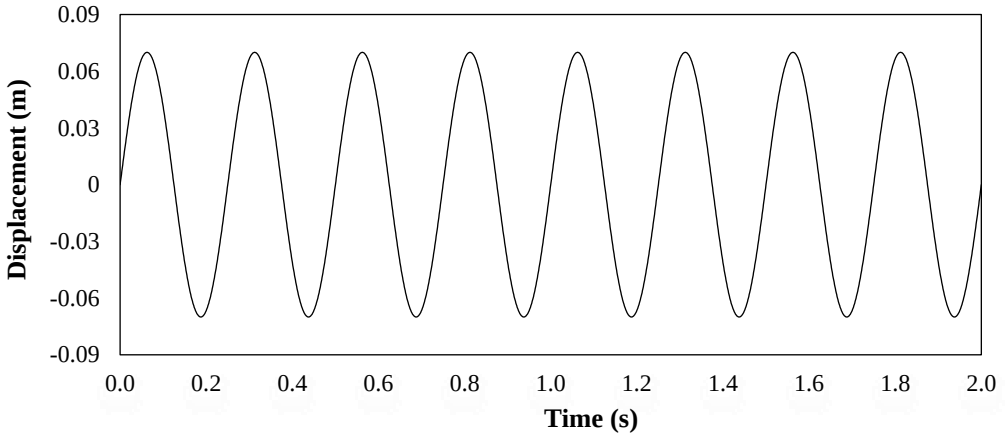

Figure 22: Constant displacement amplitude sinusoidal loading, case B

The first three flexural natural periods of the pipe are presented in the table below.

Table 5: Fundamental flexural periods

Natural period number	Period (s) FLEXCOM	Period (s) Analytical
1	0.2540	0.2546
2	0.0637	0.0636
3	0.0283	0.0283

In the following figures, the displacement of the middle point of the beam is plotted against time for two different simulation durations. Plots covering the full simulation can be found in Appendix part B.1.

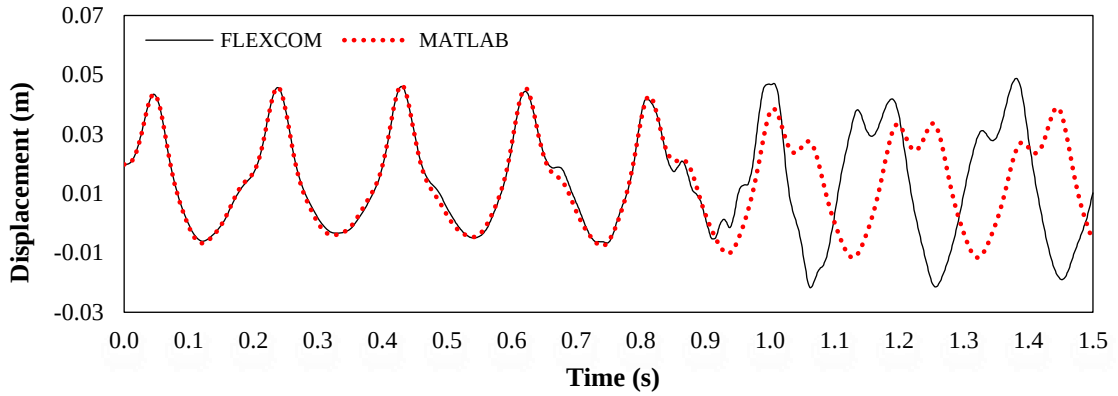

Figure 23: Lateral deflection at midspan, load case A, simulation interval: 0 - 1.5 s.

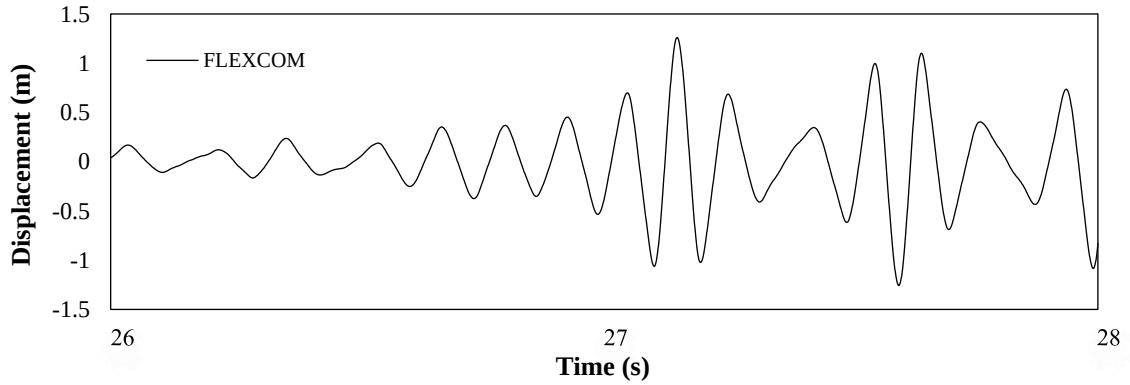

Figure 24: Lateral deflection at midspan, load case A, simulation interval: 26 – 38 s.

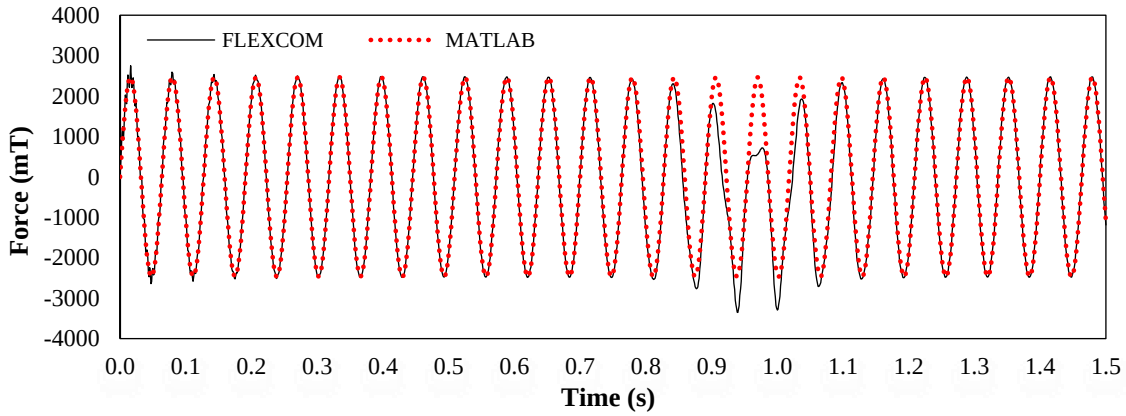

Figure 25: Axial force at midspan, load case A, simulation interval: 0 - 1.5 s.

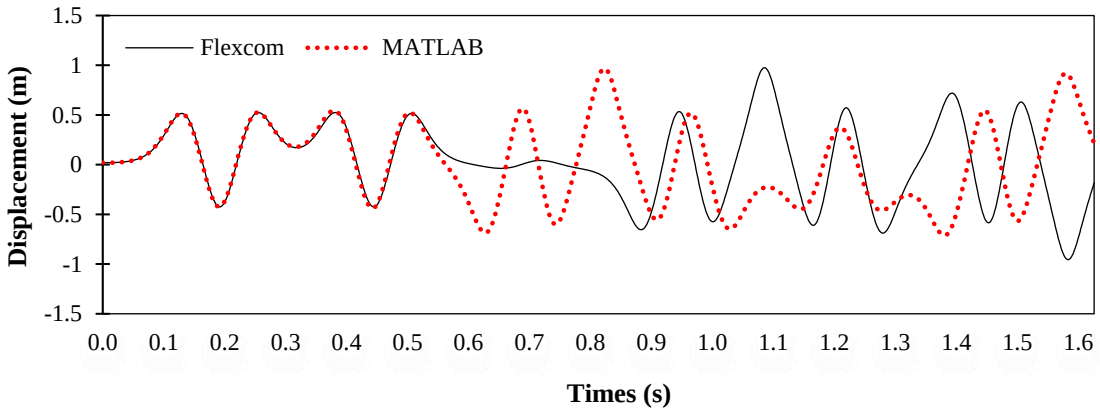

Figure 26: Lateral deflection at midspan, load case B, simulation interval: 0 - 1.5 s.

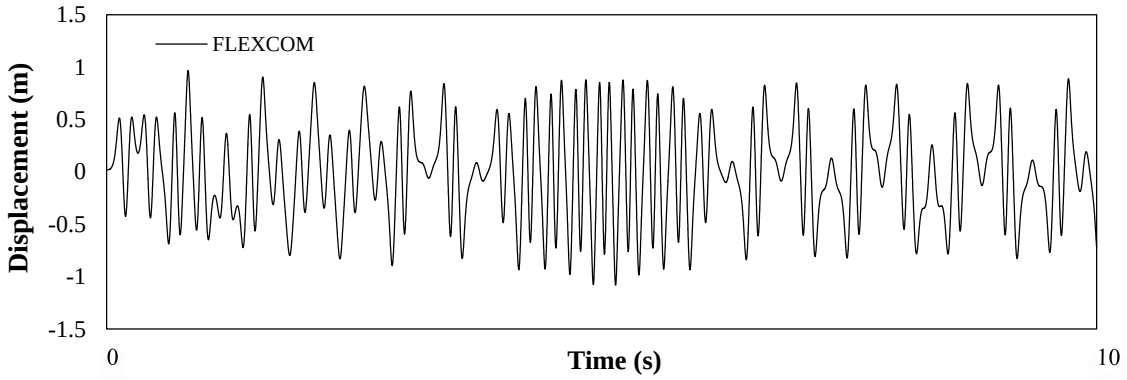

Figure 27: Lateral deflection at midspan, load case B, simulation interval: 0 - 10 s.

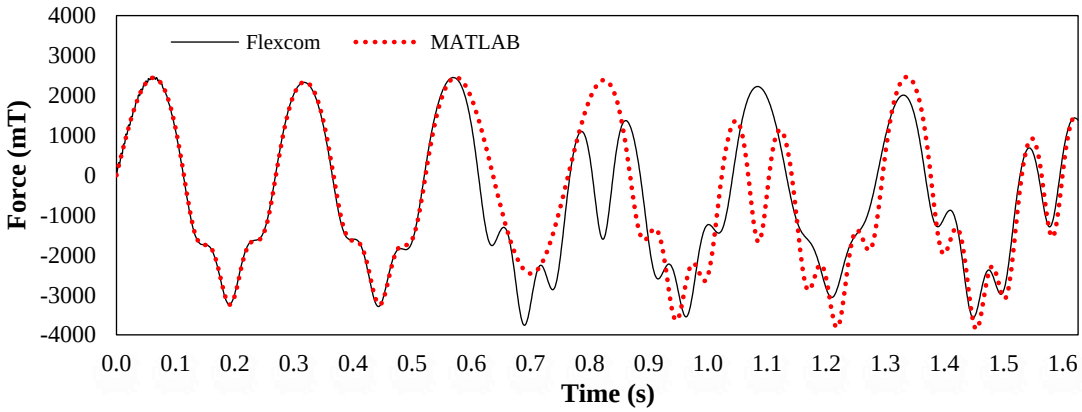

Figure 28: Axial force at midspan, load case B, simulation interval: 0 - 1.5s.

Load case A: Observing figures 23 and 24, one can notice that the middle point deflection is growing with time, resembling to a forced resonant vibration. This is due to parametric resonance as in this case the loading frequency equals four times the fundamental natural frequency, being close to the second natural frequency of the system. It has been shown that, in contrast with the

forced excitations, in case of parametric loading, the response of the system can be magnified significantly even if the frequency of loading is away from a natural frequency [19]. This phenomenon occurs for specific combinations of loading amplitude, frequency and physical characteristics of the system.

Around 26s, large amplification of the lateral deflection occurs, and according to the Budiansky and Roth dynamic buckling criterion (see chapter 2.7.1) buckling is initiated. The resultant displacements are not unbounded, because of the geometrical non-linearity. However, it has been proved that this cannot occur in the marine environment, because of the existence of hydrodynamic dissipation [17]. The growth of response is damped out, before the appearance of dangerously large deflections.

Load case B: From figures 26 and 27, one can observe that the deflection of the middle point grows monotonically from the beginning of the simulation (divergence). This is characteristic of the onset of impulse dynamic buckling. The structure undergoes unacceptably large deformations under short duration of time. Again, the resultant deflection is not unbounded, because of the existence of the geometrical nonlinearity. In that case, buckling didn't occur because of the periodic time variation of the axial force. Instead, it occurred due to the generated pulsating compressive loading (figure 28) (short duration - high amplitude compressive axial force, see chapter 2.6.1).

From figure 28, one can visualize the complete agreement between the models until $t = 0.5$ s. Then, an interaction of modes occur and deviation of the responses between the models occur. This is not important for the identification of the impulse dynamic buckling onset. For this, the first mode approximation suffices. The effect of the generated pulsating compressive load duration is obvious. From figures 24, 27 we can observe that, for the same loading amplitude, a different load duration can trigger a qualitatively different instability mechanism.

3.4.4. Sinusoidal displacement loading: linearly ramped amplitude

The goal is to calculate the critical axial motion of the movable support per loading frequency. A sinusoidal motion with a linearly increasing (linear ramp function) amplitude throughout the whole simulation time is applied to the movable support of the beam.

This is done to generate incrementally bigger axial compressive impulses (see chapter 2.8) in order to "force" the system to destabilize. The response of the system under axial compressive pulse loading depends on the pulse characteristic – meaning amplitude, duration, and shape. This information can be quantified utilizing the impulse definition. The impulse is the integral of a force *F*, over the time interval of application *t*.

An illustration of the applied excitation and the resultant axial load is given below.

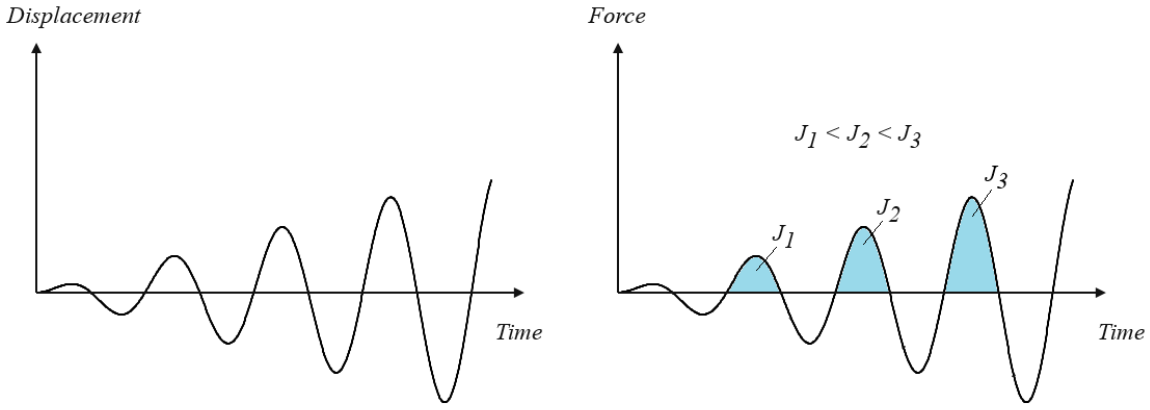

Figure 29: Applied displacement on movable support (left), resultant axial load at midspan (right).

The following loading conditions are analyzed.

Table 6: Load cases for sinusoidal motion with linearly ramped amplitude

Load case	Displacement Amplitude (m)	Period (s)	Simulation time (s)
A	0.06	0.212	50
B	0.06	0.196	50

In the following figure, the linear ramp of the displacement is demonstrated for load case A for a part of simulation time. The axial load and deflection of the middle point are being plotted against time for load cases A and B.

Plots for the total simulation duration can be found in Appendix part B.2.

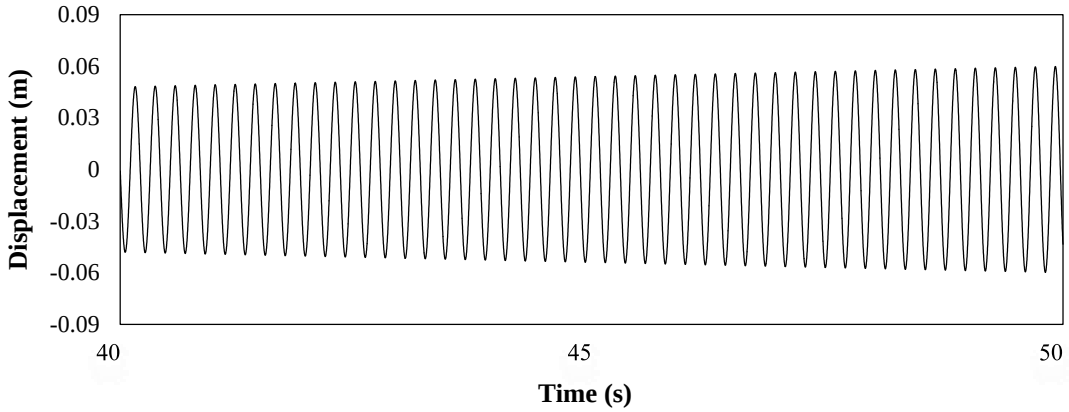

Figure 30: Linearly ramped, sinusoidal axial motion of movable support, simulation time: 40 – 50 s, load case A

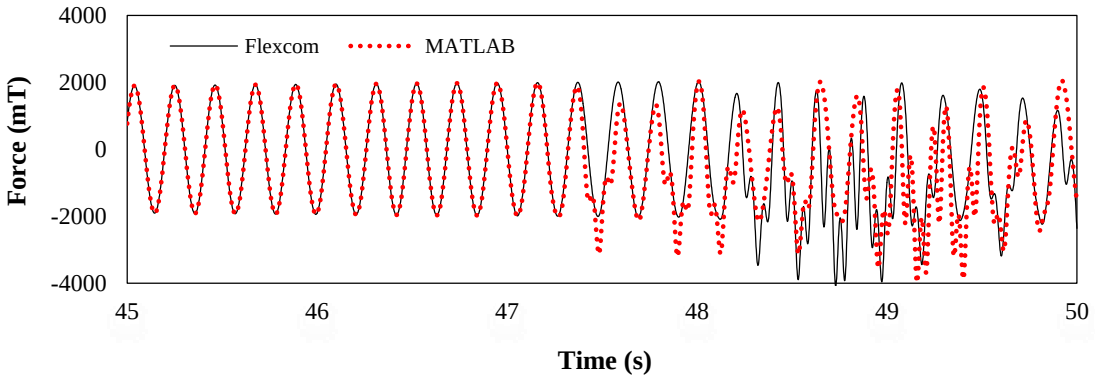

Figure 31: Axial force at midspan, load case A, simulation interval: 45 - 50 s.

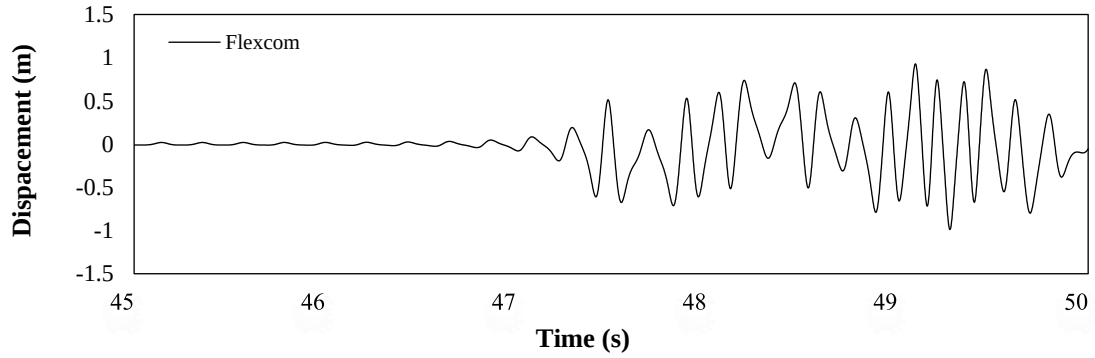

Figure 32: Deflection at midspan, load case A, simulation interval: 45 – 50 s.

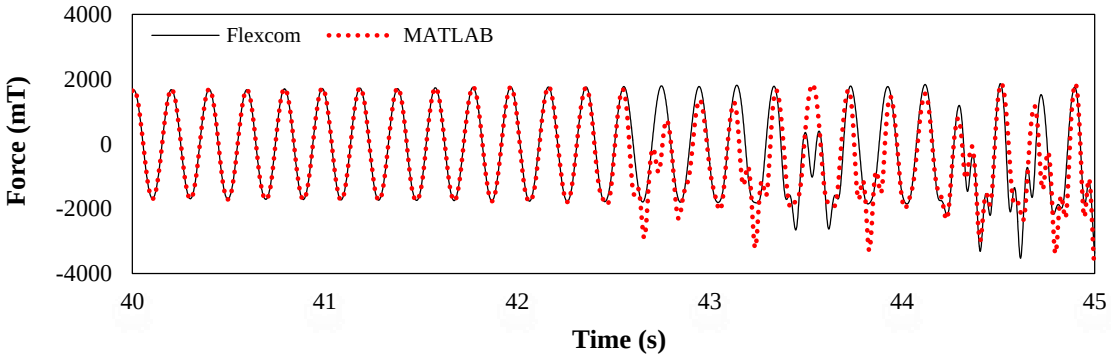

Figure 33: Axial force at midspan, load case B, simulation interval: 40 - 45 s.

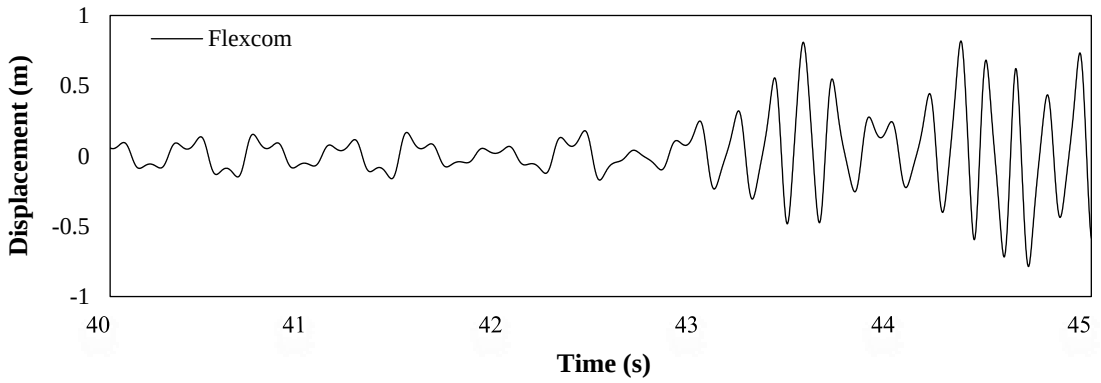

Figure 34: Deflection at midspan, load case B, simulation interval: 40 – 45 s.

According to the Budiansky and Roth dynamic buckling criterion buckling occurs when a leap in displacement occurs for small variation in the loading amplitude. Observing figures 32 and 34, one can notice that this moment is not straightforward and no conclusion can be derived regarding the onset of impulse dynamic buckling. This renders this criterion non-applicable for the problem in hand.

A different approach is proposed: *Buckling is assumed to occur when for a small increase in the displacement amplitude, a reduction in the resultant axial load of the system occurs.* This reflects alleviation of stress through excessive displacement.

According to that, the critical displacement amplitude for a specific excitation frequency can be identified. For load case A, a reduction in the resultant axial load of the system occurs at 47.34 s. The displacement amplitude at that moment in time is characterized as the critical axial motion amplitude for this specific period and integrating the corresponding compressive pulse load the critical impulse for the applied period of excitation is found. This will be used in chapter 5 for evaluating the stability of the system against irregular excitation. Consequently, the critical values of velocity and acceleration can be determined. The same procedure is applied for all load cases.

From figures 31 and 33 it can be seen, that the reduction in the axial load occurs sooner in the analytical model than in Flexcom. This is due to the axial inertia assumption (axial inertia is neglected in the analytical model), due to which, the analytical model slightly overestimates the deflections. The results are demonstrated in the following table.

Table 7: Critical axial displacement amplitude of movable support for the onset of impulse dynamic buckling.

Critical displacement (m)		
Load case	**Flexcom**	**Analytical**
A	0.057	0.056
B	0.053	0.051

The accuracy of the proposed method is increased for increasing simulation times, as more combinations of amplitudes for the selected excitation frequency are taken into account.

In order to visualize the instability onset, the phase plane plots of the middle point of the beam, for loading case A, are being plotted for three different simulation times. The first ends before the occurrence of the critical axial motion (46s), the second slightly after (47.5s) and the third ends at the end of the total simulation time (50s).

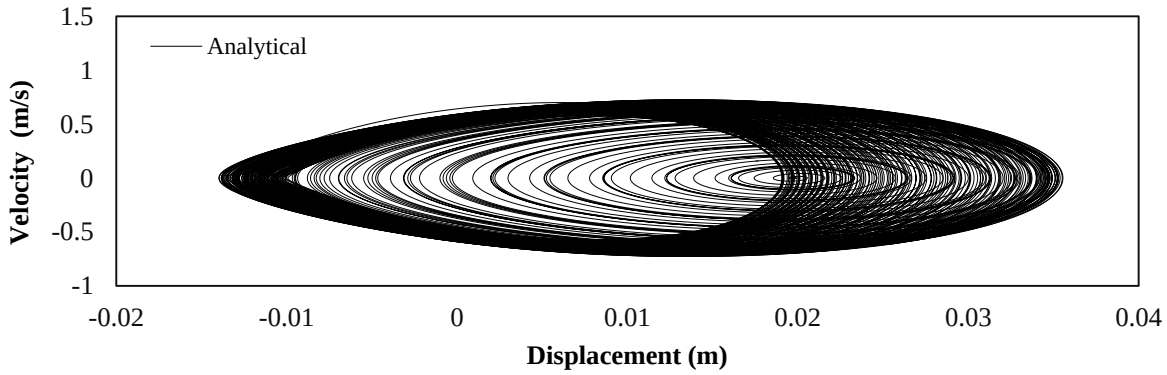

Figure 35: Phase plain of midspan deflection, load case A, simulation interval: 0 - 46 s.

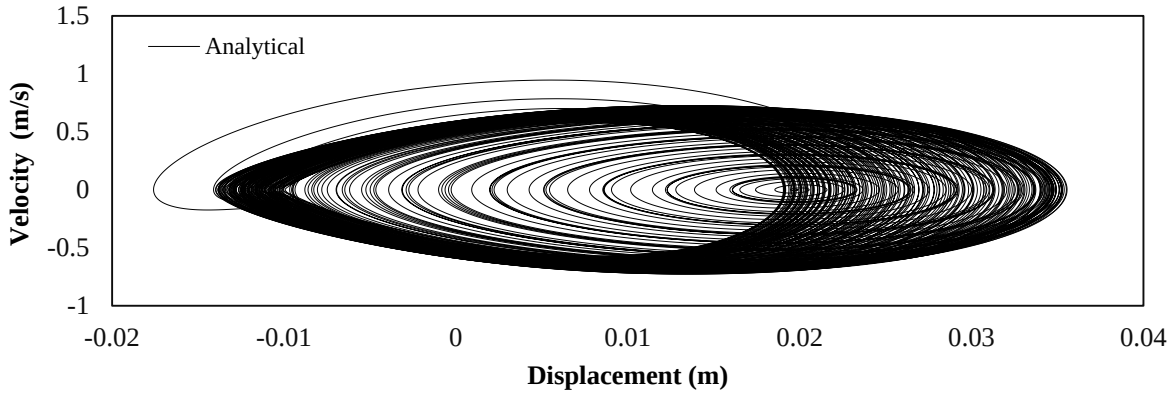

Figure 36: Phase plain of midspan deflection, load case A, simulation interval: 0 - 48 s.

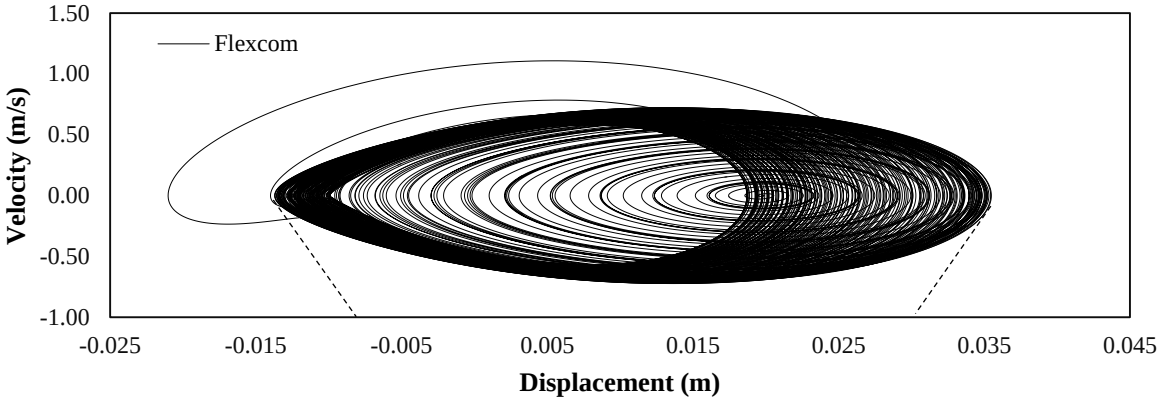

Figure 37: Phase plain of midspan deflection, load case A, simulation interval: 0 - 48 s.

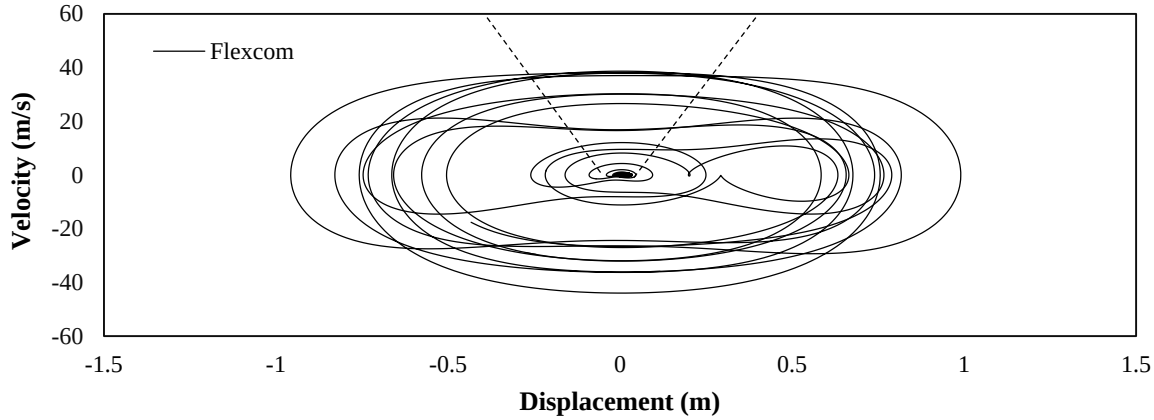

Figure 38: Phase plain of middle point for load case A, simulation interval: 0 - 50 s.

From figure 35, one can notice that the displacements are drawing elliptical trajectories around the dynamic equilibrium position (pole). The elliptical shape of the trajectories is due to the periodic oscillation. The pole of the oscillations is being shifted to the left, because of the imperfection and the envelope of the trajectories is incrementally amplified due to the increasing amplitude of the imposed axial motion. From figure 36, it can be seen that an escaping motion and consequently, instability occurred. From figure 37, it can be seen that Flexcom's phase plain plot is almost identical to the one obtained from the analytical model. After the finite jump of the displacement (jump), the system is again stable, oscillating around the post-critical dynamic equilibrium positions. Those are characterized by vastly amplified displacements and velocities as figure 38 illustrates. The trajectories of the motion are not elliptical anymore, representing the occurrence of aperiodic oscillations, characteristic of the snap through type of buckling (limit point buckling of imperfect structures).

This procedure will be applied in chapter 5, in order to identify, for regular wave excitation, the critical combinations of wave amplitudes and periods, that can initiate impulse dynamic buckling.

PART B

Base cases FE analyses: Generation of compression and stability assessment

Figure 39: HMC DV BALDER.

4

Dynamic compression

4.1. Introduction

The dynamic compression phenomenon is analyzed by conducting coupled nonlinear dynamic analysis using Flexcom software. Focus is given in the physics behind the development of the compressive forces and the relation with inertia and drag is demonstrated. A sensitivity study is performed to identify the driving parameters for the generation of compression in the sagbend area of the suspended pipe. The analysis is performed considering fully elastic material.

The motion of the installation vessel due to the incomes waves, excites the HOM, from where the pipe is suspended. The heave motion of the HOM induces a time varying effective axial load on the suspended pipe, named as dynamic tension. This can exceed the static effective tension that is applied from the installation vessel, generating compressive loading along a segment of the pipe. This particularly occurs in the sagbend area where the pipe exhibits lower effective tension due to the combined effect of weight and external hydrostatic pressure.

The analysis is performed by imposing a harmonic heave excitation on the HOM of the vessel. The effect of the heave amplitude and period is analyzed. The weight of the pipe, layback, tower angle and the offset of the vessel from its initial position, which is delimited by the pipelay watch-circle (see chapter 1.5), affect the effective tension along the suspended pipe. However, those parameters were optimized regarding other critical pipelay parameters, like the bending moment in the sagbend and overbend, hence it is of no particular interest to variate those with compression being a criterion. To that extent, only the variation of the vessels position will be examined, inside the allowable limits, as those have been defined by HMC pipelay design team in the original designs.

4.2. Static and dynamic tension

Because of the vessels vertical motion the effective tension variates in time. Its total value is given by the following formula.

$$T(x,t) = T_S(x) + T_D(x,t) \quad [4.1]$$

Where T is the total effective tension, T_S is the static effective tension and T_D is the time varying component due to the heaving motion of the HOM. The dynamic tension amplitude can surpass the static tension and compressive loading can arise in a segment of the pipe. This occurs particularly in the sagbend area, where the static component of tension has its lower value.

Typical plots, demonstrating the static tension variation along the length of the pipe are given below. The nominal vessel position is considered. The sagbend area and the TDP are highlighted with a dotted ellipse and a blue dot respectively. The starting point on the horizontal axis represents the theoretical anchorage point adopted by the FE model. The end point corresponds to the HOM.

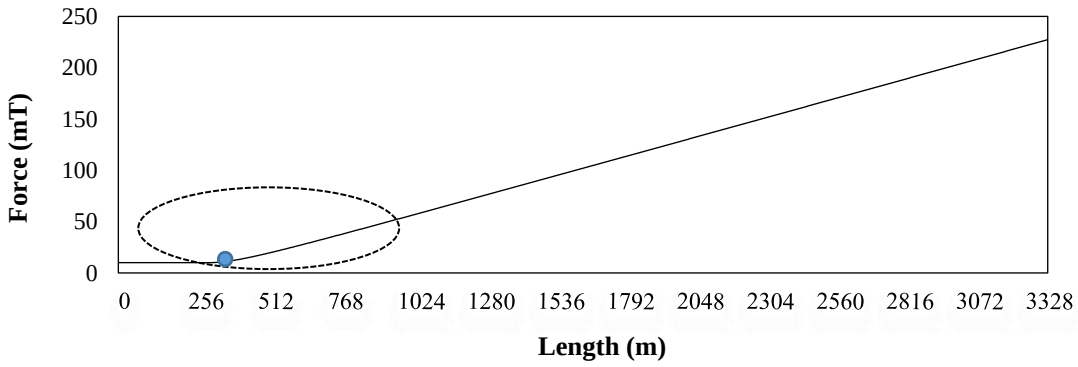

Figure 40: Static effective tension, nominal position, deep water case.

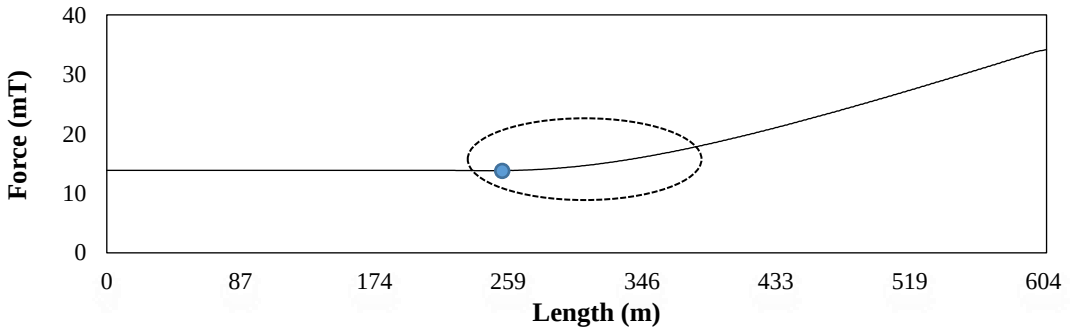

Figure 41: Static effective tension, nominal position, shallow water case.

What can be seen is that the static effective tension is significantly lower in the sagbend area of the pipe. This renders this position critical regarding the possibility of compression occurrence.

A typical plot demonstrating the variation of the total effective tension in the touchdown point of the deep water project due to harmonic heave excitation of the HOM is depicted below. Positive values demonstrate tensile loading while negative values illustrate compressive loading. The heave motion amplitude and heave period of the HOM are denoted as H and T respectively.

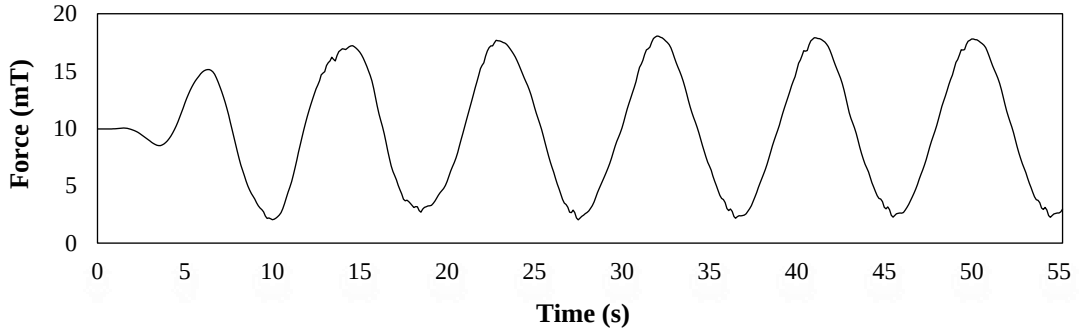

Figure 42: Total effective tension in the TDP , T=9s , H=1.5m, deep water case.

From figure 42 one can observe that the dynamic tension is introducing a sinusoidal variation of the total effective tension. The amplitudes are symmetric with respect to the value of the static effective tension. In that case, compression didn't emerge as the amplitude of the dynamic tension didn't exceeded the static component of the effective tension.

4.3. Sensitivity analyses

Static and dynamic analyses are performed based on the FE models that were used in the engineering phase of the projects. A harmonic motion of the HOM, replicating the action of a harmonic wave on a vessel with an RAO equal to unity is applied. This is done in order to gain a clear insight into the compression development, depending on two basic wave characteristics, namely wave amplitude and frequency, excluding the statistical uncertainties (various frequencies and wave heights) that a random wave excitation contains. The double amplitude of the harmonic HOM excitation is variated between 1 to 4 m. The HOM motion period varies from 6 to 12 s. The values were chosen to simply demonstrate the significance of heave period and amplitude and they do not replicate in any instance realistic HOM motions during pipelay.

The effect of the HOM heave motion amplitude and period on the generation of compression in the sagbend area is analyzed. The results are shown for the touchdown point. The vessels position is variated along the pipelay watch-circle. The effect of the far and near offset position (see chapter 1.5) on the static and dynamic tension is examined. The influence of an out of plane (sway) offset, representing the deviation of the vessel from the straight course is analyzed.

The basic geometric properties of the projects are given in the table below.

Table 8: Base cases characteristics.

Base case / Property	Deep	Shallow
Water depth (m)	2947	237
Suspended length (m)	3119	381
Vessel far/near offset (m)	75/75	8/12
Tower angle (degrees)	86	60
Outer steel pipe diameter (m)	0.2731	0.4510
Wall thickness (m)	0.0223	0.0219
Drag diameter (m)	0.4264	0.5824
Mass per unit length (kg/m)	221	364
Bending stiffness (N/m^2)	1.58×10^8	2.78×10^7

The drag diameter is different from the outer because of the existence of coating for both base cases. The coating contribution to the Flexular rigidity is not taken into account.

4.3.1. Heave amplitude and period

Considering the nominal vessel position (zero offset), the amplitude of the dynamic component of the total effective tension at the TDP is plotted against the heave double amplitude and period of the HOM. Tables containing detailed results can be found in Appendix part C.1.

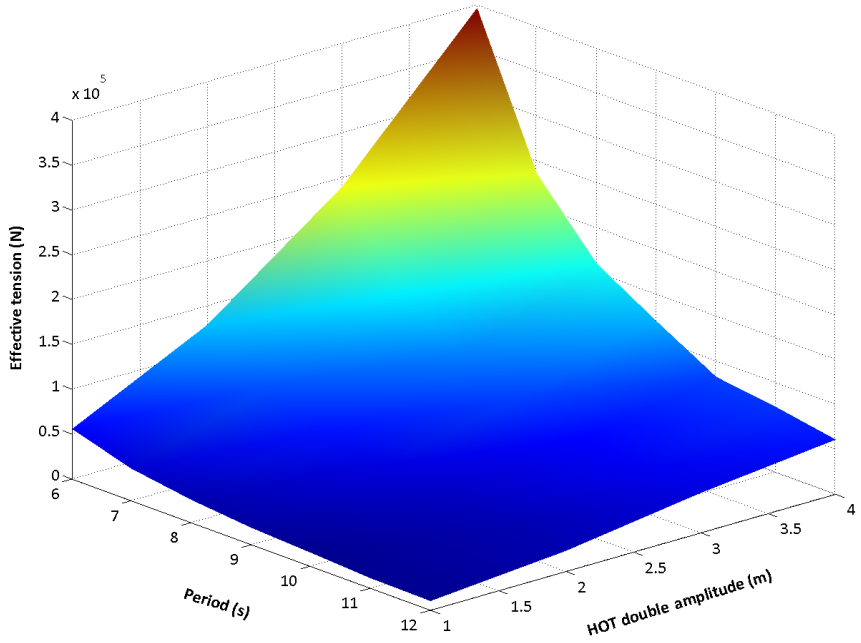

Figure 43: Dynamic tension amplitude in TDP vs HOM double amplitude vs period, deep water case.

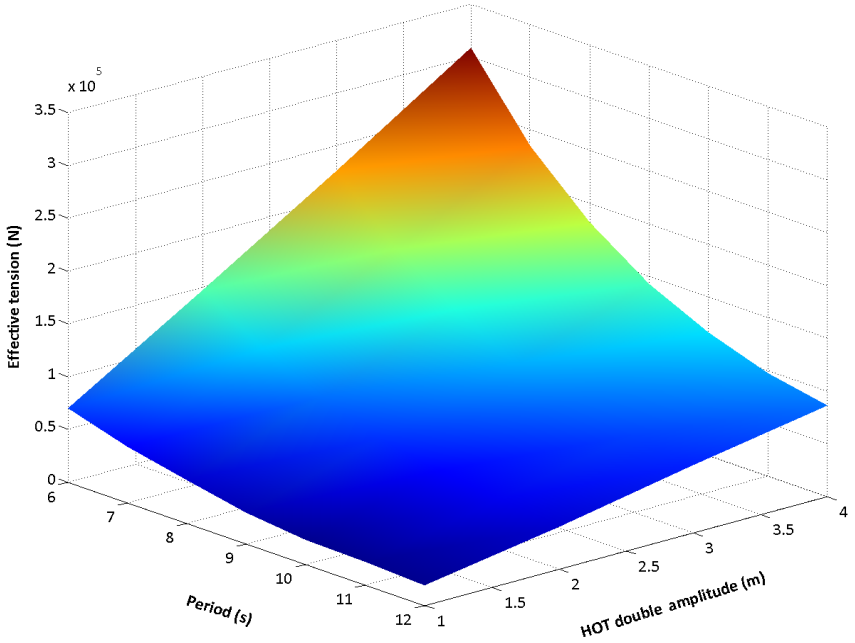

Figure 44: Dynamic tension amplitude in TDP vs HOM double amplitude vs period, shallow water case.

The amplification of the dynamic effective tension with increasing wave heights and decreasing periods relates the generation of the dynamic compression with the velocity of the heaving HOM. This is further investigated in chapter 4.6. The total effective tension in the TDP is plotted against the double amplitude and period of the harmonic HOM motion.

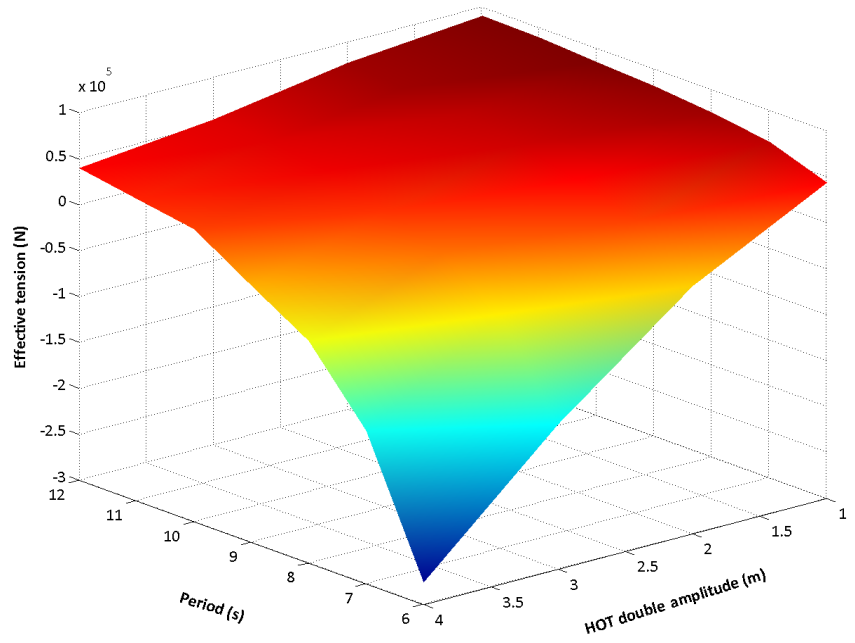

Figure 45: Total (minimum) effective tension in TDP vs HOM double amplitude vs period, deep water case.

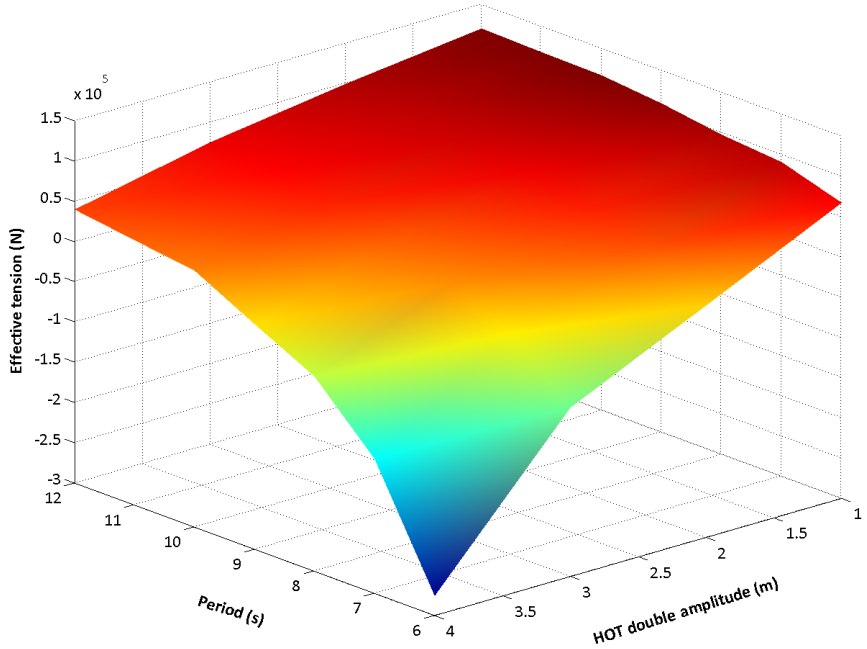

Figure 46: Total (minimum) effective tension in TDP vs HOM double amplitude vs period, shallow water case.

The total effective tension gets negative (compression) for increasing HOM heave amplitudes and decreasing periods. This is because the dynamic tension amplitude magnifies for increasing HOM heave velocities exceeding the applied static tension.

4.3.2. Vessel position

Static analyses. The static effective tension variation along the length of the suspended pipe is plotted for both projects for the near, far and zero offset positions.

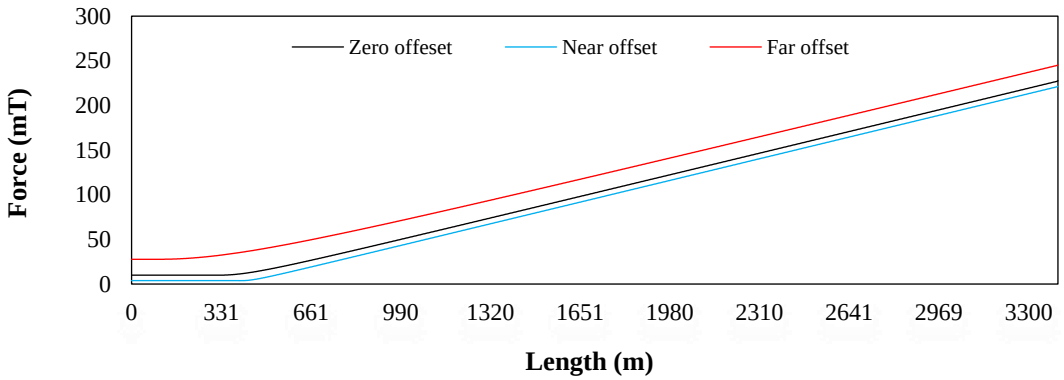

Figure 47: Static effective tension along the suspended length, deep water case.

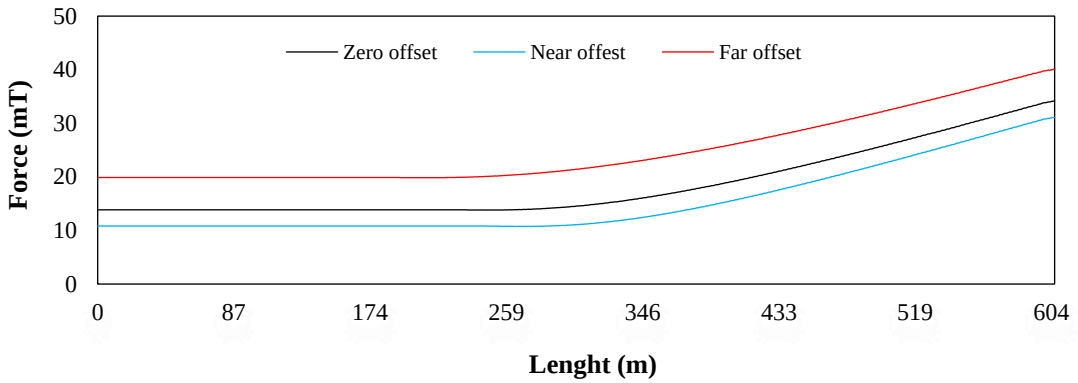

Figure 48: Static effective tension along the suspended length, shallow water case.

The effect of a near offset placement is a reduction in the static effective tension along the length of the pipe, comparing to the vessels zero offset (initial) position. The opposite occurs for the far offset. The variation of the static effective tension in the TDP is presented in the following table for the zero near and far offset positions.

Table 9: Variation of the static effective tension at the TDP due to longitudinal offset.

Project	**Shallow**	**Deep**
Offset	**Force (mT)**	**Force (mT)**
Zero	13.85	9.96
Near	10.83	3.82
Far	19.87	27.74

Dynamic analyses. The following plots, demonstrate the variation of the dynamic tension amplitude with the HOM heave period for a heave amplitude equal to 2m.

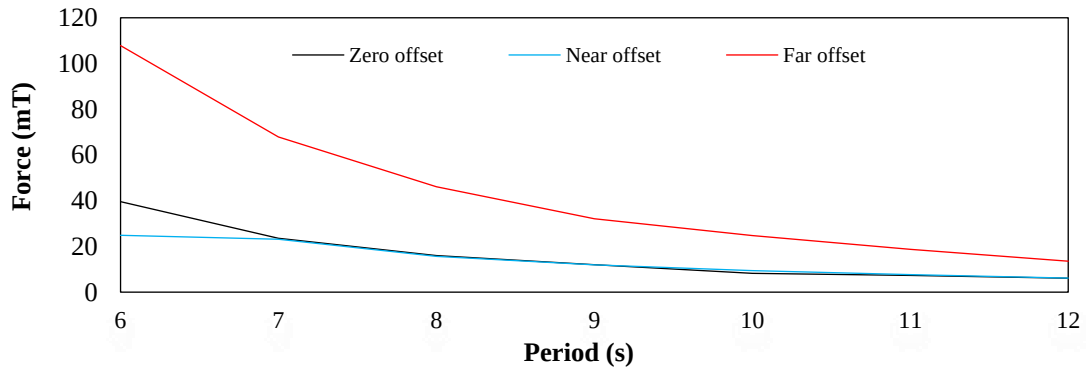

Figure 49: Dynamic tension amplitude at TDP for H=2 m vs HOM period, deep water case.

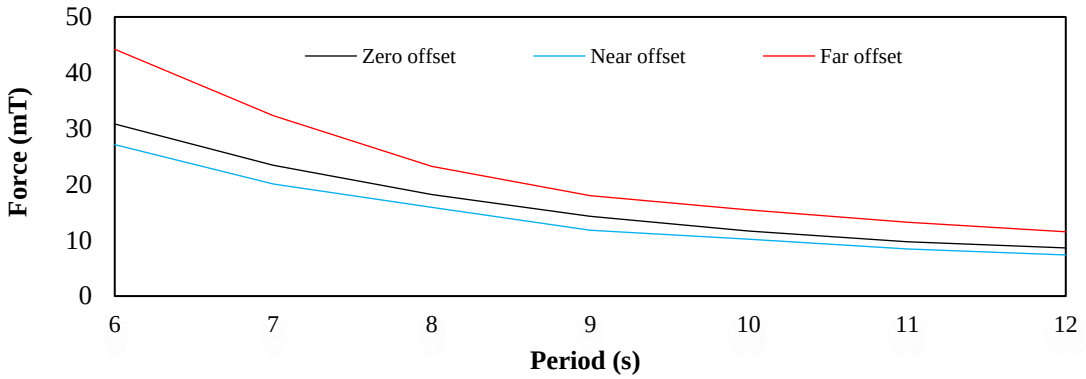

Figure 50: Dynamic tension amplitude at TDP for H=2 m vs HOM period, shallow water case.

What can be concluded figures 49, 50, is that the dynamic tension is following a different trend in statics than in dynamics. The near offset position, results in a reduction of the static effective tension while the dynamic amplitude of the axial force magnifies more for the far offset, rendering this position more critical for compression development, even if it is accompanied by higher static tension as it is shown in figures 47, 48. This has to do with the alternation of the inclination, as larger inclination angles caused by the far offset, are favouring the development of "hybrid" modes, favouring the amplification of the dynamic tension [24].

4.4. Relation with heave motion characteristics

As it was demonstrated previously (see chapter 4.3.1), there is a relation of the dynamic tension generation with the vertical velocity of the HOM. A velocity criterion regarding the dynamic compression generation, that was developed for offshore oil&gas riser applications, is applied. It is shown that the heave velocity of the HOM is not sufficient to identify if compressive loading will emerge. For this, the vertical acceleration of the HOM provides a more accurate criterion for the base cases that are examined.

4.4.1. Phase difference

The following plots demonstrate the phase difference between the displacement, velocity, and acceleration of the HOM with the total effective tension in the TDP of the base cases.

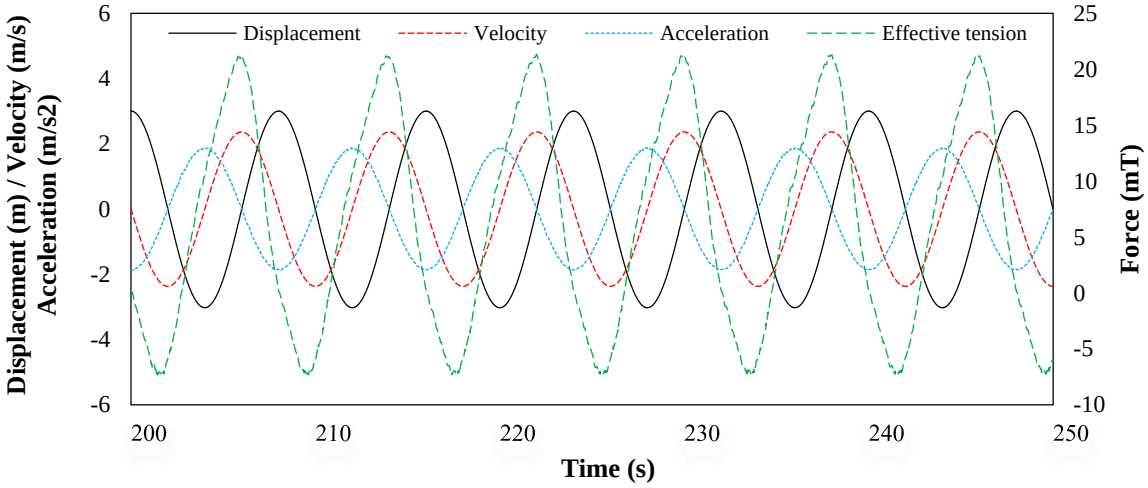

Figure 51: Phase difference, harmonic HOM heave motion, H=2m, T=8s, deep water case.

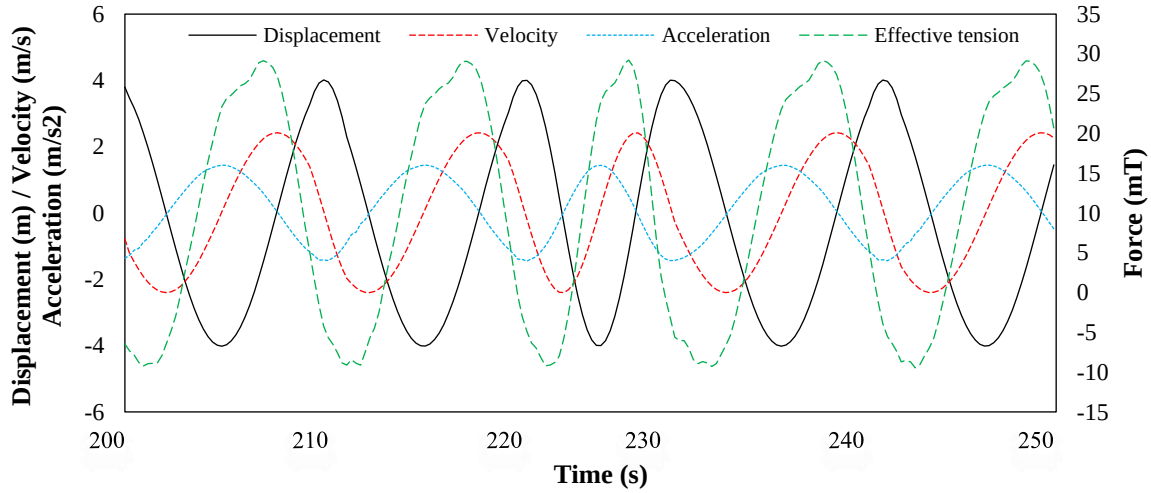

Figure 52: Phase difference, harmonic HOM heave motion, H=2m, T=8s, shallow water case.

What can be seen is that the total effective tension peak values correspond (approximately) to the HOM velocity and acceleration peaks. For that reason this relation is further investigated in the next section.

4.4.2. Velocity and acceleration effect

A publication relating the velocity of the heaving HOM with the generation of compressive loading in the TDP of offshore risers has been released [25]. The conclusion was that in the context of the deep water riser applications that were taken into account, compression is initiated from the inability of the pipe to travel through the water column with sufficient speed. This is triggered by the drag force, which acts against the direction of motion. As the velocity increases, the restoring drag force increases until it cancels out the acceleration and the suspended pipe reaches its terminal velocity. At the terminal velocity, the acceleration of the pipe is balanced by the restoring drag

force. It is not possible for the pipe to displace through the surrounding water faster than the terminal velocity. The hangoff velocity (velocity of HOM) can be directly compared with the terminal velocity of the suspended pipe.

$$Gravitational\ force = Drag\ force \rightarrow \ mg = \frac{C_d \rho D_{drag} V_{terminal}^{\ 2}}{2} \rightarrow$$

$$V_{terminal} = \sqrt{\frac{2mg}{C_d \rho D_{drag}}} \qquad [4.2]$$

A non-dimensional parameter consisting from the ratio of the hangoff velocity to the terminal velocity can be used as a criterion to indicate where compression may arise. Compression is expected where the parameter is 1.0 or greater. The bigger this term is, the greater the compressive force is expected to be. The terminal velocities for the base cases for $C_d = 0.8$ are shown in the table below.

Table 10: Base cases terminal velocities

Base case	Terminal velocity (m/s)
Shallow	3.87
Deep	3.52

The following tables demonstrate the application of the aforementioned criterion to the base cases.

Table 11: Terminal velocity criterion, shallow water case

HOM Double amplitude (m)	HOM Period (s)	HOM Velocity (m/s)	HOM Acc. (m/s^2)	$\frac{V_{HOT}}{V_{Terminal}}$ (m/s)	Minimum total effective tension in TDP (mT)
3	6	1.57	1.64	0.41	-11.3
3	7	1.34	1.20	0.35	-3.8
3	8	1.18	0.93	0.30	0.89
4	6	2.09	2.19	0.54	-21.70
4	7	1.80	1.62	0.46	-11.72
4	8	1.57	1.24	0.41	-4.09
4	9	1.40	0.98	0.36	-1.89
4	10	1.26	0.79	0.32	2.04

Table 12: Terminal velocity criterion, deep water case

HOM Double amplitude (m)	HOM Period (s)	HOM Velocity (m/s)	HOM Acc. (m/s^2)	$\frac{V_{HOT}}{V_{Terminal}}$ (m/s)	Minimum total effective tension in TDP (mT)
3	6	1.57	1.64	0.45	-14.23
3	7	1.34	1.20	0.38	-4.96
3	8	1.18	0.93	0.33	0.02
4	6	2.09	2.19	0.59	-27.57
4	7	1.80	1.62	0.51	-13.34
4	8	1.57	1.24	0.45	-5.83
4	9	1.40	0.98	0.40	-2.05
4	10	1.26	0.79	0.36	1.84

What one can observe from tables 11 and 12 is that the 3m - 6s and 4m - 8s amplitude - period combinations, are resulting in the same velocity of 1.57 m/s, but different values of total tension in the TDP. Different combinations of period and amplitude that give the same speed amplitude to the HOM, are creating different amplitudes of dynamic tension. In order to explain this difference the lateral and vertical accelerations are being plotted for the aforementioned excitations for both projects.

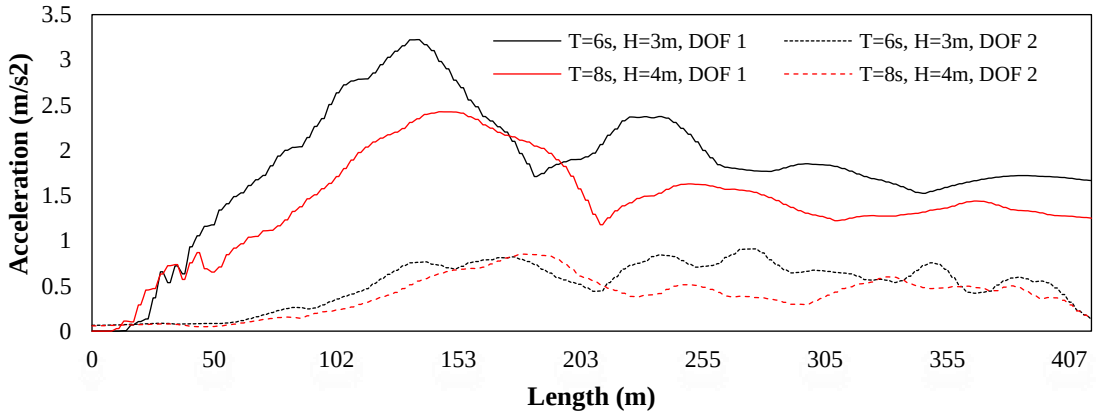

Figure 53: Acceleration along the length of the suspended pipe, harmonic HOM heave motion, shallow water case.

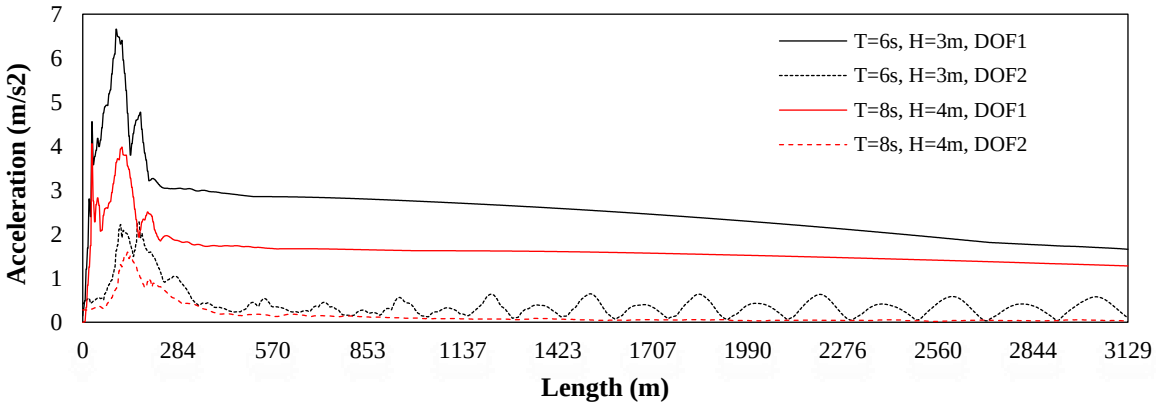

Figure 54: Acceleration along the length of the suspended pipe, harmonic HOM heave motion, deep water case.

From figures 53 and 54 one can observe that the lower period harmonic motion is accompanied with higher accelerations in the lateral and vertical directions. Hence bigger inertial forces are rising, which act in the opposite direction of the pipes deflection. Consequently, the motion of the pipe is being retarded in a bigger extent, leading to larger amplitudes of dynamic tension for the low period motion.

4.4.3. Heave absorption mechanisms

As it was demonstrated in the previous section, both velocity and acceleration of the heaving HOM are connected to the dynamic compression phenomenon. In the next section, the heave absorption mechanisms are analyzed and connected with velocity and acceleration of the HOM.

The response of the catenary shaped suspended pipe to an applied vertical displacement is associated with two "heave absorption mechanisms". The pipe moves in the lateral direction changing its shape (*catenary mechanism*) or it can move along its longitudinal axis giving rise in elastic forces due to the imposed shortening or elongation (*elastic mechanism*) [14].

During heave excitation, the pipe attempts to follow the applied vessel motion. As the pipe displaces through the water column, drag forces act against the direction of motion. The effect of the drag force is to retard the motion of the pipe. [20] [25]. Similar is the effect of inertia, as it acts against the direction of motion of the system. The combined effect of inertia and drag is "forcing" the pipe to absorb the motion partly elastically giving rise to large (comparing to the applied tensile load) axial forces.

The more the lateral and vertical motion of the pipe is restricted due to the drag and inertia forces, the more the resultant compressive loading in the sagbend rises, as the pipe is unable to alleviate the imposed motion with a change in its shape. A graphical representation, of the "in-plane and "out of plane" suspended pipe geometry, along with the adopted axis convection is given below.

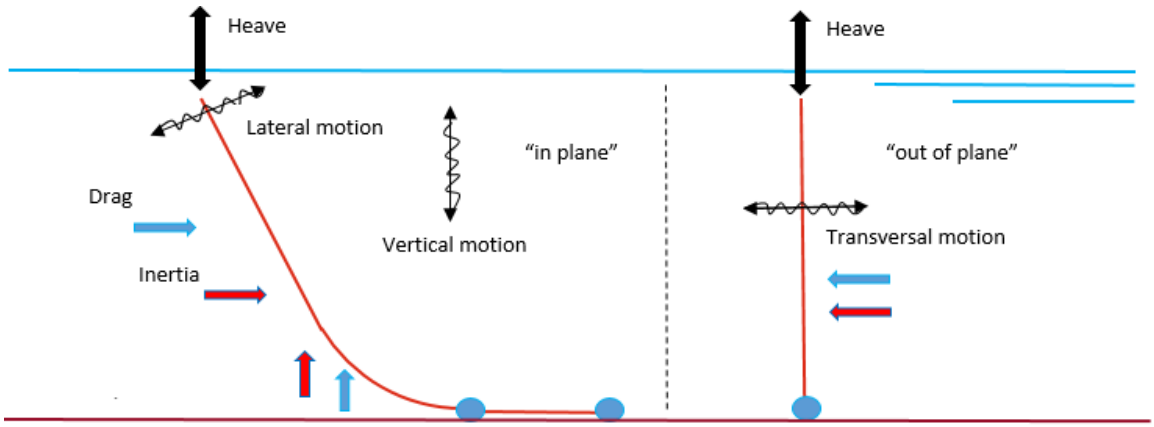

Figure 55: Heave absorption mechanisms.

5

Global stability assessment

5.1. Introduction

In the present chapter, the global stability assessment is performed. The critical combinations of heave amplitude and period that lead to the onset of impulse dynamic buckling, under harmonic excitation of the HOM are identified.

In accordance with chapter 3, a constant velocity loading is applied to demonstrate the effect of the heave velocity of the HOM on the critical buckling load. Then a dynamic buckling criterion and an applicable methodology for conducting the stability assessment against regular and irregular excitation, based on Flexcom's post processing results, is proposed. The critical impulse, for each period of excitation, is identified. This is used to assess the possibility of buckling against irregular dynamic excitation. Comparison with the original design where no compression is allowed is performed in order to quantify the potential gain in workability.

A sensitivity study on the effect of the vessel's position in the allowable HOM motions is conducted by performing FE analyses in Flexcom for various loading scenarios. The imperfection of the pipe is alternated for different vessel offsets, affecting the buckling capacity of the system. In the same time, this also affects the dynamic tension generation as it was shown in chapter 4.3.2. The position where the lowest heave motions are allowed is identified (critical "buckling" position). Finally, the effect of the seabed coefficient of friction is examined.

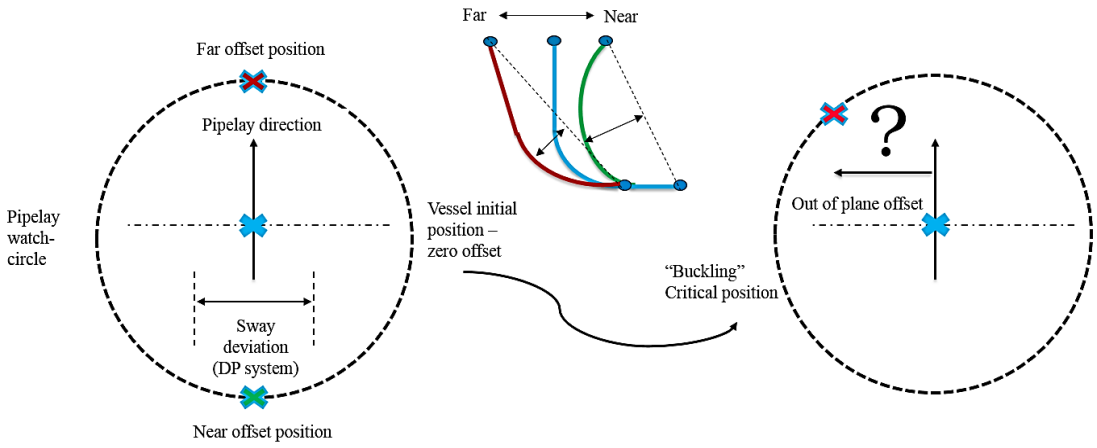

Figure 56: Critical "buckling" position.

5.2. Constant velocity loading

Applying a sinusoidal motion loading on the HOM of the suspended pipe results in a sinusoidal velocity loading and the relation between the heaving HOM velocity and critical buckling load cannot be explicitly defined. A constant velocity loading is applied to the HOM of the base cases. This is done to demonstrate the increased load-bearing capacity of the system with increasing loading velocities.

In order to initiate a realistic three-dimensional motion on the suspended pipe, a small out of plane force equal to 1000 N, is applied to the top node of the suspended pipe. The HOM is moved towards the seabed until buckling occurs according to the Budiansky and Roth dynamic buckling criterion (see chapter 2.7.1). The negative effective tension measured at that moment in time is denoted as the critical buckling load (P_{cr}).

5.2.1. Load cases

The range of velocities taken into account is 1×10^{-4} to 0.5 m/s. Higher HOM velocities are induced from wave excitations that cannot occur during pipe-laying operations. This is because various technical procedures like pipe welding, cannot take place when the vessel exhibits severe motions due to the wave excitation.

A sensitivity study is performed by considering various loading scenarios. The vessel position is variated between the near and far offset positions and an out of plane (sway) offset is introduced. This is done in order to demonstrate the dependency of the critical buckling load to the imperfection (out of straightness) of the suspended pipe. The in plane imperfection of the pipe is growing moving from the far to the near offset position (see figure 56). An out of plane (sway) offset is introduced to study the effect of biaxial imperfection.

The following load cases will be taken into account.

Table 13: Load cases, constant velocity loading.

Parameter / Case	Longitudinal offset (Near / Zero / Far)	Sway offset (m)
A	Near	0
B	Zero	0
C	Far	0
D	Far	0.5

5.2.2. Results

Initially, Hoff's dynamic similarity number Ω (see chapter 2.4) is calculated for each constant velocity. Generally, when $\Omega \to \infty$, the quasi-static capacity is being measured and when $\Omega \to 0$, the loading can be considered rapid meaning that inertia contributes to the buckling capacity of the system. This nondimensional number can be used in order to compare the contribution of inertia to the buckling capacity of systems with different physical characteristics.

Table 14: Dynamic similarity number for the base cases.

Project	Shallow	Deep
Velocity (m/s)	Ω	Ω
0.0001	9.68×10^{-2}	1.31×10^{-8}
0.001	9.68×10^{-4}	1.31×10^{-10}
0.05	3.87×10^{-7}	5.23×10^{-14}
0.1	9.68×10^{-8}	1.31×10^{-14}
0.2	2.42×10^{-8}	3.27×10^{-15}
0.3	1.08×10^{-8}	1.45×10^{-15}
0.4	6.05×10^{-9}	8.17×10^{-16}
0.5	3.87×10^{-9}	5.23×10^{-16}

The following table demonstrates the variation of the critical buckling load (P_{cr}) and DLF with the velocity applied on the HOM for both projects for load case A. Analytical results for all load cases can be found in Appendix part C.2.

Table 15: Constant velocity loading results, load case A.

Project	Shallow		Deep	
Velocity (m/s)	**P_{cr} (mT)**	**DLF**	**P_{cr} (mT)**	**DLF**
0.0001	2.35	1	0.64	1
0.001	2.35	1	0.64	1
0.05	2.7	1.17	0.8	1.25
0.1	10.99	4.28	10.07	17.17
0.2	34.75	14.78	31.36	49.01
0.3	54.91	23.37	51.73	80.82
0.4	75.39	32.08	72.10	112.66
0.5	95.48	40.63	92.48	144.50

From table 15, one can observe that for both projects, a velocity lower than 0.05 m/s, yields the static buckling capacity of the system and consequently, a DLF number equal to unity. Higher velocities are yielding higher critical buckling loads in accordance with what was discussed in chapter 3. In that case, the pipe is surrounded by water and both inertia and drag force contribute to the buckling capacity of the pipe. In the following graphs, the variation of the critical buckling load with the applied velocity for each load case is presented.

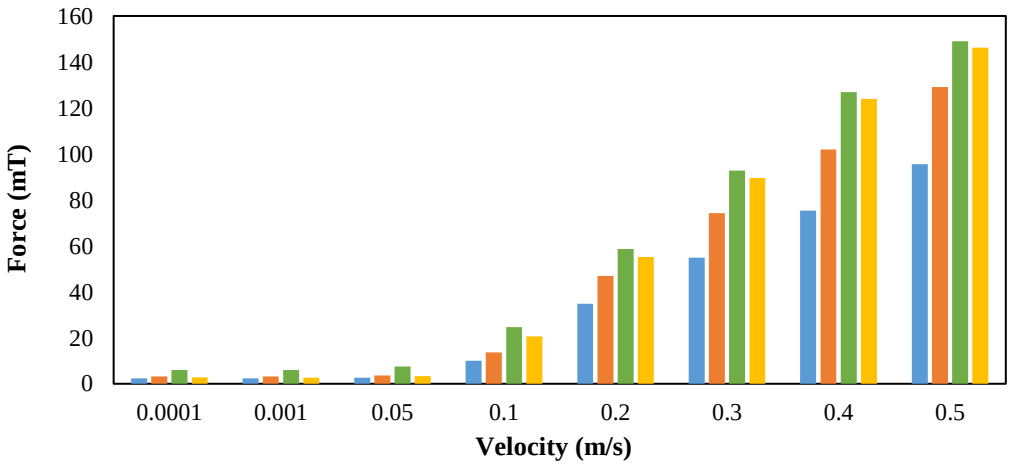

Figure 57: Critical buckling load vs HOM velocity, shallow water case.

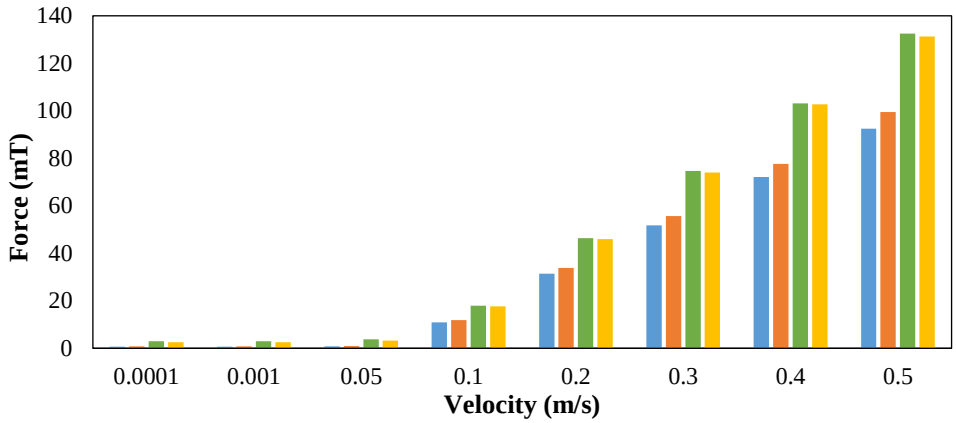

Figure 58: Critical buckling load vs HOM velocity, deep water case.

The in plane imperfection of the pipe increases when moving from the far offset position to the near Observing figures 57 and 58 the critical buckling load decreases with increasing imperfection. Accordingly, the introduction of an out of plane imperfection further reduces the buckling capacity of the system.

5.3. Harmonic and irregular excitation

5.3.1. Dynamic buckling criterion

In order to identify the critical heave motion of the HOM for the onset of impulse dynamic buckling against harmonic displacement loading, the same procedure with chapter 3.4.4. is applied. A sinusoidal vertical motion of the HOM with a linearly increasing amplitude is applied in order to "force" the system to buckle. The following plots demonstrate qualitatively, the in and out of plane deflection of the pipe, for the shallow water case.

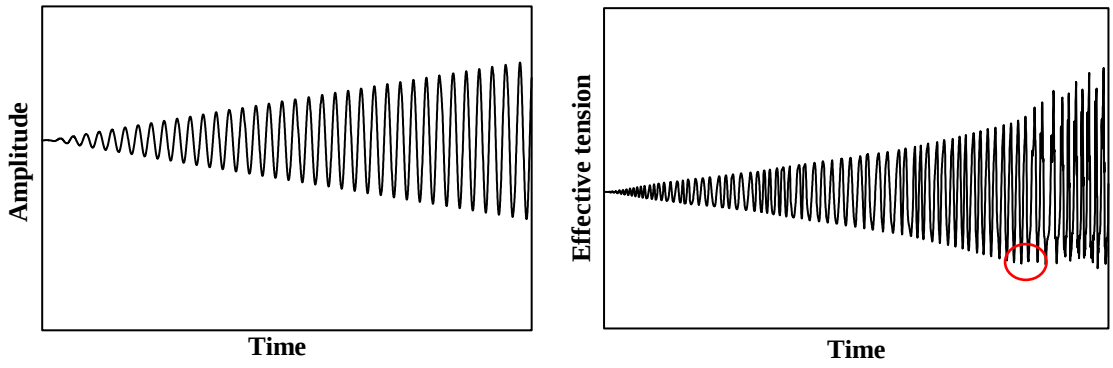

Figure 59: Linearly increasing HOM heave amplitude (left), total effective tension in TDP (right).

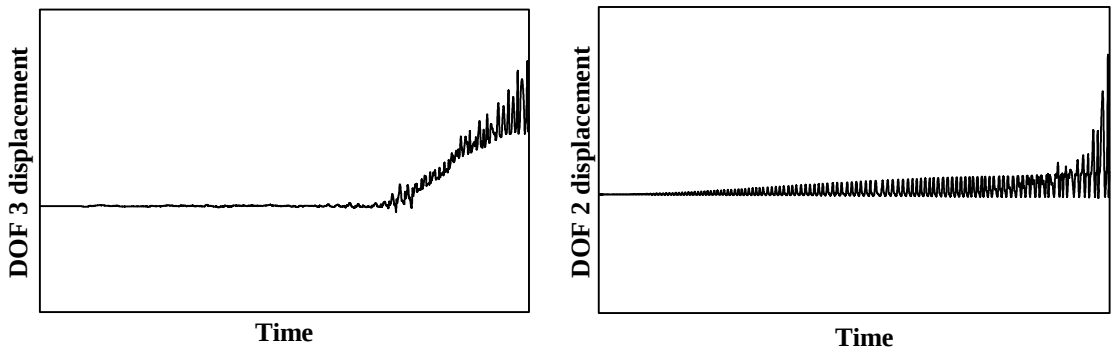

Figure 60: Out of plane displacement (left), in plane displacement (right).

Observing figure 60, the resulting in and out of "displacement jump", is not straightforward, so the Budiansky & Roth criterion cannot be accurately applied. This can be modified as follows in order to accurately perform the global stability assessment for the base cases: *Buckling is assumed to occur when for a small increase in the displacement amplitude, a reduction in the resultant axial load of the system occurs.* The reduction in the negative effective tension in the TDP, for a slightly increased HOM heave amplitude, is an indication of buckling, as it reflects alleviation of stress through extensive displacement. As it was shown in chapter 3.4.4., plotting the displacement phase-plains, this moment in time corresponds to the development of an escaping motion which is an indication of instability onset.

Based on this dynamic buckling criterion, a methodology for conducting the stability assessment for the base cases against regular and irregular excitation, using Flexcom's post processing results, is proposed.

5.3.2. Methodology

The proposed methodology for the global stability assessment against regular and irregular excitation is given in steps below. For every heave period of the HOM taken into account for the pipelay analyses:

1. Ramp linearly the heave amplitude of the HOM (H), throughout the whole simulation time, until it reaches a sufficiently high value, in order to "force" the pipe to buckle. The longer the simulation time, the smoother the ramping is and more combinations of period and amplitude are taken into account, leading to more accurate results.

2. Plot the HOM heave motion and the resultant effective tension time-traces in the TDP.

3. Denote the moment in time where a decrease in the resultant negative effective tension time-trace occurs. The amplitude of the preceding pulse load is the critical buckling load (effective tension) amplitude (P_{cr}) and the corresponding impulse is the critical impulse of the system (J_{cr}) for the period of the applied excitation.

4. Taking into account the phase difference between the displacement of the HOM and the effective tension generation (see chapter 4.4.1.), the critical HOM amplitude (H_{cr}) is identified. Then the critical velocity (v_{cr}) and acceleration (a_{cr}) amplitudes of the HOM can be calculated.

5. For increased accuracy, re-run the procedure from step 1, by ramping the HOM amplitude up to 1.1 times the calculated critical heave motion of the HOM (1.1 x H_{cr}).

6. *Regular excitation:* Compare the heave motion of the HOM with H_{cr} .

7. *Irregular excitation:* Compare the resultant effective tension impulse in the TDP with J_{cr} .

In order to identify if any convergence error is carried over the simulation time because of the linear displacement amplitude increase, individual runs with constant amplitude where performed. It was found that by setting a time step between 0.01s and 0.001s and a total simulation time of 1000s, there is no need of running individual analyses. However this can be applied as a validity check, for increased confidence over the results. The proposed methodology is being schematically presented below.

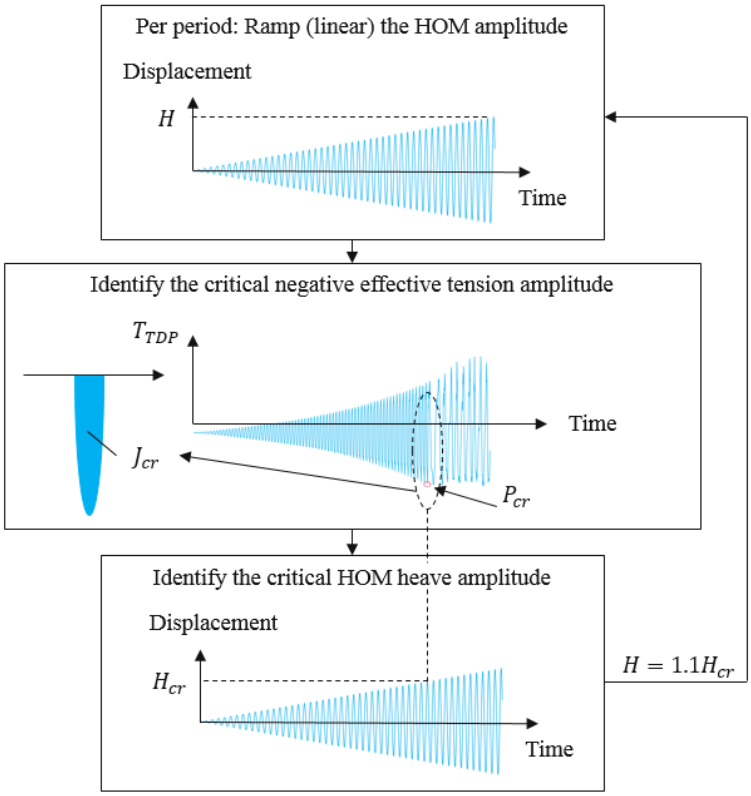

Figure 61: Schematic representation of the proposed methodology for the identification of impulse dynamic buckling onset.

5.3.3. Regular excitation: load cases & results

The global buckling assessment according to the proposed methodology, is performed for both the far and near offset positions, combined with an out of plane (sway) offset, replicating the deviation of the DP system from the straight course. A far offset position amplifies the dynamic tension generation (see chapter 4.3.2.), while it increases the buckling capacity of the pipe because a reduction of the in plane imperfection occurs. For the near offset, the opposite is true, so it not straightforward which vessel position will lead to lower allowable heave motions of the HOM.

The effect of the coefficient of friction between the pipe and the seabed is analyzed by alternating its value between the upper and lower bounds that are usually encountered for soils in the marine environment.

The following load cases are analyzed.

Table 16: Load cases for the identification of impulse dynamic buckling onset.

Parameter / Case	Longitudinal offset (Near / Far)	Sway offset (m)	Seabed coefficient of friction
A	Near	0	0.6
B	Near	0	0.1
C	Far	0	0.1
D	Far	2	0.1

In the following plots, the critical heave motion of the HOM and the critical impulse per period of excitation are plotted for each load case for the range of periods of 8 to 12s. Tables containing more results (critical HOM velocities, accelerations, impulses etc.) can be found in Appendix part C.3.

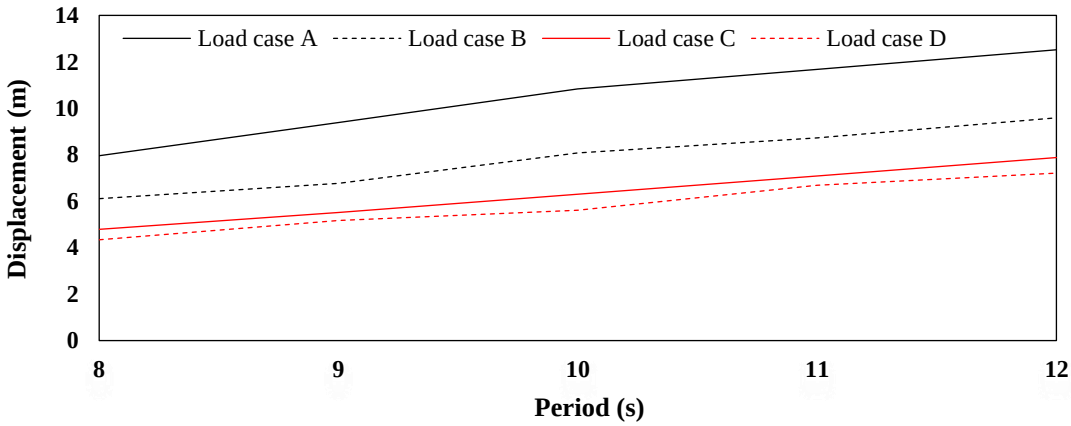

Figure 62: Critical heave amplitude of the HOM vs HOM period, shallow water case.

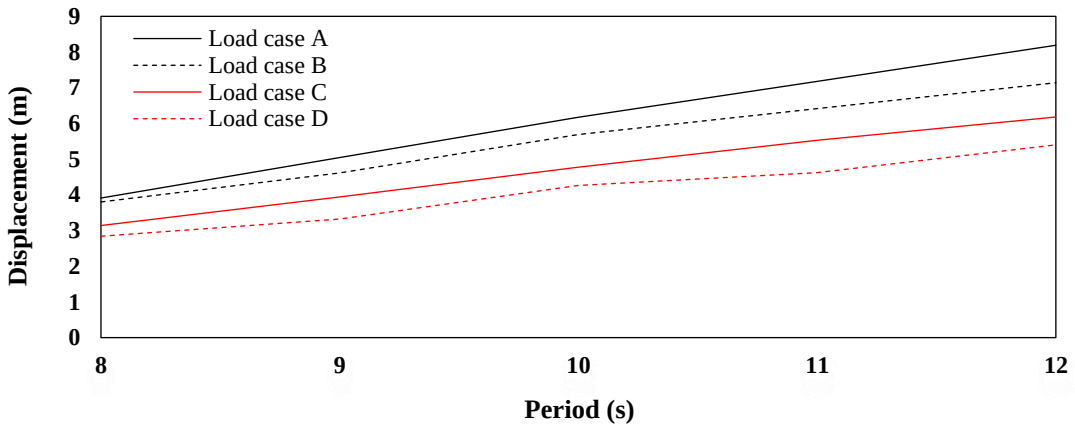

Figure 63: Critical heave amplitude of the HOM vs HOM period, deep water case.

Observing figures 62, 63 one can deduct that a lower coefficient of friction is reducing the buckling capacity of the system. This is because it governs the out of plane vibration of the system. Lowering the coefficient of friction, less energy is needed for the pipe to deflect in the out of plane direction so buckling can be initiated by lower HOM heave motions.

The longitudinal vessel position significantly affects the allowable heave motion of the HOM. Moving from the near to the far offset position, one can observe that lower HOM heave motions are needed to destabilize the system. This is because the dynamic tension amplitude amplifies significantly in the far offset position. Hence, lower heave motions are needed to reach the critical buckling load comparing to the near offset position. This could seem contradicting considering that the in plane imperfection of the system follows the opposite trend as it grows moving from the far to the near offset position. Comparing the critical impulse of the near and far offset positions, (see Appendix part C.3, tables 25, 26) one can notice that the difference is negligible, so the dynamic tension generation is the driving parameter that reduces the allowable HOM heave moving from the near to the far offset position.

The introduction of an out of plane offset is reducing the buckling capacity due to the introduction of biaxial imperfection, while it does not significantly affect the dynamic tension generation. Hence lower HOM heave motions are needed to destabilize the system in that case.

In order to visualize the change in the response caused by the onset of dynamic impulse buckling, the HOM is dynamically excited by a regular sinusoidal heave motion. The analyses is performed for two different heave amplitudes, for the same period. For a period equal to 8s and for the far offset case of the deep water project (load case C), a slightly lower (2.9m) and a higher (3.4m) HOM heave amplitude than the critical for the onset of impulse buckling (3.15 m) are applied. The simulation time is set to 20 minutes with a ramp time of twelve periods. The response is being plotted for a point in the sagbend close to the touchdown point. In the following figures, the out of plane displacement and bending strain phase-plains are illustrated. Plots for the in and out of plane deflections of the system along with the in plane phase planes can be found in Appendix part C.3.

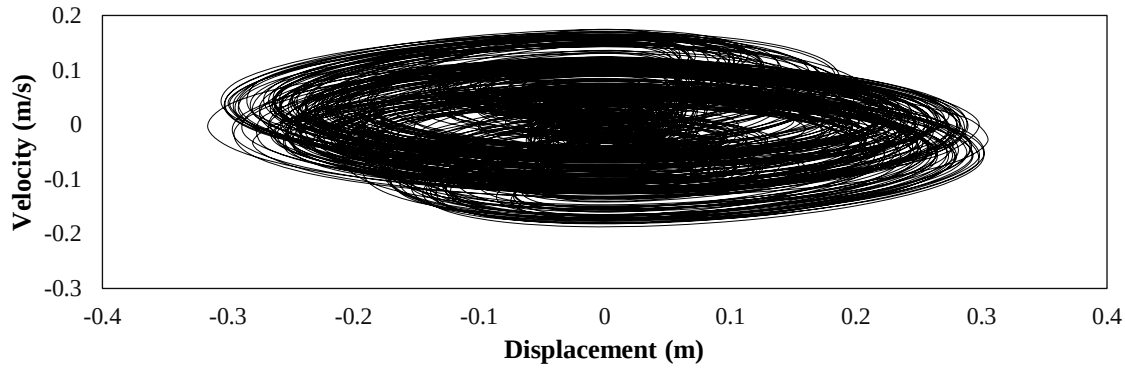

Figure 64: Out of plane motion (DOF3) phase plain, H=2.9m, T=8s, deep water case.

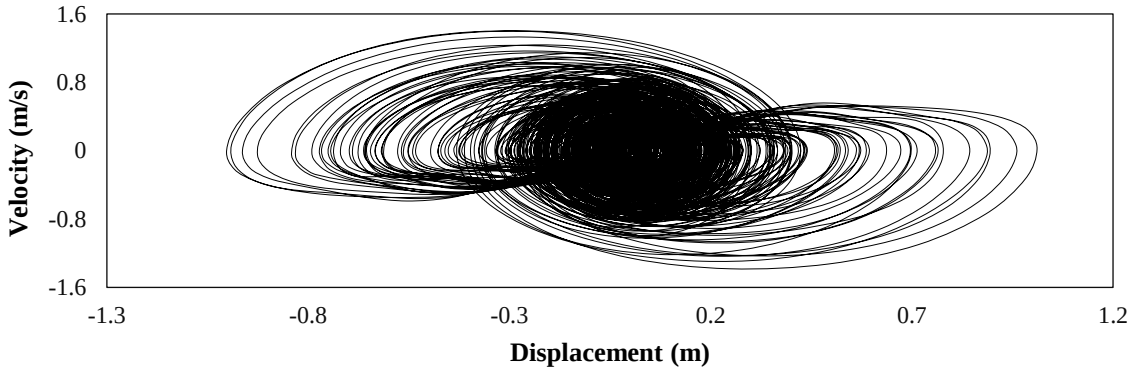

Figure 65: Out of plane motion (DOF3) phase plain, H=3.4m, T=8s, deep water case.

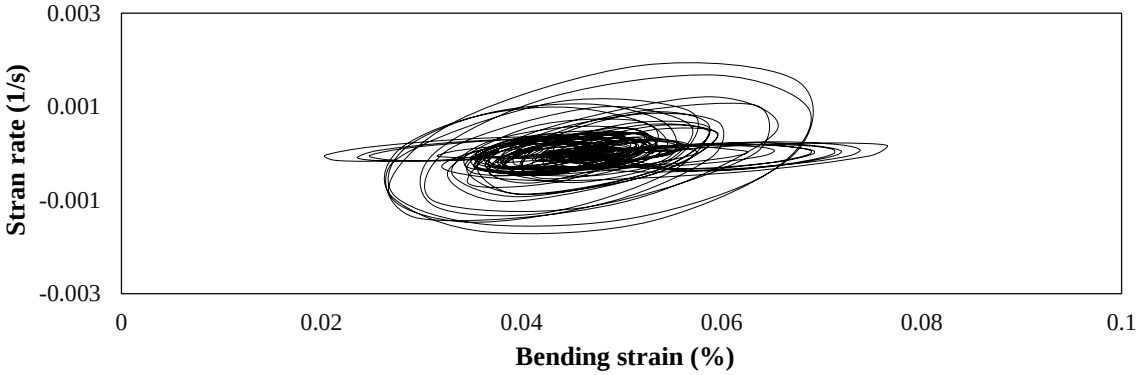

Figure 66: Out of plane motion (DOF3) phase plain, H=2.9m, T=8s, deep water case.

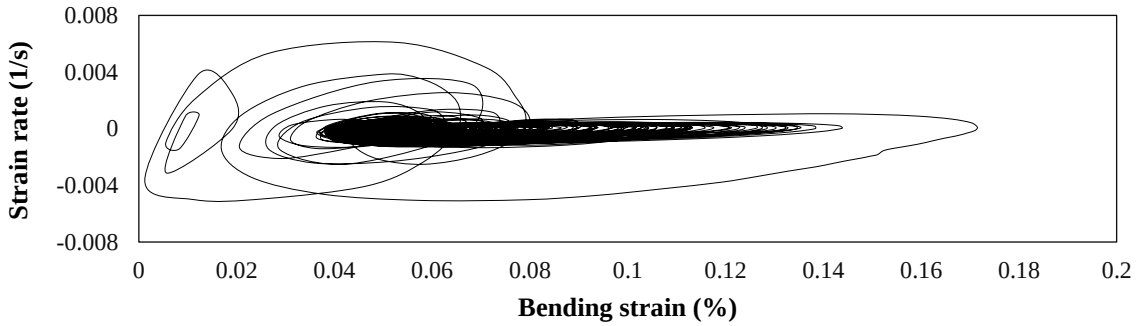

Figure 67: Out of plane motion (DOF3) phase plain, H=3.4m, T=8s, deep water case.

From figures 64 and 65 one can visualize the out of plane motion amplification due to the onset of impulse dynamic buckling. The escaping motions initiated by the destabilization of the system are visible in figure 65. The motion is bounded because the system is stabilized by the geometrical non-linearity and drag.

Observing figure 66, small escaping motions of the bending strain can be observed. This is due to parametric resonance as the suspended pipe is loaded with a heave period close to a natural period of the system. Parametric resonance cannot induce dangerously big strains in the suspended pipe as it is quickly damped by drag [2]. The effect of the impulse dynamic onset on the bending strain of the system can be seen in figure 67, where severe escaping motions occur, leading to big amplification of the stress in the system.

5.3.4. Irregular excitation: load cases & results

A random wave analysis is imperative for a robust design because of the uncertainty of varying heave amplitudes and periods during realistic wave conditions. The resultant negative effective tension time-trace can be decomposed into discrete impulses and evaluated using the design methodology against the regular harmonic excitation.

An application of the proposed methodology is given for the base cases. An irregular heave excitation is applied on the HOM. The heave amplitudes considered are unrealistic for a pipelay operation. They are specifically selected in order to possibly initiate impulse dynamic buckling, which was shown to require excessive HOM heave motion to occur (see chapter 5.3.3.). The analyses is performed considering the vessels far offset position along with an out plane (sway) offset of 2m.

An identical irregular heave motion timetrace is applied on the HOM of both projects. For each base case, three load cases are applied, varying only the amplitudes of the applied excitation. The period of the heave motion variates from 10.8 to 11.2 s. This replicates the variation of the period of the HOM due to an irregular wave excitation with a significant period of 11s. This is a realistic approximation as the heaving vessels period is not usually fluctuating in a big extent. The maximum heave amplitude of each load case along with the maximum resultant negative effective tension

impulse are given in the table below. The integration is performed by utilizing the trapezoidal numeric integration function in MATLAB, inserting the negative effective tension pulse time-trace form the FE analyses post-processing results.

Table 17: Irregular HOM excitation load cases.

Project	Shallow		Deep	
Load case	H_{max} (m)	J_{max} (s)	H_{max} (m)	J_{max} (s)
A	5.15	113	10.36	430
B	4.25	77	7.89	406
C	4.03	59	6.07	266

A representative plot of the applied excitation is given below for the deep water project.

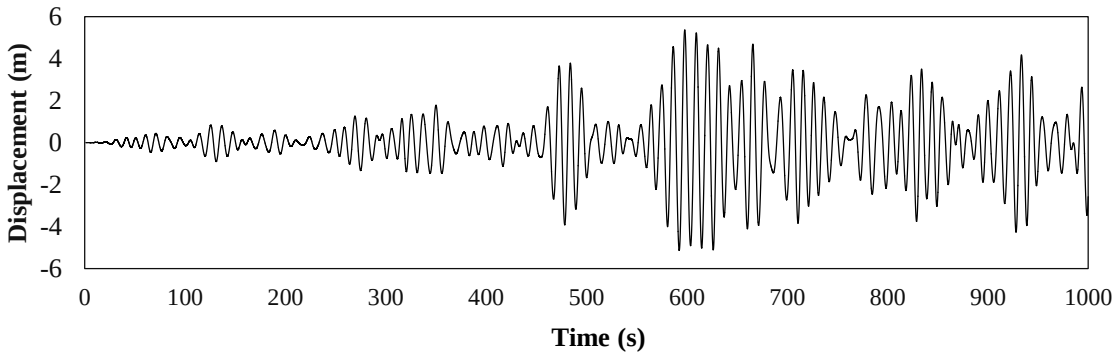

Figure 68: HOM heave motion, H_{max}=5.15m, deep water case.

Applying the methodology for design against regular wave excitation, for the far offset position along with an out plane (sway) offset of 2m, (load case D), results in the following critical impulses (see Appendix part C tables C.3.).

Table 18: Critical impulse for far offset position plus 2m sway.

Project	Deep	Shallow
Heave Period (s)	J_{cr} (mTs)	J_{cr} (mTs)
10	80	209
11	87	276
12	102	295

The HOM period do not vary significantly. It fluctuates between 10.8 to 11.2 s. Thus the critical HOM heave motion or impulse derived from the regular wave stability assessment with a period of 10 s can be used to conduct a conservative assessment. A more accurate design can be performed by applying the methodology for regular excitation for the range of periods 10,8 to 11,2 s. Then the

effect of each individual impulse can be assessed by comparison with the critical for the same loading period.

Observing tables 17 and 18, the largest negative effective tension impulse of load case A, exceeds the critical impulses of the 10s ,11s and 12s (periods) of the deep water case and initiation of instability accompanied by an amplification of displacement in the out of plane direction is expected. The same occur for the shallow water case for load cases A and B.

In order to visualize the impulse dynamic buckling onset due to the applied load cases, the out of plane motion of a point in the sagbend is plotted.

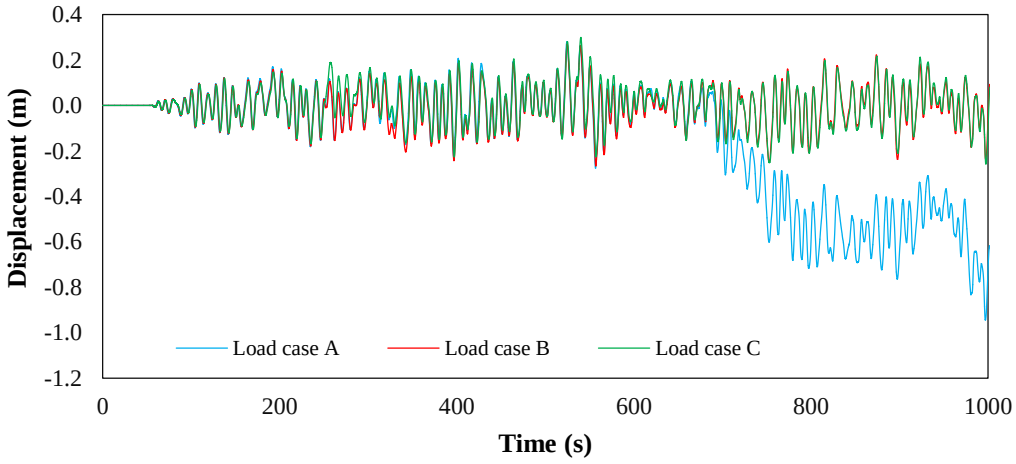

Figure 69: Out of plane displacement (DOF3) of a point in the sagbend, deep water case.

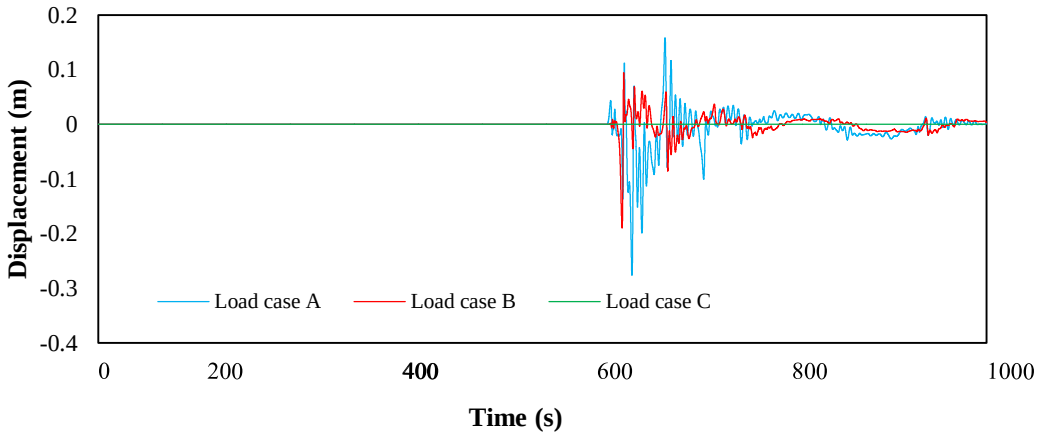

Figure 70: Out of plane displacement (DOF3) of a point in the sagbend, shallow water case.

5.4. Allowable regular harmonic HOM motions

According to DNV, compression may be allowable provided that it doesn't lead to other failure modes like local buckling or excessive fatigue loading. Fatigue is not in the scope of the present research and it will not be taken into account.

In order to define the allowable HOM motions, DNV load controlled local buckling check should be performed. This describes buckling within the pipes cross-section under the combined effect of bending moment effective tension and external hydrostatic pressure. For conducting DNV-LCC two main quantities are needed, the bending moment and effective tension time-traces for the points along the suspended pipe length. The result is a dimensionless value which is compared with unity. Higher values than unity are not allowed.

The maximum allowable heave motion per period will be specified by either the onset of impulse dynamic buckling, which defines the *global structural integrity (global buckling assessment)*, or by DNV LCC which delineates the *local structural integrity (local buckling assessment).*

Hereby, the critical HOM motions for the onset of impulse dynamic buckling derived from the stability assessment conducted in chapter 5.3.3. will be compared to the allowable HOM motions as those derived in the engineering phase of the projects. Heave motions leading to compressive loading were excluded from the original design. The allowable heave motions of the HOM in the original design, where delimited by either the DNV – LCC check or by the presence of compression.

For the comparison a limit state design approach is adopted as the values from the most onerous load case, regarding the impulse dynamic buckling onset will be taken into account. This was found to be the far offset vessel position combined with an out of pane offset of 2 m and a coefficient of friction equal to 0.1.

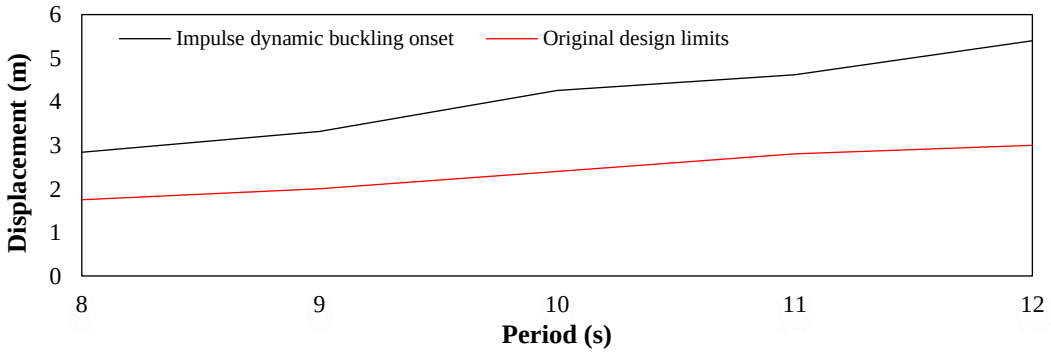

Figure 71: Allowable HOM heave motions vs period, deep water case.

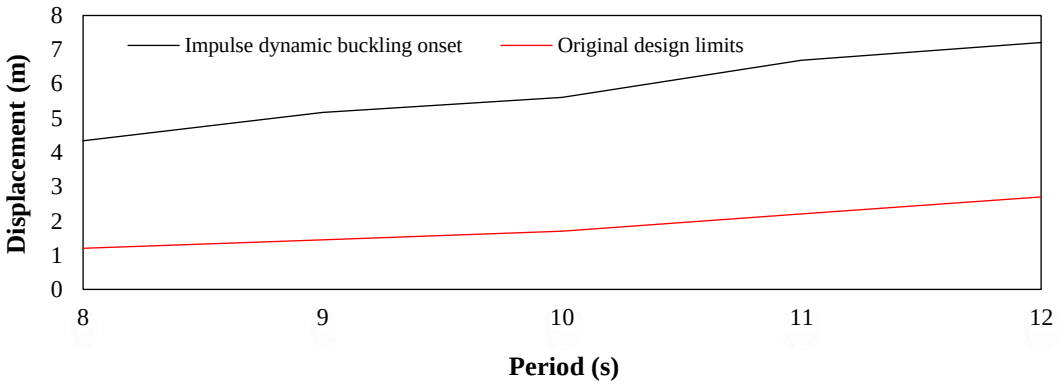

Figure 72: Allowable HOM heave motions vs period, shallow water case.

What one can observe from figures 71, 72 is that considerably larger HOM heave motions are needed to initiate impulse dynamic buckling than local buckling according to DNV – LCC for both projects. This renders compression non-critical for both base cases. In order to quantify the potential gain in workability by allowing compression, DNV – LCC unity check is performed for both projects.

DNV – LCC result should be lower or equal to unity. The check is performed for the point with the maximum static bending strain along the pipe, considering the vessels near offset position. This is located close to the touchdown point for both projects. Conducting the check for one point is a simplification because, for different sea-states and vessel offsets, the position with the biggest curvature and in accordance bending strain varies. However, this can be a quite accurate approximation. In the following plots, the DNV – LCC results are presented for the limiting combinations of HOM heave amplitudes and periods, as those defined in the original designs.

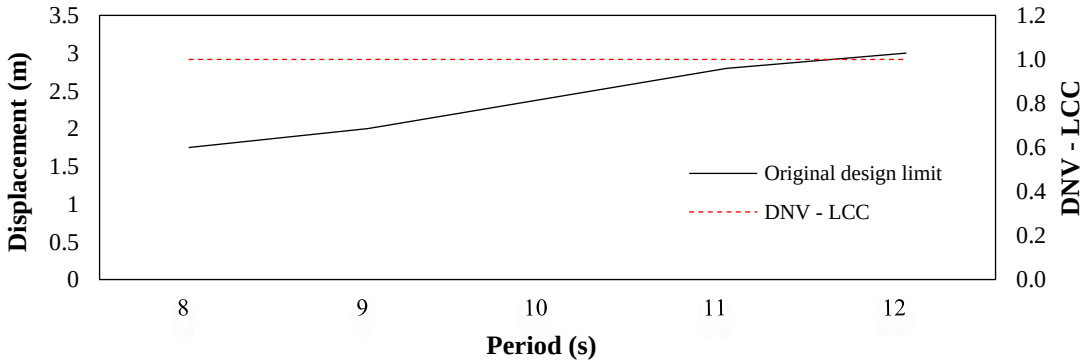

Figure 73: DNV - LCC result for the original design HOM heave limits, deep water case.

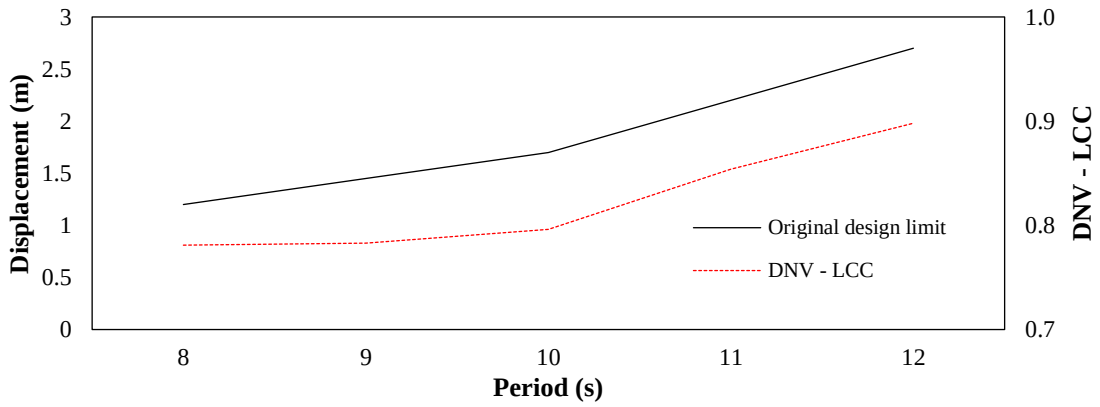

Figure 74: DNV - LCC result for the original design HOM heave limits, shallow water case.

Figure 73 demonstrates that for the deep water case compression was not limiting as the local buckling check limit is fully exploited. That means that no compression is developed for the allowable regarding, local buckling, HOM heave motion – period combinations.

From figure 74, one can observe that for the shallow water case, DNV – LCC check limit is not fully exploited. The HOM heave motions are limited due to compression. Exploring the limits of DNV – LCC regardless the generation of compression, one can get an impression of the potential gain in the allowable HOM motions, if compression was allowed. The limit of DNV – LCC, allowing compression, is demonstrated in the following plot for the shallow water case along with the original design limits.

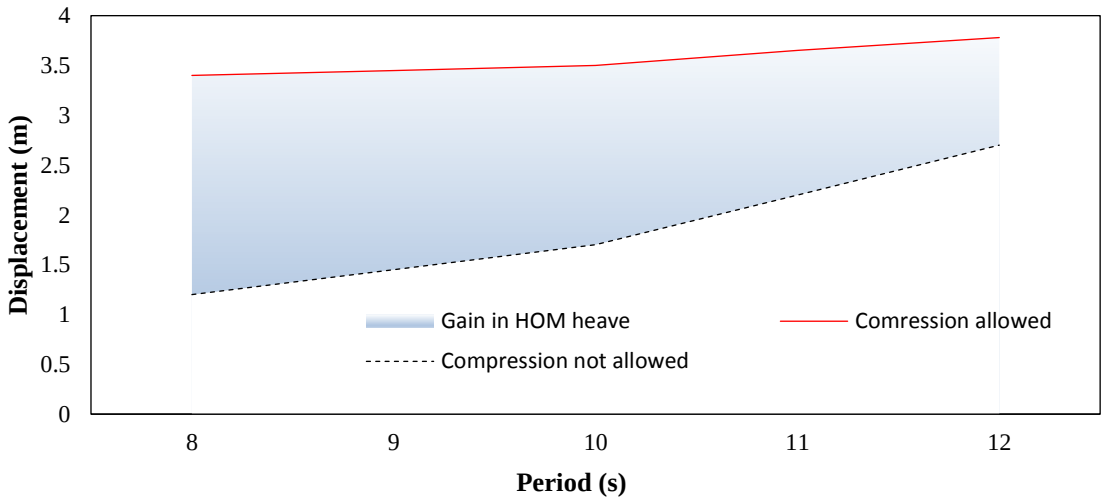

Figure 75: Allowable HOM heave vs period, shallow water case.

The area enclosed by the red line and black continuous line is the potential gain in the allowable HOM heave if compression is allowed provided that other basic pipelay design criteria are met.

6

Conclusions & recommendations

6.1. Conclusions

HMC is intrigued to discover what the constraints are regarding the occurrence of compressive loading during pipe-laying. An applicable methodology based on Flexcom's post-processing results was developed and applied in two base cases in order to identify the critical HOM motions for the onset of impulse dynamic buckling. The main conclusions derived are:

- Compression in the suspended pipeline during installation can be permitted for both base cases. The onset of impulse dynamic buckling for the base cases occurred for HOM motions where the limit of DNV-LCC local buckling check is already exceeded. This renders compressive loading noncritical for the pipelay operation and the local buckling check limits can be fully exploited regardless the occurrence of negative effective tension increasing the operational window.

- The sensitivity study demonstrated that possible limitations can arise due to the variation of the vessel position. It was found that for the base cases examined, the far offset position is leading to lower allowable heave motions of the HOM. This is because, in that position, the amplitude of the dynamic tension amplify while the buckling capacity due to the alternation of the imperfection is not significantly affected. Hence, lower heave motions are needed to destabilize the system. For the load cases that were examined, the introduction of an out of plane offset further reduced the critical heave motions for the onset of impulse dynamic buckling. This is because the introduction of an out of plane imperfection reduces the buckling capacity of the system, while the dynamic tension generation is not significantly affected.

- The friction coefficient between the pipe and the seabed was found to affect the allowable HOM motions. The onset of buckling is accompanied by excessive out of plane deflection. Hence a lower coefficient of friction decreases the critical heave amplitudes for the onset of impulse dynamic buckling.

6.2. Recommendations

- A possible embedment of the pipe can affect the pipes response. For that reason, detailed modeling for the pipe-soil interaction could be useful. The inclusion of transversal springs in Flexcom FE analyses could simulate the embedment of the pipe.

- More sensitivities should be taken into account regarding the critical buckling position of the vessel. It was found that when the vessel is moving from the far to the near offset position, the generated dynamic tension amplitudes are decreasing. In the same time, moving from the far to the near offset position results in an increase in the imperfection of the system. This results in a decrease in the critical buckling load. Hence for different structural configurations than the base cases examined, different vessel positions may be critical regarding the onset of impulse dynamic buckling. A special case could be during the turning of the vessel in order to lay the pipe in a curve, as significant out of plane imperfection could occur in that case.

- When laying pipe in a curve, the compressive loading may introduce limitations regarding the curve stability. This could be a possible limitation regarding compression during pipelaying.

- The dynamic tension being sinusoidal, results in an amplification of the bottom tension, which occasionally exceeds the vessels thrust limit. This should be further investigated as a limitation due to excessive tensile loading could be introduced in that case.

- The study of the strain – rate effect could be particularly useful for pipelay operations. Strain rates lying in the range where the yield strength of the material increases, were found to occur during the dynamic analyses conducted for the present research. Including this effect could yield in increased workability of offshore projects.

Bibliography

[1] A. Simos, A. Fujarra, Dynamic compression of rigid and flexible risers: Experimental and numerical results, Journal of offshore mechanics and Arctic engineering 233-240, 128 (2006).

[2] G.L. Kuiper, J. Brugmans, A.V. Metrikine, Destabilization of deep-water risers by a heaving platform, Journal of sound and vibration, 541-557, 310(3) (2007).

[3] N.J. Hoff, The dynamics of the buckling of elastic columns, Journal of applied mechanics, 68-74, 18 (1951).

[4] D. Karagiozova, M. Alves, Dynamic elastic-plastic buckling of structural elements: A review, Applied mechanics reviews, 61 (2008).

[5] N. F. Morozov, P. E Tovstik, T.P. Tovstik, Again on the Ishlinskii-Lavrentyev problem, Doklady Physics, 189-192, 19(4) (2014).

[6] A. V. Markin, Buckling in an elastic rod under a time-varying load, Journal of Applied Mechanics and Technical Physics, 134-138, 18(1) (1977).

[7] Andrzej Teter, Application of different dynamic stability criteria in case of columns with intermediate stiffeners, Mechanics and Mechanical Engineering, 339-349, 19(2) (2010).

[8] R.J. Mania, Strain rate effect in dynamic buckling of thinned walled isotropic structures, Mechanics and Mechanical Engineering, 189-200, 12(3) (2008).

[9] K. K. Michalska, About some important parameters in dynamic buckling analyses of plated structures subjected to pulse loading, 269-279, 14(2) (2010).

[10] E. Sevin, On the elastic bending of columns due to dynamic axial forces including effects of axial inertia, Journal of Applied Mechanics, 125-131, 27(1) (1960).

[11] K.T. Vipin, R.S Priyadarsini, Effect of imperfection on the dynamic buckling of cylindrical shells under axial impact, International Journal of Scientific & Engineering Research, 5(7) (2014).

[12] H. Hao, H.K. Cheonh, S. Cui, Analyses of imperfect column buckling under intermediate velocity impact, International Journal of Solids and Structures, 5297-5313, 37 (2000).

[13] F. Ribeiro, F. Roveri, F. Mourelle, Dynamic compression buckling in flexible riser, Offshore Technology Conference, (1998).

[14] J.A.P Aranha, M.O Pinto, Dynamic tension in risers and mooring lines: an algebraic approximation for harmonic excitation, Applied ocean research, 63-81, 43 (2001).

[15] H. M. Irvine, T. K. Caughey, The linear theory of free vibrations of a suspended cable, Proceedings of the royal society, 299-315, 341, (1974).

[16] A. Blienk, Dynamic analysis of single span cables, Thesis (Ph.D.) Massachusetts Institute of Technology, Department of Ocean Engineering, (1979).

[17] M.S. Triantafillou, The dynamics of taut incline cables, Massachusetts Institute of Technology, Dept. of Ocean Engineering, (1983).

[18] D. McCann, F. Smith, P. O'Brien, Guidelines for Compression Modeling in Flexible Risers for Deepwater Applications, Offshore Technology Conference, (2003).

[19] H.E. Lindberg, Little book of dynamic buckling, LCE Science/Software, (2003).

[20] G.J. Simitses, Dynamic stability of suddenly loaded structures, Springer – Verlag, (1985).

[21] M. Touati, A. Chelghoum, R.C. Barros, Numerical methods for determining the buckling critical load of thin shells, state of the art, The Bulletin of the Polytechnic Institute of Jassy, Construction. Architecture Section 21, (2012).

[22] R. Mania, Strain rate effect in dynamic buckling of thin walled isotropic columns, Mechanics and Mechanical Engineering, 189-200, 12 (2008).

[23] A. Vakakis. Non-linear normal modes (nnms) and their applications in vibration theory: an overview. Mechanical Systems and Signal processing, Elsevier, 3-22, 11(1) (1997).

[24] L. Artem, S. Hatice, L. Aydin, Exact solution and dynamic buckling analysis of a beam-column system having the elliptic type loading. Applied Mathematics and Mechanics, 1317-1324 (2010).

List of figures

List of tables

Appendix

A. Analytical model mathematical formulation

A.1. Moderately large displacement theory

Comparing to the small deflections theory where infinitesimal angles are being considered, the angles are considered finite, contributing in the strain development of the element. In order to visualize the difference from the theory of small deflections, the initial and deformed configuration due to finite rotation of the beam axis, is illustrated in the following figure.

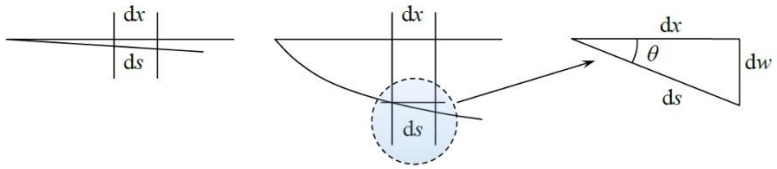

Figure 76: Initial and deformed configuration of beam axis due to rotation.

Were, dx and ds is the initial and deformed configuration respectively. Observing figure 76, one can derive the following geometrical relation:

$$dx = ds\cos\theta \qquad [A.1]$$

Strains are defined as relative displacements. The Cauchy strain formulation is adopted:

$$\varepsilon = \frac{ds^2 - dx^2}{2dx^2} \qquad [A.2]$$

Consider a simply supported beam subjected to an axial motion of its movable support. The strain due to an axial shortening du of the beam is given by:

$$\varepsilon_{long} = -\frac{du}{dx} \qquad [A.3]$$

Due to the imposed axial motion, the axis of the beam rotates and as a consequence, stretches. The total strain of the beam axis denoted as ε^o, is the combined axial strain due to the beams rotation ε_{rot} (extension) and axial motion ε_{long} (shortening).

$$\varepsilon^o = \varepsilon_{long} + \varepsilon_{rot} \quad [A.4]$$

The total strain of the beam axis is different for the small and moderately large deflection theories.

Small deflections theory:

$$\theta^2 \ll 1 \rightarrow dx \approx ds \rightarrow \varepsilon_{rot} = 0 \rightarrow \varepsilon^o = -\frac{du}{dx} \quad [A.5]$$

There is no stress relief because no stretching of the beams midsurface is being considered.

Moderately large deflections theory:

$$cos\theta \approx \left[1 - \frac{\theta^2}{2}\right] \rightarrow dx = dscos\theta \approx ds\left[1 - \frac{\theta^2}{2}\right] \quad [A.6]$$

The approximation given in equation is sufficiently accurate for angles $0 < \theta < 10^o$. Expressing the current length ds in terms of dx and dw one get:

$$ds^2 = dx^2 + dw^2 \quad [A.7]$$

From [A.2] and [A.7] we have

$$\varepsilon_{rot} = \frac{1}{2}\left(\frac{dw}{dx}\right)^2 = \frac{1}{2}\theta^2 \quad [A.8]$$

The total strain of the beam axis due to the beams axial shortening and stretching due to bending is:

$$\varepsilon^o = -\frac{du}{dx} + \frac{1}{2}\left(\frac{dw}{dx}\right)^2 \quad [A.9]$$

This reflects the stress relief due to the finite rotations assumption. Following the simplified, Euler Bernoulli law of linear elasticity, the bending moment M is proportional to the curvature k.

$$M = EIk \quad [A.10]$$

The definition of curvature for the small deflection theory is:

$$k = -\frac{d^2w}{dx^2} \qquad [A.11]$$

Taking into account moderately large deflections expression equation [A.11] becomes:

$$k = \frac{-\frac{d^2w}{dx^2}}{\left(1 + \left(\frac{dw}{dx}\right)^2\right)^{3/2}} \qquad [A.12]$$

The significance of the term $\left(\frac{dw}{dx}\right)^2$ in equation [A.12] is illustrated in the following figure.

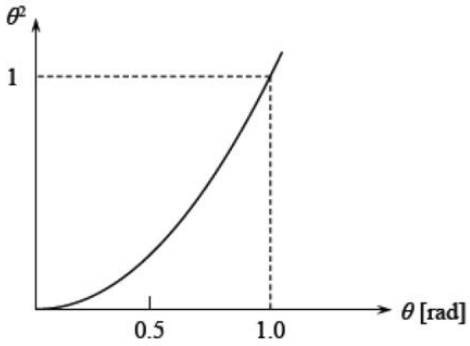

Figure 77: Square slope term variation with angle.

The two terms in the denominator of eq. [A.12] are equal for θ = 1 rad = 57 degrees. However, the validity of the moderately large deflection theory holds for angles up to $\theta = 10^\circ \approx 0.175$ rad. For those values, the squared term of the denominator equals to 0.03, which is insignificant compared to unity. This limitation of the moderately large deflection theory is called as the small strain assumption.

Consequently for angles up to $\theta = 10^\circ \approx 0.175$ rad, the curvature is defined in a similar manner with the small deflections theory.

$$k = -\frac{d^2w}{dx^2} \qquad [A.13]$$

A.2. Derivation of the non-linear EOM of the lateral motion of the curved beam

Consider a simply supported, initially curved Euler Bernoulli beam subjected to a time varying motion of its movable support, denoted as $f(t)$, as shown in figure 78.

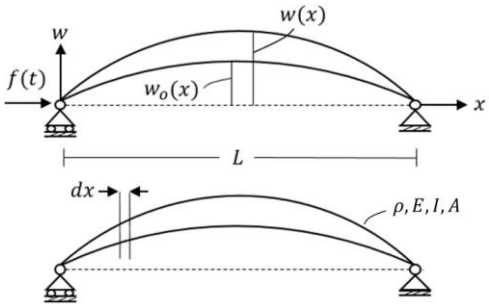

Figure 78: Initialy curved beam subjected to axial motion of movable support

Where, $w(x)$ is the structural deflection of the beam, $w_o(x)$ is the initial unstressed deflection, E is the modulus of elasticity, I is the cross sectional moment of inertia, A is the cross sectional area and ρ is the density of steel. The lateral deflection $w(x)$ is measured from axis x and it is taken positive upwards. The free body diagram of a differential element dx is shown in figure..

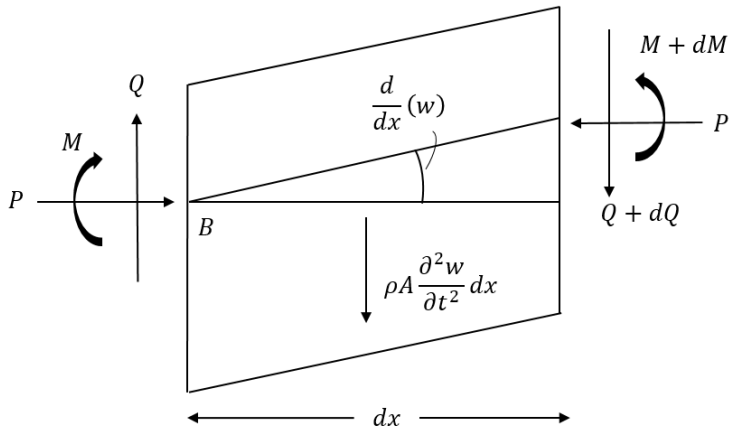

Figure 79: Free body diagram of an imperfect beam differential element

The terms Q and M represent the shearing and bending moment acting on the sides of the element. They are taken positive as illustrated in figure 79. The term $\rho A\ (\partial^2 y/\partial t^2)dx$ is the inertial force acting on the differential element, in the opposite direction of the structural deflection. P is the longitudinal internal axial force of the beam due to the imposed time varying displacement $f(t)$. It is assumed that the axial force is constant along the beams length, L.

The equilibrium of forces in the direction of the vertical axis z, gives:

$$Q - (Q + dQ) - \rho A \frac{\partial^2 w}{\partial t^2} dx = 0 \quad [A.14]$$

or

$$\frac{dQ}{dx} = \rho A \frac{\partial^2 w}{\partial t^2} \quad [A.15]$$

Taking moments around point B yields:

$$M - \rho A \frac{\partial^2 w}{\partial t^2} dx \frac{dx}{2} + (Q + dQ)dx - (M + dM) + P \frac{\partial w}{\partial x} dx = 0 \quad [A.16]$$

Ignoring the second order terms, equation [A.16] is reduced to:

$$Q = \frac{\partial M}{\partial x} - P \frac{\partial w}{\partial x} \quad [A.17]$$

Adopting the Euler Bernoulli beam theory the shear deformations and shortening of the axis of the beam are neglected. The curvature of the beam axis is related to the bending moment by

$$EI \frac{\partial^2 (w - w_o)}{\partial x^2} = -M \quad [A.18]$$

Differentiating equation [A.17] yields:

$$\frac{\partial Q}{\partial x} = \frac{\partial^2 M}{\partial x^2} - P \frac{\partial^2 w}{\partial x^2} \quad [A.19]$$

Substituting equations [A.15] and [A.18] twice differentiated (eliminating Q and M) into equation [A.19] yields:

$$EI \frac{\partial^4 (w - w_o)}{\partial x^4} + P \frac{\partial^2 w}{\partial x^2} + \rho A \frac{\partial^2 w}{\partial t^2} = 0 \quad [A.20]$$

Due to the imposed axial displacement, from the equilibrium of forces along axis x we get:

$$-P = EA\varepsilon^o \quad [A.21]$$

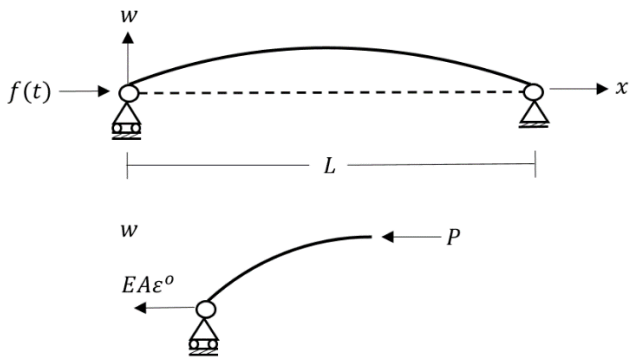

Figure 80: Equilibrium of forces along x direction

Considering moderately large angles, from equations [A.21] and [A.9] we get the following relation for the internal axial load P:

$$-P = EA\left(-\frac{\partial u}{\partial x}+\frac{1}{2}\left(\left(\frac{\partial w}{dx}\right)^2-\left(\frac{\partial w_o}{\partial x}\right)^2\right)\right) \quad [A.22]$$

Where $u = f(t)$ is the imposed axial compressive displacement. Integrating both ends of equation over the beams length and taking into account the initial imperfection w_o, we get:

$$P(t) = \frac{EA}{L}\left(f(t)-\frac{1}{2}\int_0^L\left(\left(\frac{\partial w}{\partial x}\right)^2-\left(\frac{\partial w_o}{\partial x}\right)^2\right)dx\right) \quad [A.23]$$

B. Flexcom vs analytical model results

B.1. Constant amplitude sinusoidal excitation

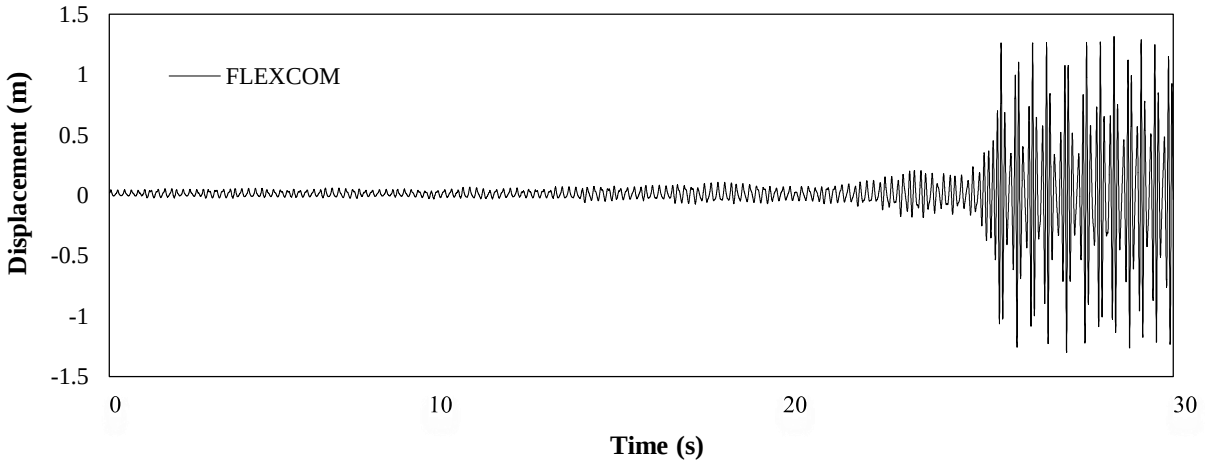

Figure 81: Deflection at midspan, load case A.

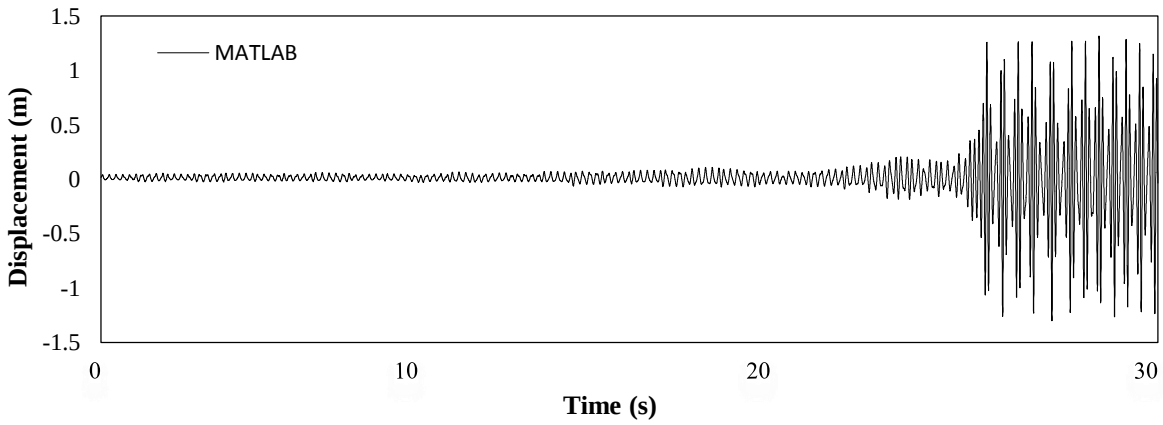

Figure 82: Deflection at midspan, load case A.

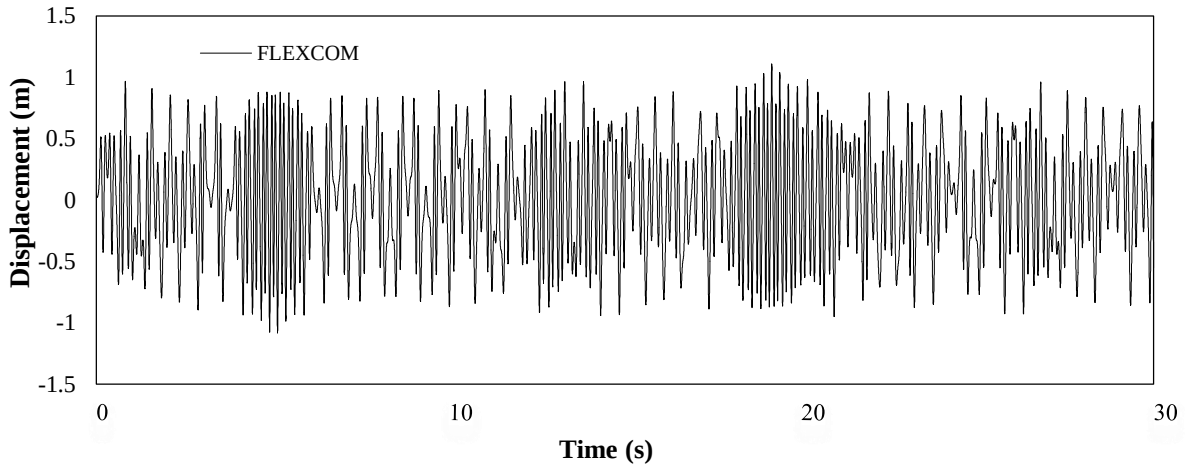

Figure 83: Deflection at midspan, load case B.

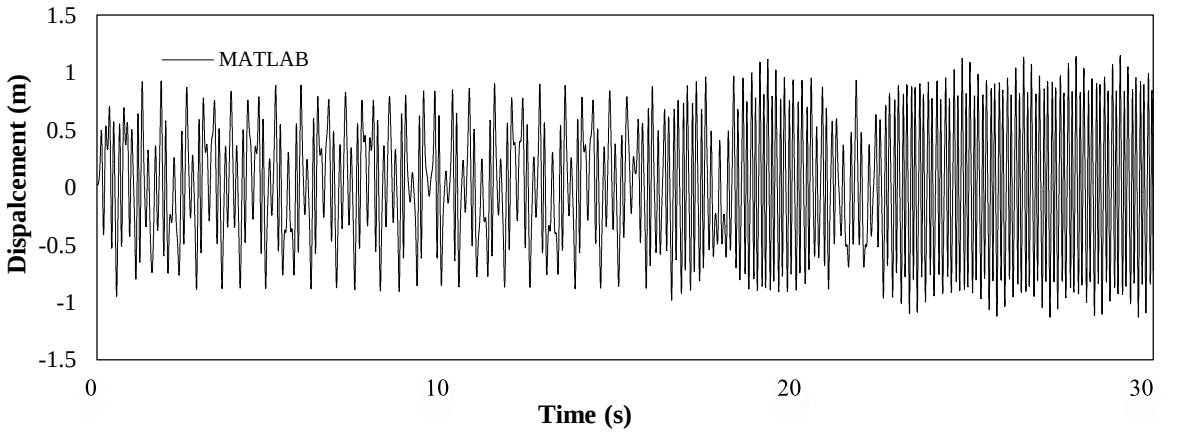

Figure 84: Deflection at midspan, load case B.

B.2. Ramped amplitude sinusoidal excitation

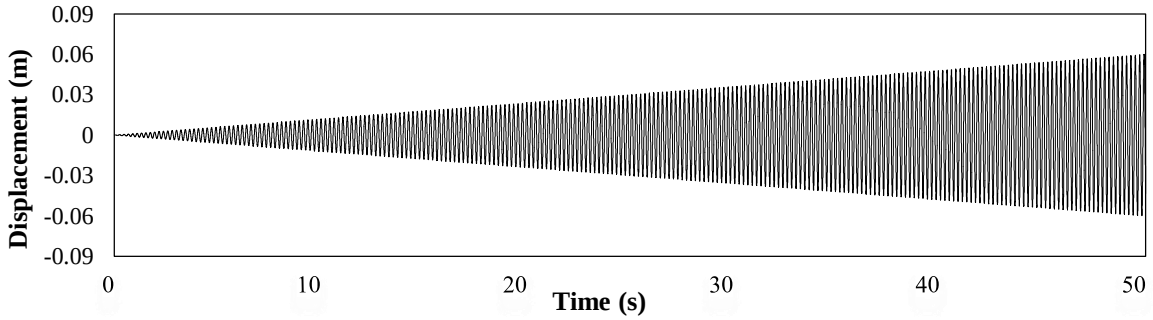

Figure 85: Linearly ramped sinusoidal axial motion of movable support, load case A.

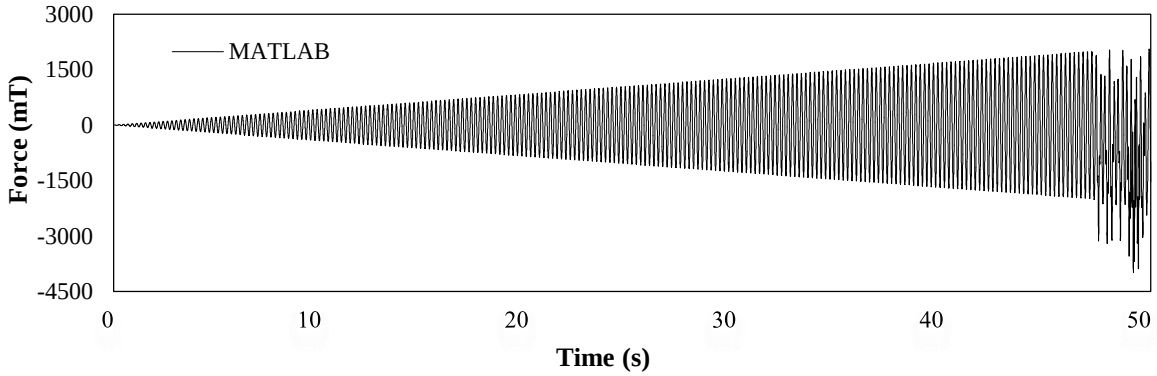

Figure 86: Axial force at midspan, load case A.

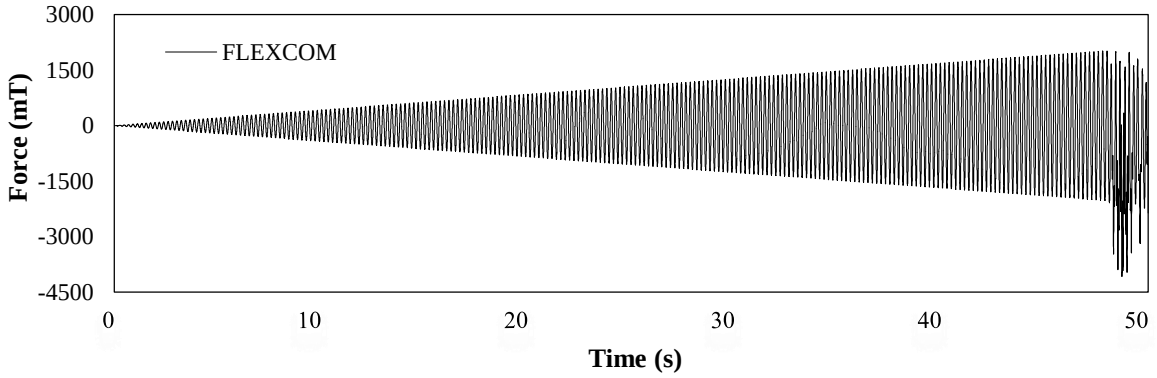

Figure 87: Axial force at midspan, load case A.

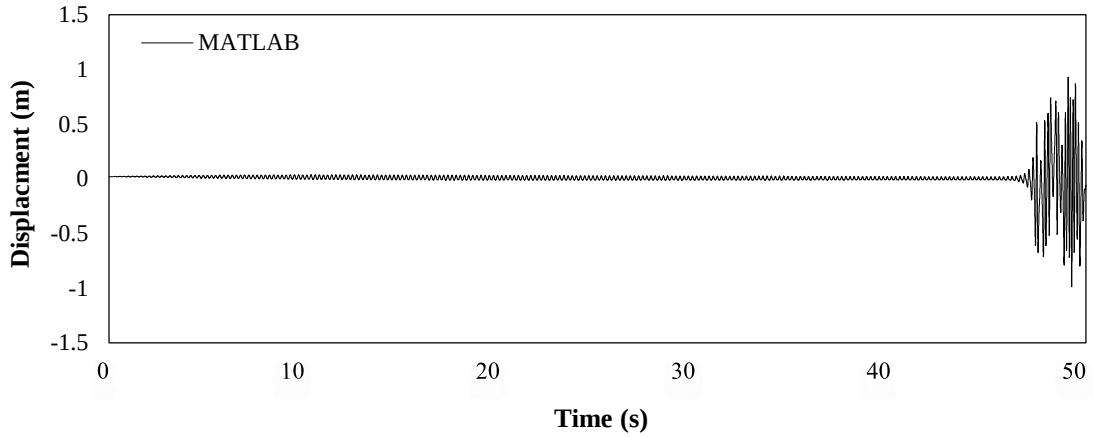

Figure 88: Deflection at midspan, load case A.

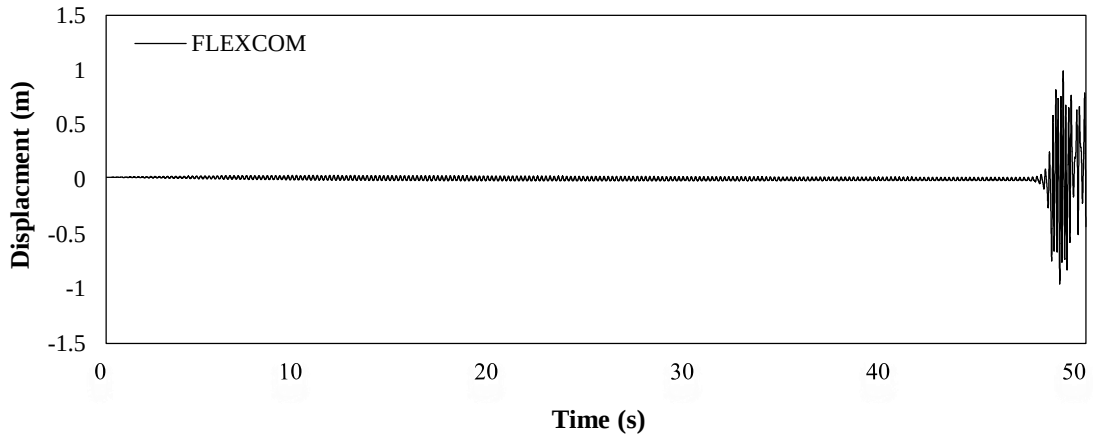

Figure 89: Deflection at midspan, load case A.

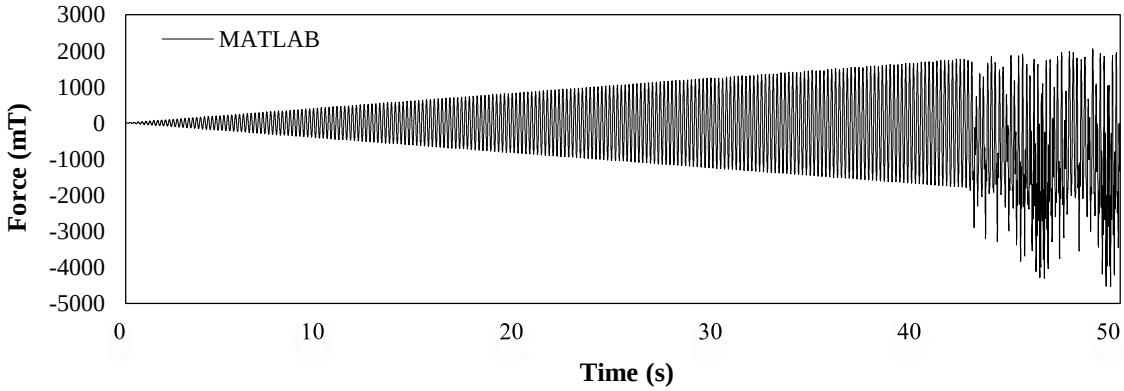

Figure 90: Axial force at midspan, load case B.

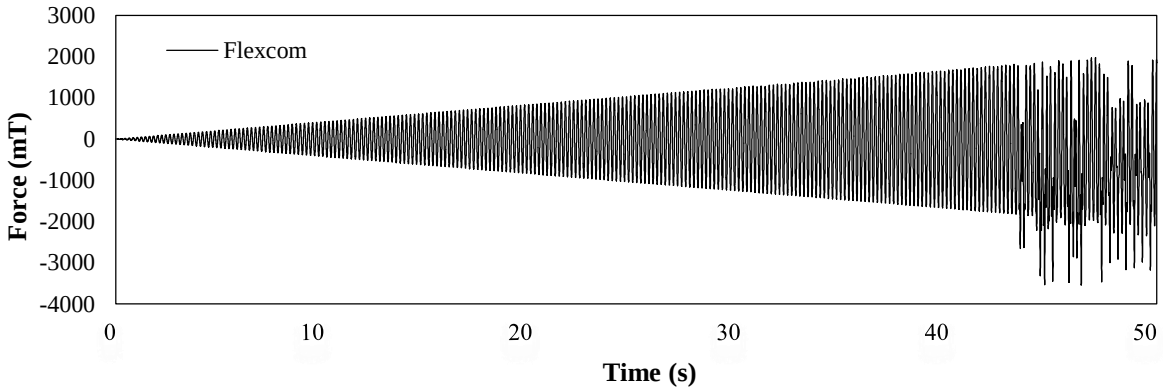

Figure 91: Axial force at midspan, load case B.

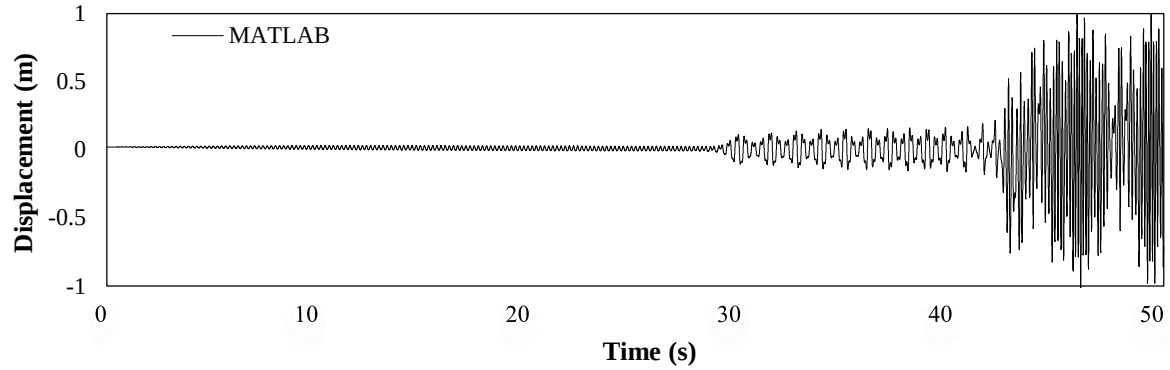

Figure 92: Deflection at midspan, load case B.

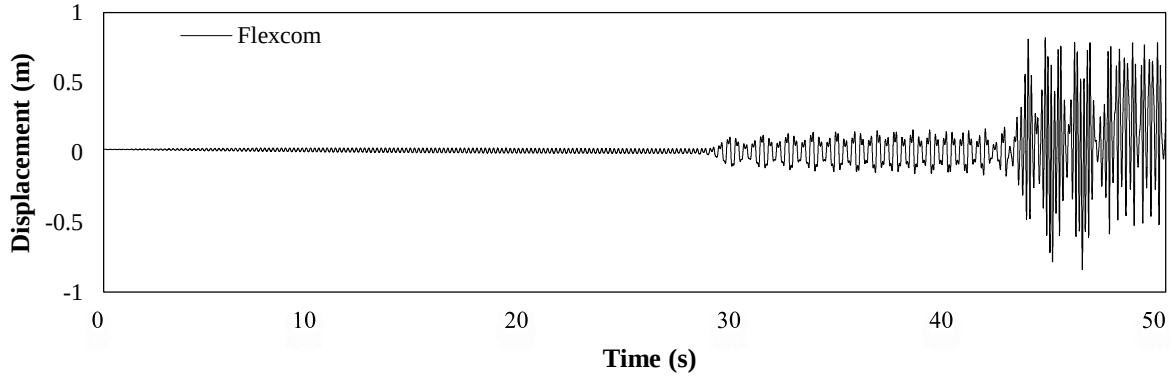

Figure 93: Deflection at midspan, load case B.

C. Flexcom FE analyses results

C.1. Compression generation

Table 19: Total and dynamic effective tension vs HOM heave double amplitude vs HOM period, shallow water case, nominal position.

HOM heave period (s)	HOM heave double amplitude (m)	Minimum total effective tension (mT)	Maximum total effective tension (mT)	Dynamic effective tension (mT)
6	4	-17.61	44.04	30.83
7	4	-9.17	37.72	23.45
8	4	-3.99	32.37	18.18
9	4	-1.05	27.53	14.29
10	4	1.95	25.22	11.64
11	4	4.05	23.52	9.73
12	4	5.04	22.3	8.63
6	3	-9.04	36.2	22.62
7	3	-2.55	31.79	17.17
8	3	0.85	27.55	13.35
9	3	3.26	23.75	10.24
10	3	5.42	22.45	8.51
11	3	6.68	21.29	7.3
12	3	7.47	20.32	6.43
6	2	-1.21	28.25	14.73
7	2	3.34	25.73	11.19
8	2	5.2	22.27	8.53
9	2	7.19	20.26	6.53
10	2	8.47	19.35	5.44
11	2	9.22	18.59	4.69
12	2	9.89	17.91	4.01
6	1	6.69	20.73	7.02
7	1	9	19.65	5.32
8	1	9.67	17.89	4.11
9	1	10.81	16.73	2.96
10	1	11.56	16.24	2.34
11	1	11.69	16.11	2.21
12	1	11.9	15.76	1.93

Table 20: Total and dynamic effective tension vs HOM heave double amplitude vs HOM period, deep water case, nominal position.

HOM heave period (s)	HOM heave double amplitude (m)	Minimum total effective tension (mT)	Maximum total effective tension (mT)	Dynamic effective tension (mT)
6	4	-27.57	51.59	39.58
7	4	-13.34	33.75	23.54
8	4	-5.83	26.1	15.96
9	4	-2.05	21.93	11.99
10	4	1.84	18.27	8.21
11	4	2.89	17.47	7.29
12	4	3.96	16.15	6.09
6	3	-14.22	33.69	23.96
7	3	-4.5	24.4	14.45
8	3	10	20.27	10.14
9	3	2.23	17.93	7.85
10	3	4.42	15.74	5.66
11	3	5.34	14.71	4.68
12	3	5.4	14.32	4.46
6	2	-3.05	22.68	12.86
7	2	1.83	18.59	8.38
8	2	4.15	16.09	5.97
9	2	5.56	14.5	4.47
10	2	6.67	13.3	3.31
11	2	7.28	12.68	2.7
12	2	7.72	12.32	2.3
6	1	4.36	15.53	5.59
7	1	6.54	13.72	3.59
8	1	7.46	12.57	2.56
9	1	8.07	11.86	1.9
10	1	8.43	11.51	1.54
11	1	8.85	11.11	1.13
12	1	8.97	11.04	1.03

Table 21: Dynamic effective tension vs period vs vessel position, H=4m, shallow water case.

HOM heave period (s)	Zero offset Dynamic effective tension (mT)	Near offset Dynamic effective tension (mT)	Far offset Dynamic effective tension (mT)
6	30.83	27.13	44.21
7	23.45	20.09	32.32
8	18.18	15.88	23.24
9	14.29	11.81	17.99
10	11.64	10.19	15.43
11	9.73	8.43	13.23
12	8.63	7.37	11.51

Table 22: : Dynamic effective tension vs period vs vessel position, H=4m, deep water case.

HOM heave period (s)	Zero offset Dynamic effective tension (mT)	Near offset Dynamic effective tension (mT)	Far offset Dynamic effective tension (mT)
6	39.58	24.86	107.83
7	23.54	23.17	67.83
8	15.96	15.62	46.12
9	11.99	11.91	32.09
10	8.21	9.41	24.75
11	7.29	7.68	18.74
12	6.09	6.14	13.53

Table 23: Total effective tension vs period vs vessel position, H=4m, shallow water case.

HOM heave period (s)	Zero offset Total effective tension (min) (mT)	Near offset Total effective tension (min) (mT)	Far offset Total effective tension (min) (mT)
6	-17.61	-16.05	-19.44
7	-9.17	-7.09	-11.53
8	-3.99	-5.09	-4.73
9	-1.05	-1.34	1.57
10	1.95	0.59	4.14
11	4.05	2.30	6.93
12	5.04	3.39	8.56

Table 24: Total effective tension vs period vs vessel position, H=4m, deep water case.

HOM heave period (s)	Zero offset Total effective tension (min) (mT)	Near offset Total effective tension (min) (mT)	Far offset Total effective tension (min) (mT)
6	-27.57	-12.61	-48.02
7	-13.34	-7.56	-40.97
8	-5.83	-4.01	-18.84
9	-2.05	-2.10	-4.048
10	1.84	-0.85	2.74
11	2.89	-0.04	8.93
12	3.96	0.78	14.25

C.2. Constant velocity loading

Table 25: Constant velocity loading results, load case A.

Project	**Shallow**		**Deep**	
Velocity (m/s)	**P_{cr} (mT)**	**DLF**	**P_{cr} (mT)**	**DLF**
0.0001	2.35	1	0.64	1
0.001	2.35	1	0.64	1
0.05	2.7	1.17	0.8	1.25
0.1	10.07	4.28	10.99	17.17
0.2	34.75	14.78	31.36	49.01
0.3	54.91	23.37	51.73	80.82
0.4	75.39	32.08	72.10	112.66
0.5	95.48	40.63	92.48	144.50

Table 26: Constant velocity loading results, load case B.

Project	**Shallow**		**Deep**	
Velocity (m/s)	**P_{cr} (mT)**	**DLF**	**P_{cr} (mT)**	**DLF**
0.0001	3.18	1	0.81	1
0.001	3.18	1.89	0.81	1
0.05	3.65	2.36	1.01	1.25
0.1	13.61	7.73	11.91	14.70
0.2	46.96	18.47	33.83	41.77
0.3	74.20	29.2	55.72	68.79
0.4	101.88	39.93	77.61	95.81
0.5	129.03	50.65	99.50	122.84

Table 27: Constant velocity loading results, load case C.

Project	Shallow		Deep	
Velocity (m/s)	P_{cr} (mT)	DLF	P_{cr} (mT)	DLF
0.0001	6.02	1	3.02	1
0.001	6.02	1.89	3.02	1
0.05	7.52	2.36	3.77	1.25
0.1	24.58	7.73	17.95	5.94
0.2	58.68	18.47	46.31	15.33
0.3	92.78	29.20	74.72	24.74
0.4	126.88	39.93	103.12	34.08
0.5	149.03	40.60	132.53	43.76

Table 28: Constant velocity loading results, load case D.

Project	Shallow		Deep	
Velocity (m/s)	P_{cr} (mT)	DLF	P_{cr} (mT)	DLF
0.0001	2.71	1	2.56	1
0.001	2.70	1	2.56	1
0.05	3.38	1.25	3.2	1.25
0.1	20.61	7.63	17.7	6.91
0.2	55.07	20.39	45.92	17.94
0.3	89.52	33.15	74.01	28.91
0.4	123.99	45.91	102.72	40.13
0.5	146.15	58.66	131.26	51.27

C.3. Harmonic displacement loading

Table 29: Critical HOM motion parameters for the onset of impulse dynamic buckling, load case A.

Case: A		Shallow					Deep			
Period (s)	P_{cr} (mT)	J (mTs)	H_{cr} (m)	v_{cr} (m/s)	a_{cr} (m/s^2)	P_{cr} (mTs)	J mTs)	H_{cr} (m)	v_{cr} (m/s)	a_{cr} (m/s^2)
8	113	288	6.11	4.80	3.77	33	84	3.91	3.07	2.41
9	118	338	7.10	4.94	3.48	35	100	5.04	3.47	2.42
10	123	392	8.08	5.08	3.19	36	115	6.17	3.88	2.44
11	134	469	8.84	5.05	2.91	42	147	7.18	4.08	2.34
12	145	554	9.59	5.02	2.63	53	202	8.19	4.29	2.25

Table 30: Critical HOM motion parameters for the onset of impulse dynamic buckling, load case B.

Case: B		Shallow					Deep			
Period (s)	P_{cr} (mT)	J (mTs)	H_{cr} (m)	v_{cr} (m/s)	a_{cr} (m/s^2)	P_{cr} (mT)	J (mTs)	H_{cr} (m)	v_{cr} (m/s)	a_{cr} (m/s^2)
8	80.25	204	6.11	4.80	3.77	31.43	80	3.80	2.98	2.34
9	83.41	239	6.77	4.73	3.30	31.97	92	4.61	3.22	2.25
10	88.34	281	8.08	5.08	3.19	31.10	99	5.69	3.58	2.25
11	87.04	305	8.73	4.99	2.85	36.14	127	6.42	3.67	2.09
12	89.58	342	9.59	5.02	2.63	38.82	148	7.14	3.74	1.96

Table 31: Critical HOM motion parameters for the onset of impulse dynamic buckling, load case C.

Case: C		Shallow					Deep			
Period (s)	P_{cr} (mT)	J (mTs)	H_{cr} (m)	v_{cr} (m/s)	a_{cr} (m/s^2)	P_{cr} (mT)	J (mTs)	H_{cr} (m)	v_{cr} (m/s)	a_{cr} (m/s^2)
8	81.35	207	4.79	3.76	2.95	33.38	85	3.14	2.47	1.94
9	83.76	234	5.51	3.85	2.69	36.43	104	3.94	2.75	1.92
10	86.26	275	6.30	3.96	2.49	34.79	110	4.77	3.00	1.88
11	89.70	314	7.08	4.05	2.31	35.81	125	5.53	3.16	1.80
12	93.10	356	7.88	4.13	2.16	41.12	157	6.18	3.24	1.69

Table 32: Critical HOM motion parameters for the onset of impulse dynamic buckling, load case D.

Case: D		Shallow					Deep			
Period (s)	P_{cr} (mT)	J (mTs)	H_{cr} (m)	v_{cr} (m/s)	a_{cr} (m/s^2)	P_{cr} (mT)	J (mTs)	H_{cr} (m)	v_{cr} (m/s)	a_{cr} (m/s^2)
8	63.30	161	4.34	3.41	2.68	24.95	64	2.84	2.23	1.75
9	71.14	204	5.17	3.61	2.52	23.71	68	3.32	2.32	1.62
10	65.54	209	5.61	3.52	2.21	25.12	80	4.26	2.68	1.68
11	78.72	276	6.69	3.82	2.18	24.83	87	4.62	2.64	1.51
12	77.17	295	7.21	3.78	1.98	26.80	102	5.40	2.83	1.48

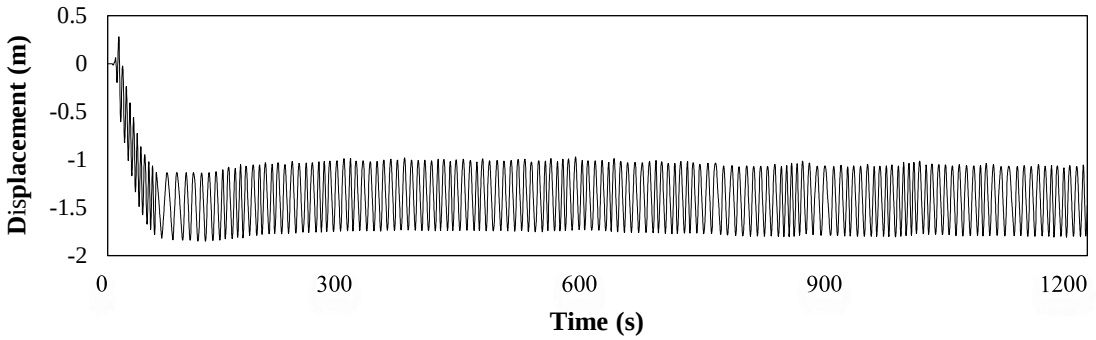

Figure 94: In plane deflection, H=2.9m, T=3.4m, deep water case.

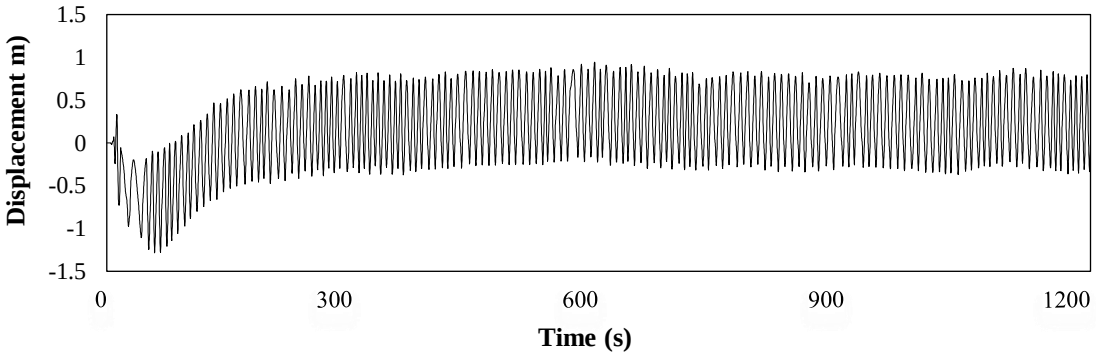

Figure 95: In plane deflection, H=3.4m, T=8s, deep water case.

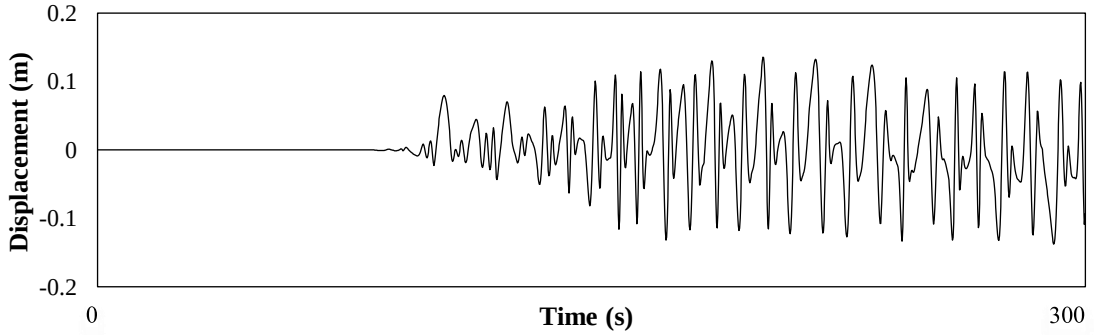

Figure 96: Out of plane deflection, H=2.9m, T=8s, deep water case.

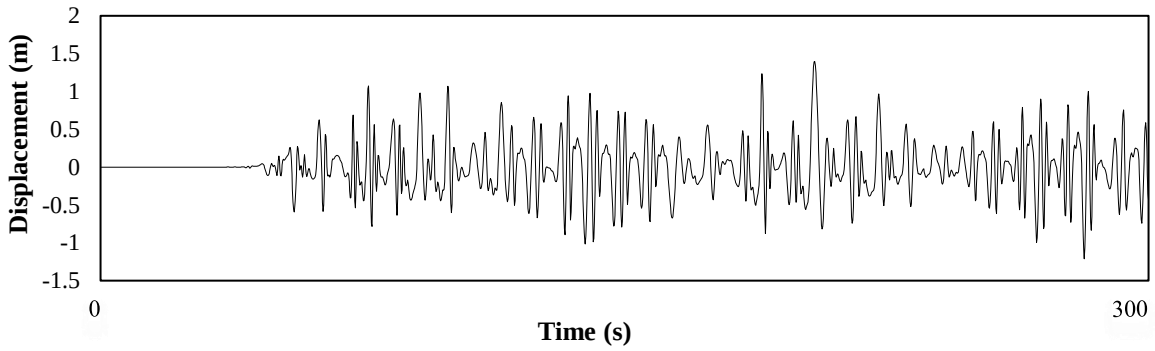

Figure 97: Out of plane deflection, H=3.4,, T=8s, deep water case.

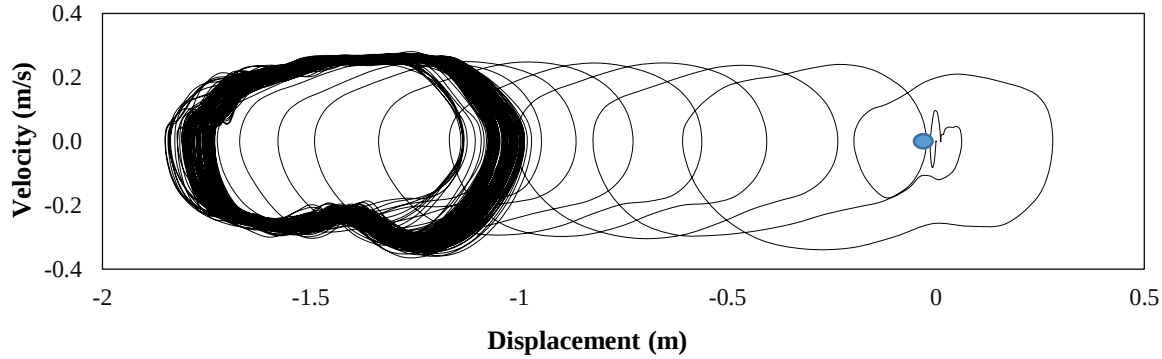

Figure 98: In plane motion phase plain, H=2.9m, T=8s, deep water case.

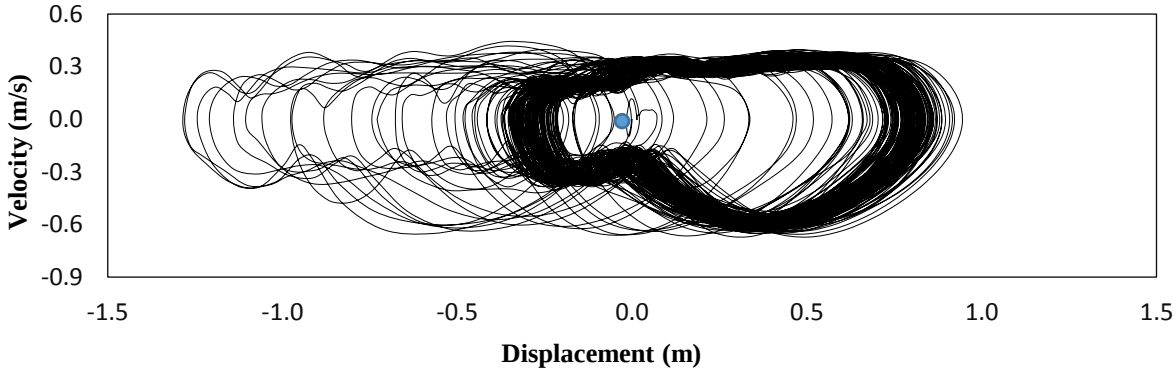

Figure 99: In plane motion phase plain, H=3.4m, T=8s, deep water case.

D. MATLAB Code

Main.m

```
% INPUT-----------------------------------------------------------------

clc
clear all
close all

% Beam properties
P.rho_st=7850;              % Density of steel [kg/m^3]
P.E=2e11;                   % Modulus of elasticity [N/m^2]
P.V=[0.5];                  % Compression rate [m/s]
P.L=20 ;                    % Length [m]
P.d=0.01981;                % Imperfection amplitude [m]
Di=0.54;                    % Internal diameter [m]
Do=0.58;                    % External diameter [m]

% OUTPUT----------------------------------------------------------------

%Beam properties
P.A=pi*(Do^2-Di^2)/4;       % Cross sectional Area [m^2]
P.I=pi*(Do^4-Di^4)/64;      % Cross sectional Moment of inertia [m^4]
R=(Do^2+Di^2)^0.5/4;        % Radius of gyration [m]
ratio=P.L/R;                % Slenderness ratio [-]
Bend_stiff=P.E*P.I;         % Bending stiffness [N/m]
Axial_stiff=P.E*P.A;        % Axial stiffness [N/m]


%Dynamic similarity
Pe=(pi^2*P.E*P.I)/P.L^2;                % Euler buckling load [N]
Vs=(P.E/P.rho_st)^0.5;                  % Velocity of compr waves [m/s]
P.Omega=pi^8*(R/P.L)^6.*(Vs./P.V).^2;   % Dynamic similarity number [-]

timestep_s_stable=0.016*P.Omega^(-0.5); % stability of timestep [-]
timestep_sec=0.001;                     % timestep [s]
s=0:timestep_sec:1;                     % simulation interval [s]

%Initial conditions
init_disp = P.d;                        % Midspan IC - displacement [m]
init_vel = 0;                           % Midspan IC - velocity [m/s]
q_0=[init_disp;init_vel];               % IC [-]
P.n=1;                                  % Mode number [-]

%----------------------------------------------------------------------
```

Constant_velocity_loading.m

```
% INPUT-----------------------------------------------------------------

P.V=[0.5];                  % Compression rate [m/s]

% OUTPUT----------------------------------------------------------------

%ODE_45
[S,X_num_1] = ode45(@(t,q_n) odeFunc_const(t,q_n,P),s,q_0);


% Axial load at midspan
Pcr=P.E*P.A/P.L*(P.V.*s'+0.5*(pi^2*(P.d^2-X_num_1(:,1).^2)/(2*P.L)));

% Stiffness matrix
stiffness_matrix=(P.L/2)*P.E*P.I*(pi/P.L)^4-Pcr.*(pi/P.L)^2*P.L/2;

%-----------------------------------------------------------------------
```

odeFunc_const.m

```
function q_n_dot=odeFunc_const_new_1(t,q_n,P)
q_n_dot=[q_n(2); (q_n(1)*(P.n*pi/P.L)^2*(+P.E*P.A/P.L*(P.V*t-0.5*((-
2*pi^2*P.d^2+pi*P.n*(sin(2*pi*P.n)+2*pi*P.n)*q_n(1).^2))/(4*P.L)))+P.E*P
.I*(pi/P.L)^4*P.d-P.E*P.I*(pi*P.n/P.L)^4*q_n(1))/(P.A*P.rho_st) ];
end

%-----------------------------------------------------------------------
```

Harmonic_velocity_loading.m

```
% INPUT-----------------------------------------------------------------

% Mode of vibration (1:9.87 / 2:39.5 / 3:88.8)
n=[9.87 39.5 88.8];

% Fudamental flexular radial frequency (rad/s)
w=n(1)*(P.E*P.I/(P.rho_st*P.A*P.L^4))^0.5;

P.D=0.07;           % Sinosoidal displacement amplitude [m]
T=0.2546;           % Excitation Period[s]

% OUTPUT----------------------------------------------------------------

P.w=2*pi/T;         % Radial frequency [rad/s]
P.V=P.D*P.w;        % Sinosoidal velocity amplitude [m/s]

% ODE 45
[S,X_num_1] = ode45(@(t,q_n) odeFunc_harm (t,q_n,P),s,q_0);

% Axial force at midspan
Pcr=P.E*P.A/P.L*(P.D*sin(P.w.*s')+0.5*(pi^2*(P.d^2-
X_num_1(:,1).^2)/(2*P.L)));
```

```
%-------------------------------------------------------------------------


odeFunc_harm.m

function q_n_dot=odeFunc_harm(t,q_n,P)
q_n_dot=[q_n(2);
(((q_n(1))*(1*pi/P.L)^2/(P.rho_st*P.A)*P.E*P.A/P.L*(P.D*sin(P.w*t)+0.5*(
pi^2*(P.d^2-1*q_n(1)^2)/(2*P.L)))-
P.E*P.I/(P.rho_st*P.A)*(1*pi/P.L)^4*(q_n(1)-P.d)))];
end

%-------------------------------------------------------------------------


Half_sin_disp_pulse.m

% INPUT----------------------------------------------------------------

P.D=0.06;                    % Sinosoidal displacement amplitude[m]
T=0.5;                       % Pulse duration x 2 [s]
P.simulation_length=10;      % Simulation interval [s]

% OUTPUT---------------------------------------------------------------

P.w=2*pi/T;
s=0:timestep_sec:P.simulation_length;
ss=0:timestep_sec:P.simulation_length;
P.length=length(s);
P.limit=round(T/2/timestep_sec);
ss(1,P.limit:length(s))=0;
P.s=s;
P.limit_ode=T/2;
disp=P.D*sin(P.w*ss);
vel=P.V*cos(P.w*ss);

[S,X_num_1] = ode45(@(t,q_n) odeFunc_harm_new_1_PULSE(t,q_n,P),s,q_0);

Pcr=P.E*P.A/P.L*(P.D*sin(P.w.*s')+0.5*(pi^2*(P.d^2-
X_num_1(:,1).^2)/(2*P.L)));
stiffness_matrix=(P.L/2)*P.E*P.I*(pi/P.L)^4-Pcr.*(pi/P.L)^2*P.L/2;

%-------------------------------------------------------------------------


odeFunc_pulse.m

function q_n_dot=odeFunc_pulse(t,q_n,P)
% q_n_dot=zeros(1001,2);

if t < P.limit_ode
q_n_dot=[q_n(2);
(((q_n(1))*(1*pi/P.L)^2/(P.rho_st*P.A)*P.E*P.A/P.L*(P.D*sin(P.w*t)+0.5*(
pi^2*(P.d^2-1*q_n(1)^2)/(2*P.L)))-
P.E*P.I/(P.rho_st*P.A)*(1*pi/P.L)^4*(q_n(1)-P.d)))];
```

```
else
q_n_dot=[q_n(2);
(((q_n(1))*(1*pi/P.L)^2/(P.rho_st*P.A)*P.E*P.A/P.L*(0*sin(P.w*t)+0.5*(pi
^2*(P.d^2-1*q_n(1)^2)/(2*P.L)))-
P.E*P.I/(P.rho_st*P.A)*(1*pi/P.L)^4*(q_n(1)-P.d)))];
end
end

%-------------------------------------------------------------------------
```

Sinusoidal_ramped.m

```
% INPUT-----------------------------------------------------------------

P.D=0.05;                           % Target amplitude [m]
T=0.192;                            % Period of excitation [s]

% OUTPUT----------------------------------------------------------------

P.w=2*pi/T;
timestep_sec=0.001;
P.timestep=timestep_sec;
s=0:timestep_sec:50;
P.length=length(s);
disp=P.D*s./length(s)/timestep_sec.*sin(P.w*s);

% ODE 45
[S,X_num_1] = ode45(@(t,q_n) odeFunc_harm_new_1_RAMP(t,q_n,P),s,q_0);
stiffness_matrix=(P.L/2)*P.E*P.I*(pi/P.L)^4-
P.E*P.A/P.L*(abs((P.D*s./P.length/P.timestep).*sin(P.w*s))+(0.5*(pi^2*(P
.d^2-1* X_num_1(:,1)'.^2)/(2*P.L))));
stress=P.E*P.D*(abs((P.D*s./P.length/P.timestep).*sin(P.w*s))+abs(0.5*(p
i^2*(P.d^2-1* X_num_1(:,1)'.^2))));

% Axial force at midspan
Pcr=P.E*P.A/P.L*(P.D*sin(P.w.*s')+0.5*(pi^2*(P.d^2-
X_num_1(:,1).^2)/(2*P.L)));

%-------------------------------------------------------------------------
```

odeFunc_ramp.m

```
function q_n_dot=odeFunc_ramp(t,q_n,P)
q_n_dot=[q_n(2);
(((q_n(1))*(1*pi/P.L)^2/(P.rho_st*P.A)*P.E*P.A/P.L*((P.D*t./P.length/P.t
imestep)*sin(P.w*t)+0.5*(pi^2*(P.d^2-1*q_n(1)^2)/(2*P.L)))-
P.E*P.I/(P.rho_st*P.A)*(1*pi/P.L)^4*(q_n(1)-P.d)))];
end

%-------------------------------------------------------------------------
```

plots.m

```
% OUTPUT-----------------------------------------------------------------

% Displacement at midspan
figure
plot (s,X_num_1(:,1));
xlabel('Time [s]','FontSize',12);
ylabel('Deflection [m] - Mode 1','FontSize',12);
title('Shallow Arch Dynamic Buckling','FontSize',12);
grid minor
% Displacement Phase plain
figure
plot (X_num_1(:,1),X_num_1(:,2));
xlabel('Deflection [m]- Mode 1','FontSize',12);
ylabel('Velocity [m/s]','FontSize',12);
title('Shallow Arch Dynamic Buckling','FontSize',12);
grid minor

% Axial force at midspan
figure
plot (s,Pcr);
xlabel('Time [s]','FontSize',12);
ylabel('Pcr [N],n=1','FontSize',12);
title('Shallow Arch Dynamic Buckling','FontSize',12);
grid minor

% Stiffness matrix
figure
plot (s,stiffness_matrix);
xlabel('Time [s]','FontSize',12);
ylabel('Stiffness','FontSize',12);
title('Shallow Arch Dynamic Buckling','FontSize',12);
grid minor

% Bending stress at midspan
figure
plot (s,stress);
xlabel('Time [s]','FontSize',12);
ylabel('Total stress in outer diameter - First mode','FontSize',12);
title('Shallow Arch Dynamic Buckling','FontSize',12);
grid minor

%-----------------------------------------------------------------------
```

Impulse_calculator.m

```
% INPUT-----------------------------------------------------------------

clc
clear
clear all
close all

A=[];

% OUTPUT----------------------------------------------------------------

pulse_11=A'./10000;
time=(0:(length(A)-1))./100;

figure
plot(time,pulse_11,'r')
grid on
title('CRITCAL FORCE IMPULSE T=11s')
xlabel('Time (s)')
ylabel('Effective tension (anchorage) (mT)')
xverts = [time(1:end-1); time(1:end-1); time(2:end); time(2:end)];
yverts = [zeros(1,(length(A)-1)); pulse_11(1:end-1); pulse_11(2:end);
zeros(1,(length(A)-1))];
p = patch(xverts,yverts,'b','LineWidth',1.5);

capacity_11=trapz(pulse_11)/100;
hold on
plot(time,pulse_11,'r','LineWidth',1.5);

%----------------------------------------------------------------------
```